Impact of Red Cell Distribution in Sheared Blood Flow upon Quantification of Hemolysis Rate in Artificial Organs

Einfluß der Verteilung der roten Blutkörperchen in einer Scherströmung auf die Hämolyse in künstlichen Organen

Von der Fakultät für Maschinenwesen der Rheinisch-Westfälischen Technischen Hochschule Aachen zur Erlangung des akademischen Grades eines Doktors der Ingenieur-wissenschaften genehmigte Dissertation

vorgelegt von

Ali Poorkhalil

Berichter: Univ.-Prof. Dr.-Ing. Jochen Büchs

Prof. Dr. rer. nat. Khosrow Mottaghy

Tag der mündlichen Prüfung : 09.09.2016

Diese Dissertation ist auf den Internetseiten der Universitätsbibliothek online verfügbar.

Dedicated to "**Baghiat allah al aazam (aj)**"

Acknowledgments

This thesis is the result of my studies at the ECC Lab (Extracorporeal Circulation Laboratory), Institute of Physiology, in cooperation with AVT-Biochemical Engineering at RWTH Aachen University.

I am especially grateful to my supervisor Professor Dr. Khosrow Mottaghy, who suggested me this interesting topic and gave me the opportunity to do research in the field of Biomedical Engineering Sciences and I could always enjoy his depth knowledge and expertise. He introduced me to this highly interdisciplinary field of research and gave me the possibility to work with a high degree of freedom and individual responsibility.

I wish to sincerely thank also Professor Jochen Büchs for his interest, support and encouragement of my Dissertation. I am also grateful to Assoc. Prof. Ghassem Amoabediny from University of Tehran who supported as a mentor for my research activities in Aachen and also regarding my scholarship (MSRT).

Also I wish to thank Dr.-Ing. Ali Kashefi. His knowledge who generously shared with me his knowledge in the technical aspects of extracorporeal circulation. Furthermore, I would like to express my thanks also to all my friends and associates in the institute of physiology for their support especially Dr. Hadi Tabesh and M.Sc. Foivos Mouzakis and Dr. Ali Khachab.

I owe my life, my education and the pleasure of learning to my parents. I wish to express my deep gratitude towards my mother Batul and my father Khodayar. I would like to thank my wife Foroogh. Her support, encouragement, quiet patience and unwavering love were undeniably the bedrock upon which the past six years of my life have been built. Last but not least, I thank our little daughter Hanane whose presence gave me additional energy to continue with the scientific activities.

Aachen, September 2016

Ali Poorkhalil

Abstract

Blood contacting artificial organs, whether used as a bridge to transplantation, or even as a permanent organ replacement, find ever increasing application in contemporary medicine. Hemocompatibility and blood trauma minimization (e.g. hemolysis) are the two key factors in artificial organ development and design optimization. These issues become rather imperative for blood contacting devices, designed for long term application. Hemolysis is considered to be a function of shear stress and shear exposure time. Each device, based on its function, it may perform under a very broad range of operational conditions; high shear stress and short exposure time, e.g. ventricle assist devices (VADs) or low shear stress and long exposure time (e.g. dialyzers).

Where VADs are concerned, high shear regions might be unavoidable on the ground of pumping performance maximization, but on the other hand, the existence of these regions tends to be avoided, due to design modifications for improved hemocompatibility. However, the performance and design characteristics have contradictory effects on each other, concerning their optimization. In spite of their low shear stress, conventional dialyzers exhibit relatively long exposure and contact time with foreign surfaces, which highlights the necessity of design optimization for good hemocompatibility.

In an effort to address the above stated challenges, the first part of this study describes the theoretical and physiological background (chapter 1-4) and further the experimental studies (Chapters 5-6), as a manifestation of shear field induced erythrocyte distribution and local hematocrit, on the resulting hemolysis, through an innovative hypothesis that treats blood as a multiphase fluid. Two modified Taylor – Couette devices mimicking the VADs blood flow pattern, are designed and manufactured to investigate the outcomes of shear field variation on the resulting hemolysis. In addition, a semi-empirical hemolysis model that considers the dominant phenomena involved in the process, is presented, to provide a better understanding and prediction of the resulting hemolysis mechanism. The proposed hypothesis as well as the semi-empirical hemolysis model are then validated by in-vitro investigations, using fresh human and animal (porcine) blood.

The effect of filtration and backfiltration processes on local hematocrit in dialyzers, and the subsequent generation of hemolysis, is studied in the second part (Chapters 7-9) as a counter case to VADs. Semi-empirical models predicting the courses of hematocrit, flow rate and

pressure, are introduced, and mathematical equations governing the mass transfer phenomena are established, in order to further the understanding of dialysis hemodynamics. In-vitro investigations are carried out for different validation purposes, using porcine blood, in pursuance of the aforementioned mathematical models.

The findings of this study emphasize the importance of the consideration of shear induced cell migration and distribution, has a significant impact on the resulting hemolysis, and is a key factor for the design and performance optimization of artificial organs with various flow characteristics.

Zusammenfassung

Künstliche Organe zur temporären bzw. dauerhaften Unterstützung und Ersatz von erkrankten Organen finden immer mehr Anwendung in der modernen Medizin. Bei Optimierung von Design und Konstruktion der künstlichen Organen sind nicht nur die Leistungsdaten des zu entwickelnden künstlichen Organs von Bedeutung, sondern auch die Frage der Hämokompatibilität und des Bluttraumas insbesondere Hämolyse. Gerade bei der Langzeitanwendung von künstlichen Organen nehmen diese Faktoren an Bedeutung zu. Mechanische Hämolyse ist vordergründig eine Funktion der Scherspannung und Belastungsdauer. Jeder Anwendung, basierend auf ihrer Funktion, Einsatzzweck und Dauer, werden unterschiedliche Betriebsbedingungen zugrunde gelegt: Hohe Scherbeanspruchung und kurze Belastungsdauer, z.B. Ventrikel Unterstützungssysteme (Ventricle Assist Device, VAD) mit Hilfe von „ Rotary Pumps" oder niedrigere Scherbelastungen aber langere Anwendungsdauer wie bei Dialyseverfahren.

Bei der Konstruktion und Optimierung von rotatorischen Blutpumpen sind unterschiedliche Aspekte, vor allem Maximierung der Pumpleistung und Minimierung deren Größe für eine minimale Schädigung der Blutzellen zu berücksichtigen. Allerdings haben Optimierungen unter verschiedenen Vorgaben widersprüchliche Auswirkungen aufeinander. Hohe Pumpleistung zu erzielen, hat zur Folge, dass innerhalb der Pumpe Regionen mit hoher Scherbelastung für die Blutzellen auftreten, wodurch die Blutzellen in diesen Regionen extrem beansprucht werden. Im zweiten Teil der Studie, als umgekehrter Fall zu den rotatorischen Blutpumpen (VAD-Systemen) in Bezug auf die Strömungscharakteristik, werden herkömmliche Dialysatoren untersucht. Trotz ihrer relativ geringen Scherbeanspruchung weisen sie z.B. im Vergleich zu den rotatorischen Blutpumpen eine längere Belastungspriode im künstlichen Organ auf , die die Notwendigkeit der Designoptimierung für eine minimale Bluttraumatisierung und infolge dessen eine höhere Hämokompatibilität hervorhebt.

Um die oben genannten Aspekte zu untersuchen, werden im ersten Teil der Arbeit die theoretiche-physiologiche Hintergrounde (Kapital 1-4) und anschliessend die Auswirkung des lokalen Hämatokrit-Wertes durch die Scherfeldverteilung auf die Hämolyse (Kapitel 5-6) beschrieben. Durch eine neue Hypothese, in der das Blut als ein mehrphasiges Fluid betrachtet wird, wird dieses Phänomen belegt. Die vorgeschlagene Hypothese basiert auf der regionalen Verteilung der Erythrozyten, in Analogie zu den physiologichen Verhältnissen, innerhalb solcher Vorrichtungen, die bisher noch nicht systematisch untersucht wurde. Zwei modifizierte

Taylor-Couette Apparaturen, realisiert durch zwei koaxiale Zylinder, „imitieren" die rotatorischen Blutpumpen. Die dabei entstandenen Blutgeschwindigkeitsprofile sind so konzipiert und realisiert , um die Ergebnisse von Scherfeldvariation auf die resultierende Hämolyse zu untersuchen. Darüber hinaus ist ein semiempirisches Hämolysemodell, das die Gewichtungen der Hauptphänomene im Hämolyseprozess berücksichtigt, entwickelt, um ein besseres Verständnis der Hämolysemechanismus darzustellen. Die vorgeschlagene Hypothese sowie das semiempirischen Hämolysemodell werden dann durch in vitro-Untersuchungen bestätigt, die mit frischem Human- und Schweineblut durchgeführt wurden.

Der Effekt der Filtrations- und Rückfiltrationsprozesse auf dem lokalen Hämatokrit in Dialysatoren und die anschließende Entstehung von Hämolyse, wird in dem zweiten Teil (Kapitel 7-9) untersucht. Mit Hilfe der Bilanzgleichungen sind semiempirische Modelle zur besseren Veranschaulichung der Fluid- bzw. Hämodynamik in den Dialyseverfahren entwickelt. Diese Modelle erlauben eine genaue Vorhersage des Hämatokritverlaugs, Blut- und Filterationsflussrate und Druckverläufe innerhalb des Dialysators. Zur Validierung der oben erwähnten semiempirischen Modelle werden in vitro-Untersuchungen unter Verwendung von Schweineblut für verschiedene experimentelle Untersuchungen durchgeführt.

Die Erkenntnisse dieser Studie, die mit großen experimentellen Daten validiert wurden, zeigen, dass die Hypothese scherinduzierte Zellmigration und Verteilung einen erheblichen Einfluss auf die resultierende Hämolysebestimmung hat und stellt einen Schlüsselfaktor für die Konstruktion und Designoptimierung von den blutführenden künstlichen Organen für die Leistungsoptimierung und gleichzeitige Minimierung der Blutschädigung und vertretbare Hämokompatibilität dar.

Table of Contents

Chapter 1

Introduction

1.1   Motivation

The rapidly increasing rate of demand for organ transplantation in past decade is mainly due to the increased incidence of organ failure, accompanied by an extreme organ shortage for transplantation. Consequently, the number of patients on transplant waiting lists has been increased enormously [1]. This fact is the strongest motivating force for the development and implementation of artificial organs. Artificial organs can be used either as a bridge to a living organ transplantation, or as a permanent organ replacement. Artificial organ design and development faces several other challenges aside from functionality, e.g. affordability and hemocompatibility in terms of attaining minimal blood trauma.

In spite of having achieved considerable progress towards its minimization, blood trauma still remains a serious problem for prolonged mechanical circulatory support of internal organs, e.g. ventricular assist devices (VADs), hemodialyzers and oxygenators [2-4]. Hemolysis is one of the most frequent expressions of blood trauma, and it is related to the functionality of red blood cells with the marker of free plasma hemoglobin. In addition to blood cell characteristics, hemolysis also depends on shear stress and exposure time, i.e. on hemodynamics [4].

Hemodynamics play a crucial role in medical devices, due to the prominent risk of achieving intolerable hemolysis levels, especially in the case of high shear devices, such as VADs, as well as in long term or permanent implantable devices, like heart valves. During dialysis, where extracorporeal non-physiological shearing is exerted repeatedly and for relatively long periods, blood trauma and hemolysis in particular should be monitored well. Although new trends and technologies are almost daily introduced in the field of dialysis treatment, such as the implementation of toxin absorbers and imprinted polymer nanoparticles, dialyzers using capillary membrane will remain the golden standard therapy for uremic patients in the foreseeable future.

Shear induced hemolysis in blood contacting devices has been investigated as early as the initiation of their clinical applications. However, the regional distribution of RBCs inside such devices, indicated as local hematocrit, has not been yet systematically investigated. It could potentially have a substantial impact on the resulting hemolysis, due to the dependence of viscosity on local hematocrit, which leads to the generation of different local shear stresses and eventually affects the regional distribution of RBCs through a feedback mechanism.

All the aforementioned points are nowadays considered obstacles in the way of blood trauma minimization in artificial organs, but also function as challenges and provide the motivation for this study to discover appropriate and applicable solutions to these problems.

1.2   Objectives and study goals

This study attempts to address the challenges in design optimization and hemolysis minimization in rotary blood pumps as discussed in the previous section. The main goal of this thesis is to present the phenomenon potential cell migration in the hemodynamics of artificial organs and consequently to evaluate its significance and its impact on total hemolysis. Intention of this study is to model the swiftly changing shear and flow pattern in a typical rotary blood pump, and to investigate the effect of cell migration on red blood cell trauma. The objective of this study, shear induced cell migration, was visually evidenced by stroboscopic pictures. A phenomenological semi-empirical model that quantitatively describes hemolysis is also introduced, in order to have a sophisticated insight considering the physical phenomena involved. The results of this study, presented in this thesis, can be directly applied in design optimization of commercially available rotary blood pumps, in pursuance of an improved hemocompatibility.

In contrast to the rotary blood pump, a blood contacting device with a very high shear rate (up to 40,000 s^{-1}) and low shearing time, dialyzer is a blood contacting device that has a very long exposure time and low shear rate. It is therefore selected for the evaluation of the significance of the mentioned objective as the extreme opposite case of the rotary pump. The effect of local hematocrit variation along the fibers' length is investigated for its hemodynamic characteristics alongside the potentially enhanced hemolysis rate near the area where backfiltration starts. Along these terms an analytical model predicting local hematocrit as well as pressure drop and blood flow rate in the dialyzer is presented in this study, in order to provide full understanding of the topic and to have an overview of the main parameters,. This model is validated by two cases utilizing different extracorporeal hemodialysis circuits. The results of this sections can inspire further research in the direction of optimizing the dialyzer's length and the number of its fibers, in order to achieve minimal hemolysis and maximal ultrafiltration rate at the same time.

1.3   Overview and structure of the thesis

This thesis aspires to make a contribution in this development and endeavors to

- Present a comprehensive theoretical approach in hemodynamics and hemorheology
- Explain cell migration phenomena in relation to physiological RBCs behavior in microcirculation
- Discuss the possible shear induced cell migration in artificial organs
- Investigate the effect of regional RBCs distribution on the resulting hemolysis in a typical rotary blood pump
- Define a new semi-empirical model for shear induced hemolysis
- Introduce three different analytical mathematical models that determine local hematocrit in a dialyzer
- Validate the above mentioned models by in-vitro investigations with commercially available dialyzers, adapted to the needs of this study

This thesis is structured in 11 chapters. In the present chapter the topic of the thesis and its structure are described. Furthermore, the outline and the goals of this study are defined addressing the highlighted challenges.

Chapter 2 explains the composition of blood and the function of its constituents, with a clear focus on hemorheology and the cell migration phenomenon. Blood cell damage and causes of hemolysis are also described in this chapter. Chapter 3 deals with rotary blood pumps and the shear field in such devices. In Chapter 4, artificial kidney, current therapeutic approaches used for dialysis patients, and the state of the art in this field, are described. This chapter will also be an introduction for the main technical terms required further on, in Chapters 7-9.

Chapter 5 is dedicated to the investigations on cell migration occurring in a Couette device that mimics the flow pattern in a rotary blood pump, as well as to the evaluation of this phenomenon and its effect on hemolysis. Established local hematocrits are visually inspected by means of stroboscopic photography of blood and other suspensions. A new semi-empirical and phenomenological model for blood hemolysis is introduced in Chapter 6. This model is applicable for both human and porcine blood. The experimental data originating from the Couette device experiments, are used to validate the model.

In Chapter 7, three mathematical models describing the filtration process of hemodialysis are introduced. One is founded on the usage of water as working medium, whereas the other two are addressed to blood.

Chapter 8 acquaints the reader with the experimental procedure pursued to prove the validity of the mathematical models introduced in chapter 7. In the first section (8.1), a hemodialysis circuit constructed for this purpose relies on a serially connected modules configuration. In order to provide additional evidence of the model's validity and reliability, a single dialyzer circuit is used in the investigation reported in the second section (8.2). The unique characteristic of this approach is that blood samples are obtained for hematocrit measurement directly from inside the fibers.

Likewise, Chapter 9 presents a third, validation method, and it outlines its applicability on the mathematical model for blood. A single dialyzer circuit has been employed in this occasion as well, but with the distinction of having the flows of the two fluids inversed.

Conclusively, Chapter 10 summarizes the whole work and compares the results obtained from in-vitro experimental data with those from models predictions. The contribution of this thesis and complementary future suggestions are disclosed at the end of Chapter 10.

Chapter 2

Rheological aspects of blood physiology

2.1   Overview of blood properties

The blood volume of an adult correlates with body mass and is typically 4-6 liters, with the rule of thumb of body weight over twelve. Blood is considered as a living tissue that circulates through circulation system including heart, arteries, veins and capillaries.

Blood is a multiphase fluid that is composed of blood cells suspended in an aqueous blood plasma which comprises about 55 % of blood fluid's volume. Around 99% of the blood cells consist of erythrocytes (red blood cells, RBCs) and the rest amounting less than 1% is leukocytes (white blood cells) and thrombocytes (platelets). Erythrocytes, the biconcave disc shaped red blood cells play a significant role in oxygen and carbon dioxide exchange[5]. Leukocytes or white blood cells are spherical cells that are part of the immune system[6]. Platelets, or thrombocytes are the smallest type of cells suspended in circulating blood. They are responsible for the initial formation of a plug to arrest bleeding and act as a catalyst in the blood coagulation process to fix the plug. In an inactivated state, platelets are smooth and biconvex disks[7].

Functions of blood: overview

The main functions of the fluid organ blood are 1) Transport function: transport of respiratory gases (oxygen, nitrogen and carbon dioxide), waste products of metabolism (water, urea), nutrients, hormones, enzymes and vitamins. 2) Buffering and regulation function (homeostasis): pH must be maintained in a range of $7.35 - 7.45$ and temperature at $37 \circ$C. Concentration of several substances suspended in blood has to be kept constant. 3) Defense function: elimination of foreign objects such as bacteria and viruses by means of phagocyte and antibody producing white blood cells. 4) Protection from blood loss (hemostasis): closing of an injured vessel due to complex processes involving platelet adhesion, aggregation, and blood clotting [8].

2.2   Blood cell properties

In biology and anatomy, a collection of tissues which performs a specific function or a group of functions is called an organ. By this definition blood is an organ[9].

Blood composition varies amongst people and between genders, whilst it also depends on age. In addition, health and nutrition continually affect the blood properties of each individual to some extent. Likewise, blood composition can be influenced by psychological factors (e.g. stress) and drugs. In general, blood volume comprises corpuscular components (RBCs, WBs and platelets) and plasma, in ratios of 45% and 55% respectively. Plasma consists of water at 92% per volume, and is therefore considered a Newtonian liquid with viscosity 1.16 - 1.35 mPa [10]. The remaining 8% contains dissolved substances such as proteins (albumin, globulin, fibrinogen etc.) and electrolytes (sodium, chloride, calcium etc.). A physiological concentration of plasma protein amounts to 7.3 g/dL, and the corresponding viscosity at body temperature is 1.46mPas [6].

Figure *2.1* displays the cellular components of blood in images taken with SEM. Platelets appear in their activated state.
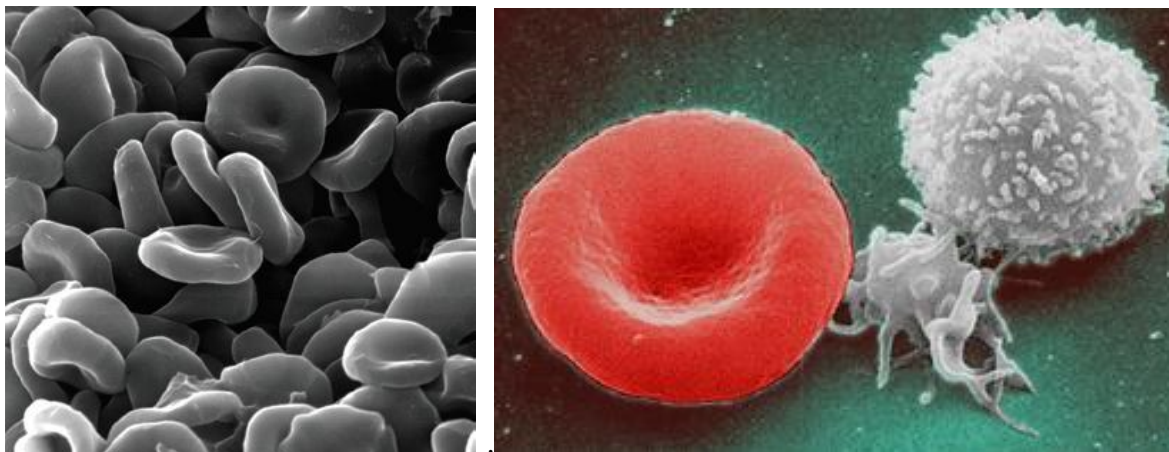
Figure 2.1: SEM of Blood cells A) Erythrocytes [11] B) Erythrocyte , activated platelet and white blood cell [12].

Table 2.1 contains information regarding the fundamental geometrical characteristics of erythrocytes, leukocytes and thrombocytes, along with their population in a cubic millimeter.

	Red blood cells	**White blood cells**	**Platelets**
Number of cells per mm^3	Male: 4.32-5.72* 10^6 Female: 3.90-5.03* 10^6 [13]	$4 - 10 * 10^3$	$140 - 400 * 10^3$
Diameter in μm	$6 - 9$	$7 - 20$	$2 - 4$
Volume in μm^3	$84 - 100$	$180 - 4200$	$4 - 10$
Cell shape	Biconcave and discoid	Spherical	Discoid (rest) Spherical (activated)

Table 2.1: Some characteristic data of main blood cells[14]

RBCs transport oxygen from the lung to body tissues and remove carbon dioxide from the body tissues. RBCs are well-adapted to resist shear stresses encountered under physiological conditions, e.g, when blood is pumped through arterioles or the network of narrow capillaries. When no external forces act on the membrane, a RBC takes the shape of an axisymmetric, biconcave, disk-like body. Because of its biconcave shape, a RBC has 40% excess surface area compared to a sphere of the same volume, enabling the cell to undergo deformations that preserve both volume and surface area. From a mechanical point of view the RBC can be described as an incompletely inflated bag (the plasma membrane) filled with a viscous fluid (the cytoplasm) [11].

The WBCs (leukocytes) are responsible for the body's defense against infectious disease and foreign materials as part of the immune system. WBCs have a particularly low life time of 5 - 21 days. Platelets (thrombocytes) are cells without a nucleus similar to RBCs. They play an important role during hemostasis. In case of injury they can adhere to the surrounding tissue or aggregate in order to close the wound [15].

2.3   Circulatory system and hemodynamics

The circulatory system consists of three independent systems that work together: the heart (cardiovascular), lungs (pulmonary), and arteries, veins, coronary and portal vessels (systemic). The system is responsible for the flow of blood, nutrients, oxygen and other gases, and as well as hormones to and from cells.
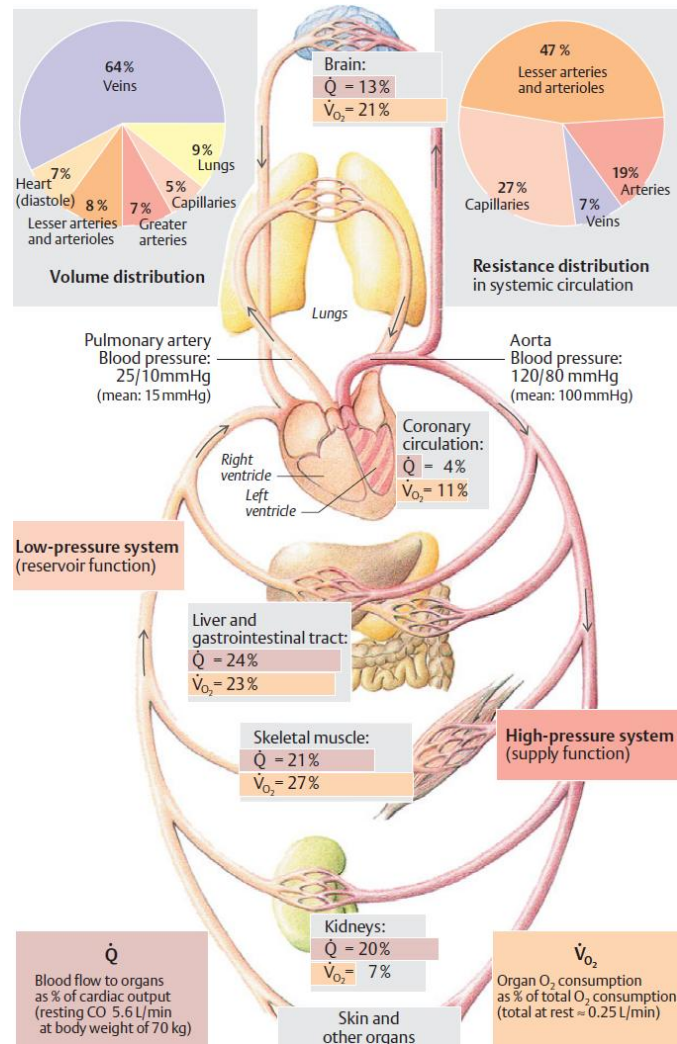
Figure 2.2: Schematic depiction of the circulation system indicating the delivered cardiac output and oxygen fraction for different organs [6].

The science dedicated to describe the physics of blood flow is called hemodynamics. For the basic understanding it is important to be familiar with anatomy of the cardiovascular system and hydrodynamics. Hereafter some hemodynamic features known in physiology of blood flow will be mentioned [16].

2.3.1   Red blood cell distribution in bifurcating vessels

Y. C. Fung in 1969 showed that distribution of blood cells inside the bifurcating vessels is influenced by velocity ratio and consequently hematocrit in the branch with faster flow properties becomes higher. Thence, the hematocrit decreases in the slower and increases in the faster branches. In other words there exist a varying local hematocrit value e.g. in aorta in comparison to smaller arteries and arterioles, which could be also transferred to the artificial blood conduits [17].

2.3.2   The Fahraeus effect and Fahraeus–Lindqvist effect

The finding that, for blood flowing steadily in tubes with diameters of less than 300 μm, the average hematocrit of the blood in the tube is less than the hematocrit of the blood in the reservoir feeding the tube is known as the Fahraeus effect. This effect is generated in the concentration entrance length of the tube, in which erythrocytes move towards the central region of the tube as they flow downstream. This entrance length is estimated to be about the distance that the blood travels in a quarter of a second for blood where red blood cell aggregation is negligible and the vessel diameter is greater than about 20 μm [18].

As the characteristic dimension of a flow channel approaches the size of the particles in a suspension; one should expect that the simple continuum model of the suspension will fail to be applicable. Often, this limit of the applicability of the continuum model begins to manifest itself at characteristic channel dimensions that are about 30 times the particle diameter: in the case of blood with a characteristic RBC dimension of 8 μm, an apparent failure occurs at about 300 μm. This was demonstrated by Fahraeus and Lindqvist, who found that the apparent viscosity of blood was a function of tube diameter, for diameters of 300 μm and less, when they flowed constant-hematocrit blood from a well-stirred reservoir through a tube. Changing of blood hematocrit and viscosity with the diameter of the tube it travels through is a physiological fact known as Fahreus–Lindqvist effect [19]; In particular a decrease of viscosity as the tube's diameter decreases (only if the vessel diameter is between 10 and 300 μm) is observed. This is because of axial migration of erythrocytes, leaving plasma at the wall of the vessel (see Figure 2.3).

This phenomenon can be explained by the concept of a plasma cell-free layer, a thin layer adjacent to the capillary wall that is depleted of red blood cells. Because the cell-free layer is

red cell-poor, its effective viscosity is lower than that of whole blood. This layer therefore acts to reduce flow resistance within the capillary, with the net effect that the effective viscosity is less than that for whole blood. Because the cell-free layer is very thin (approximately 3 μm) this effect is insignificant in capillaries whose diameter is large. This explanation, while accurate, is ultimately unsatisfying, since it fails to answer the fundamental question of why a plasma cell-free layer exists.
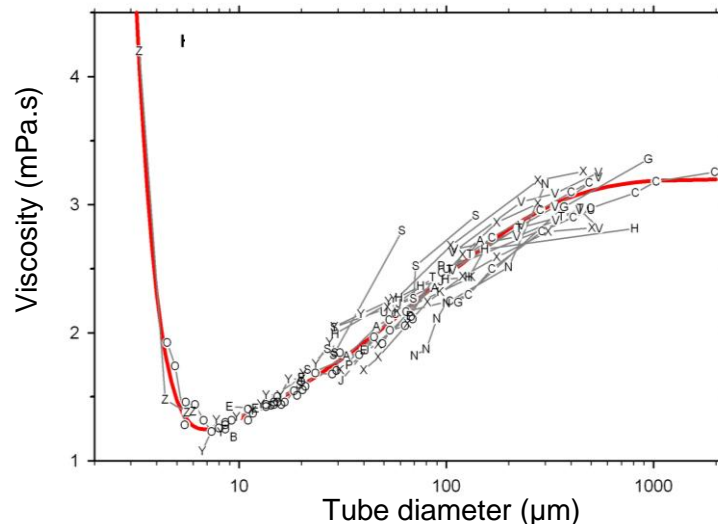
Figure 2.3: Relative apparent viscosity (normalized to plasma viscosity) as a function of tube diameter for flow of a RBC suspension with a discharge (or feed) hematocrit of 0.45; the red curve corresponds to best fit to data from several in vitro studies using photomicrographs of RBCs flowing through glass tubes of 3, 7 and 17 μm in diameter [20].

There are actually two factors which promote cell-free layer formation.

1- For particles flowing in a tube, there is a net hydrodynamic force that tends to force the particles towards the center of the capillary. This is known as the Segre–Silberberg effect [21]. There are also effects associated with deformability of red blood cells that might increase this force [22].

2- It is clear that red blood cells cannot pass through the capillary wall, which implies that the centers of red blood cells must lie at least one red blood cell half-thickness away from the wall. This means that, on average, there will be more red blood cells near the center of the capillary than very near the wall.
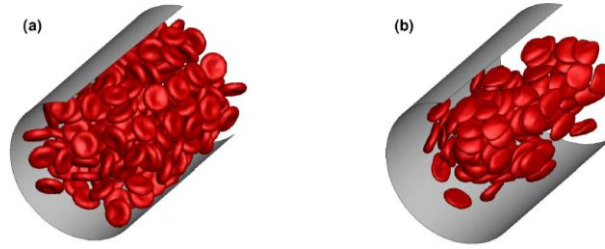
Figure 2.4: Simulation snapshots for D = 40 μm and hematocrit = 0.3. (a) Before the flow is applied, RBCs are distributed nearly randomly in the tube. (b) After the flow has converged for shear rate of 298 s^{-1}. The cell free layer region can be clearly seen[23].

The phenomenon of fluid dynamic separation, where a dilute suspension of neutrally buoyant particles traversing a tube in a laminar flow balances at a distance of 0.6 R from the tube's central axis, is better known as Segre–Silberberg effect, since it was first observed by Segre and Silberberg [21, 24]. Viscous drag forces are exerted on the buoyant solid particles, in addition to inertial lift forces. The drag forces act as pathways, keeping the particles from diverting away from the flow streamlines. The inertial forces on the other hand, influence the lateral position of the particles, thus affecting their homogeneous distribution.

The laminar velocity profile of a Poisseuille flow exhibits a parabolic nature, which generates a shear-induced inertial lift force that propels the suspended particles towards the tube's walls. The proximity of the solid particles to the wall generates a flow-induced pressure gradient, which forces the particles to certain distance from the wall [25]. The opposing lift forces depend on the ratio of particle diameter to the diameter of the tube (d/D), which as reported is dominant for d/D $\geq$ 0.07 [21].

Cell-free marginal layer has been modeled mathematically, in pursuance of explaining the Fahreus – Lindqvist effect [26].
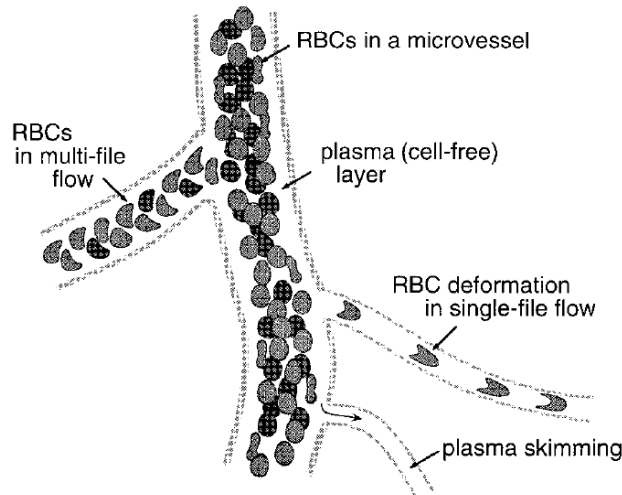
Figure 2.5: Marginal cell free layer formed by axial migration of red bloold cells[26]

2.4   Hemorheology

The study of the properties of the blood flow such as viscosity is called hemorheology. Blood behaves as a non-Newtonian fluid. The viscosity of blood varies with shear rate. This property allows it to become less viscous at high shear rates like during peak-systole and vice versa, during end-diastole, move more slowly and become thicker. This behavior classifies blood as a shear-thinning fluid.

2.4.1   Blood viscosity: effect of hematocrit and shear rate

Blood is a two phase fluid consisting of plasma and its dissolved gradients as well as cells (particles). Having a better approach it should be considered like a two phase fluid with the possibility of local and time dependent concentration of particles. The composition of blood can influence the flow behavior of blood. The flow of a fluid moving with a moderate speed can be thought to consist of fluid layers moving past other layers. Such a flow condition is called "laminar flow". In Couette flow between two parallel plates, one of which is moving relative to the other is laminar. For such flow pattern, in x-direction between two parallel plates, of which one is stationary while the other one moves with velocity $u_{(y)}$, as shown in Figure 2.6, the shear rate $\dot{\gamma}$ is defined as the velocity gradient [27]:

$$\dot{\gamma} = \frac{d\,u(y)}{dy}$$
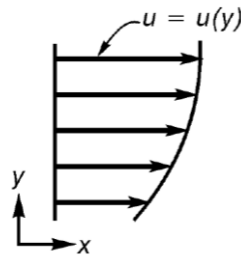
Figure 2.6: A velocity profile in which velocity changes only in y direction (normal to the u)[28].

For a large class of fluids the local shear stress is proportional to the shear rate.

$$\tau = \mu\dot{\gamma}$$

Where μ is the dynamic viscosity coefficient of the fluid, τ and $\dot{\gamma}$ are shear stress and shear rate respectively. This linear relation was first derived by Isaac Newton, hence such fluids are called Newtonian fluids. In some occasions, blood can be treated as a Newtonian fluid, but particularly in low shear ranges and in small capillaries behaves totally different.

Blood has extraordinary characteristics, described not only by fluid mechanics, but by physiological phenomena influenced by the existence of RBCs too. These phenomena along with the fluid mechanics of blood are thoroughly investigated in the multidisciplinary field of hemorheology.

The rheological properties of erythrocytes, such as deformability etc., are frequently affected by health disorders and extreme physiological conditions. Blood viscosity is a function of temperature and hematocrit, and it demonstrates a shear-thinning, nonlinear viscoelastic behavior that is greatly affected by the presence of red blood cells. Mottaghy et al. [29] proved the shear-thinning property of blood viscosity, by running in vitro experiments with human blood, where the apparent viscosity decreased when shear rate increased. In fact, blood can be regarded as a Newtonian fluid for shear rates higher than 250 s^{-1} at the physiological hematocrit of 45% (Figure 2.7). Of course blood plasma behaves as Newtonian fluid too in the absence of corpuscles (Hct = 0%), and its viscosity is nearly independent of shear rate [30].
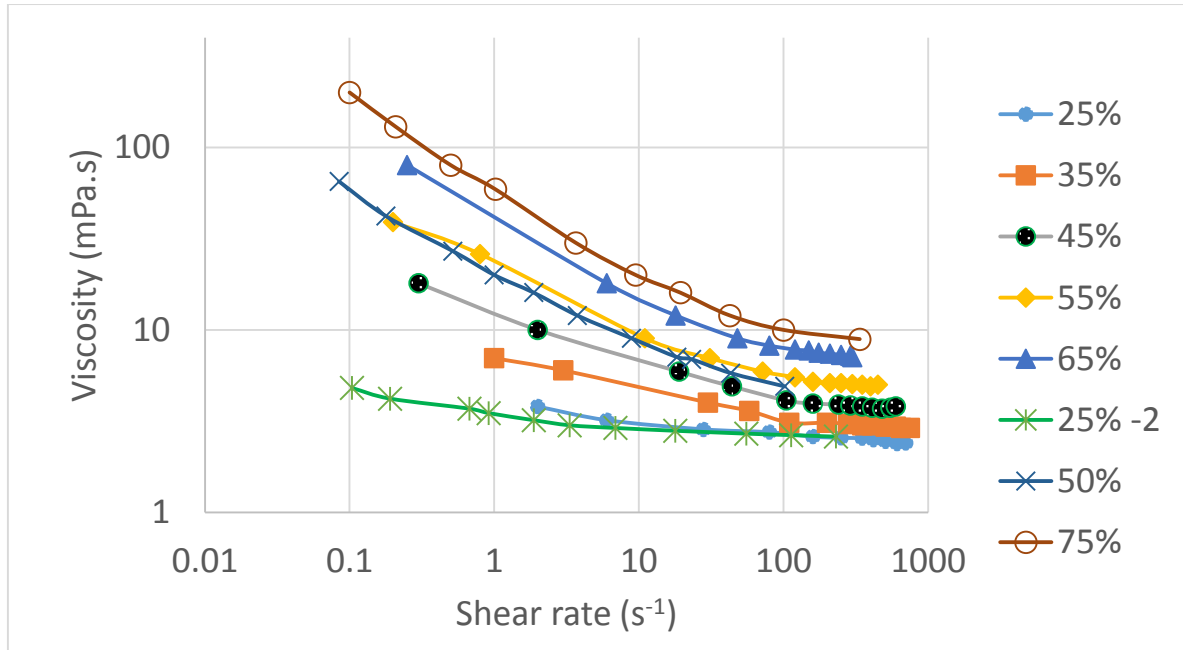
Figure 2.7: Dependency of dynamic blood viscosity for different hematocrits to function of the shear rate [31, 32]

When blood is pumped through a tube of small diameter (< 0.3 mm) the apparent viscosity decreases, in what is known as the Fahraeus-Lindqvist or sigma effect (see 2.3.2).

Another effect is the dependence of the hematocrit on the tube diameter, the so called Fahraeus effect (see 2.3.2). In addition, a cell-free layer near the wall as well as non-uniform distribution of cellular content and plasma at bifurcations can be observed. Those effects become more significant when the tube diameter becomes comparable to the diameter of a RBC [20].

As mentioned above the rheological properties of blood as a two phase fluid containing particles, various proteins and different electrolytes are very complex and not still fully understood. Therefore for modeling purposes some different approaches are presented. Hereafter some of the often used models will be described. It is frequently assumed that the viscosity of blood can be approximated by the Cross equation [33]

$$\frac{\mu_0 - \mu}{\mu - \mu_\infty} = (K\dot{\gamma})^m$$

where μ_0 and μ_∞ refers to the asymptotic values of viscosity at very low shear rates and at very high shear rates, respectively. K and m are constant parameters. For $\mu \ll \mu_0$ and $\mu \gg \mu_\infty$ the Cross equation by simplification of parameters reduces to the power-law model:

$$\mu = C\dot{\gamma}^{n-1}$$

where n is the power-law index and C is a parameter for consistency. Casson model is another alternative implemented in blood flow numerical simulations. The modified Casson model takes into consideration the dependency of blood viscosity on shear rate, and it can be expressed by a close approximation equation listed below [34]:

$$\mu = \left(\left(\frac{\sigma_{max}}{\dot{\gamma} + 1}\right)^{0.5} + \mu_c^{0.5}\right)^2$$

where the σ_{max} is the maximum yield shear stress and μ_c is the Casson viscosity. Various blood viscosity models have been proposed so far, including those that consider blood as an elastic Maxwell type fluid (elastic RBCs) mixed with a Newtonian fluid (plasma) [35]; however, the modified Casson model for human blood and power law model for porcine blood are the best available predictive models. For application of dialyzers the shear rate is fluctuating in the low shear range, therefore the assumption of constant blood viscosity can be extreme far from reality. In chapter 7, for validating of the experimental results with porcine blood, power law model is used.

2.5   Red blood cell damage

Red blood cell damage or hemolysis can be caused by different sources. It may be induced chemically by exposure to some lysing agent e.g. non-isotonic solutions and/or mechanically through exposure to shear stress in laminar and turbulent flows. The literature suggests that RBCs may be damaged by turbulence whose length scales are similar in size to an RBC, but may tolerate larger eddies[36]. Hemodynamics of medical devices is very important because of the risk possibility to make intolerable hemolysis, especially in the case of high shear devices such as VADs as well as long term or permanently use devices like heart valves. During dialysis in which the external non-physiological shear is exerted very frequent (3 times a week) and for relatively long time (typically 4 hours), blood trauma and particularly hemolysis should be monitored well.

Hemolysis generally addresses to the release of hemoglobin from RBCs. The sources of released hemoglobin can be from ruptured red blood cells as well as permeation through the cell membrane of unruptured RBCs (sub-lethal hemolysis). Changes in mechanical properties of blood cells such as red blood cell (RBC) deformability, RBC mechanical fragility, and

decrease in the concentration of plasma proteins are considered to represent a sub-lethal blood trauma [37]. The predominant expression of blood trauma in artificial organs such as VADs, is the mechanically induced hemolysis, caused by the sub-lethal damage of RBCs at shear rates above 42,000 s^{-1} [38], where the cell membrane is still un-ruptured, yet hemoglobin is leaking through the semipermeable membrane. This premature release of hemoglobin, shortens the normal life span of RBCs (~120 days for a healthy individual) [39]. Sub-lethal damage is a time dependent process, which necessitates time for the RBCs to undergo deformation. Further analysis on the subject of hemolysis is provided in Chapter 5.

The erythrocyte membrane, whether stretched due to cell deformation or not, is permeable to small molecules such as oxygen, carbon dioxide and water, but it does not permit the release of larger structures as hemoglobin and ADP [39]. However, if shear stress exceeds the threshold of 150 Pa, the membrane is stretched to such an extent that the pores open wide and larger molecules (e.g. hemoglobin, ADP etc.) leak into blood plasma. This blood trauma may be detected as hemolysis. It is worth mentioning that released ADP is itself a strong activator of platelets.

2.5.1   Fluid droplet behavior of erythrocytes

Erythrocyte deformation under the exertion of shear stress is similar to that of a liquid droplet, as reported by Schmid–Schönbein and Wells [40], who first established this analogy after suspending RBCs in a highly viscous continuous medium. Figure 2.8 features several instants of a human blood droplet suspended in silicon oil or (FC43) under increasing shear stress, which deforms the shape of the droplet, transforming it from spherical to ellipsoidal, until it eventually ruptures.
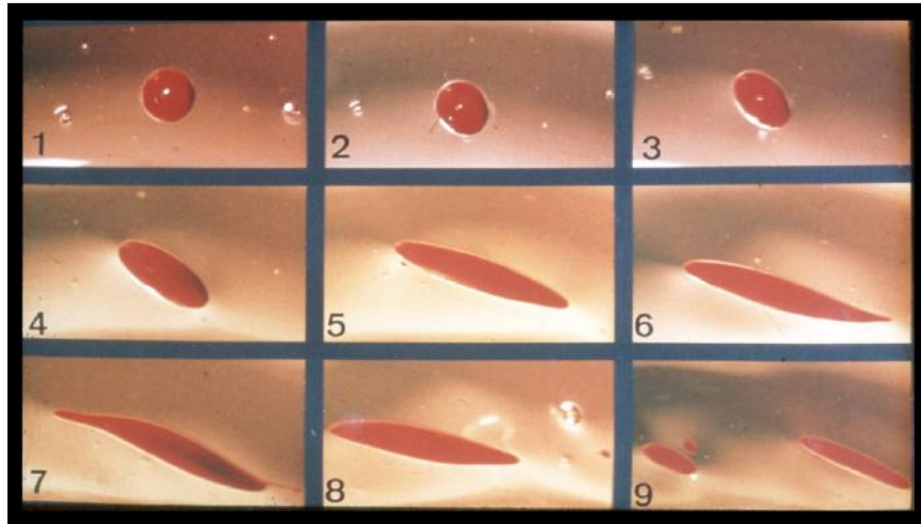
Figure 2.8: The deformation behavior of blood drops suspended in silicon oil. At rest the blood droplet has a spherical form. Under the influence of shear it deforms into an ellipsoid aligning with the direction of flow. Increasing further the shear, a bursting phenomenon can be observed in pictures 6 − 9[41].

Chapter 3

Blood pump systems

3.1   Different types of blood pumps

Blood pumps are used for extracorporeal support as well as ventricular assist devices (VAD) which might be implanted. Blood pumps used for extracorporeal support has been developed since 1855. Porter and Bradley patented in 1855 the first roller pump. Truax, who also distributed and promoted the Allen pump with one roller, developed the first double roller pump in 1899. After and application of a modified pump by DeBakey in 1934, in one of the first heart-lung machines constructed by Gibbon, DeBakey's name became inseparably attached to this type of pump. Nowadays, the roller pump is the most frequently used blood pump for cardiopulmonary bypass worldwide. In recent years, centrifugal pumps have increasingly competed with roller pumps as systemic blood pumps for cardiopulmonary bypass and have become the preferred arterial pump in a variety of centers[42].

Ventricular assist devices (VADs) are used to partially or completely replace the function of a failing heart. In general, VADs can be categorized into two main types: displacement pumps and rotary blood pumps. Displacement pumps, as their name denotes, displace a certain volume periodically, thus propelling the liquid. Rotary pumps, on the other hand, transfer energy directly to the fluid by means of velocity fluctuations caused by the vanes of the impeller [43]. Depending on the flow volume and pressure requirements of the application, either the one pump type, or the other will be favored: Rotary pumps being ideally suited for large flux volumes with low pressures, whereas displacement pumps generate high pressures even at low flow rates.

Displacement pumps such as roller pumps, have established themselves in the healthcare systems worldwide, after several decades of implementation in heart-lung machines (for cardiopulmonary bypass) and in hemodialysis, thanks to their reliability, operational simplicity and low cost of disposable conduit. Nevertheless, they cause some degree of blood trauma and particulate spallation. In contrast, rotary pumps offer smaller size, improved portability, reduced priming volume (total available volume for the recirculating liquid) and shorter accommodation periods in ICU, while they also claim lower blood damage rate, virtually negligible spallation, less bleeding and minimized neurological complications. In addition, their application can be extended up to several days, if necessary, whereas roller pumps are usually employed for a limited period (up to several hours) [44].

Rotary blood pumps can be classified into three main categories according to the impeller geometry: axial, radial (centrifugal) and diagonal (mixed flow) pumps. These pumps usually

preferred in applications with high flow rates (up to 20 l/min) and differential pressures lower than 500 mmHg. For such tasks axial pumps are the ideal candidates, whereas the radial design is the most efficient in producing high pressures and low flows. Finally diagonal pumps, being equally capable of high flows and high pressures, are often referred to as mixed flow systems [45].
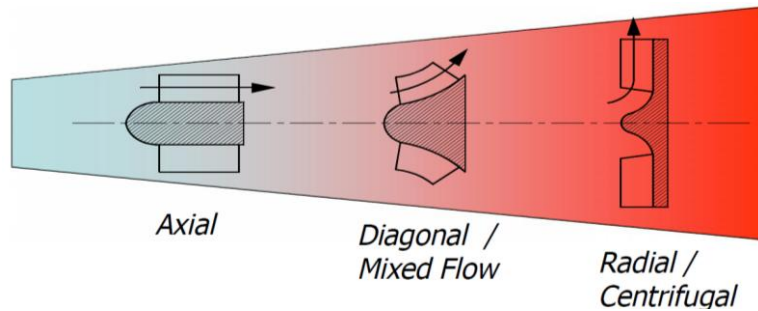
Figure 3.1: Schematic flow direction in axial, diagonal and centrifugal blood pumps

While differing in technical details, all state-of-the-art VADs have similar structure. They consist of a mechanical pumping device, an external power supply and an external control unit, as Figure 3.2 demonstrates.
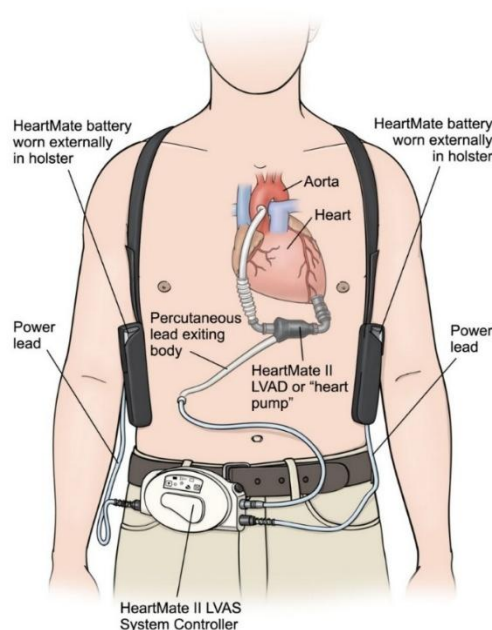
Figure 3.2: Overview of components of the HeartMate II LVAS[46].

3.2 Rotary blood pumps and blood trauma

A heart failure incident is usually followed by a gradual degeneration of the cardiac muscle, which directly affects its ability to propel blood in the circulatory system. End-stage heart failure can only be addressed with a heart replacement from a transplant donor, and it offers mid- to long-term relief. The substantial increase of heart transplantations performed in the 1980's, however, was not accompanied by an analogous boost in the availability of transplantable organs, thus limiting the number of performed operations. This organ shortage, along with the fact that not every donor's organ is compatible with any recipient's immune system, amplified the lack of transplantable hearts [47].
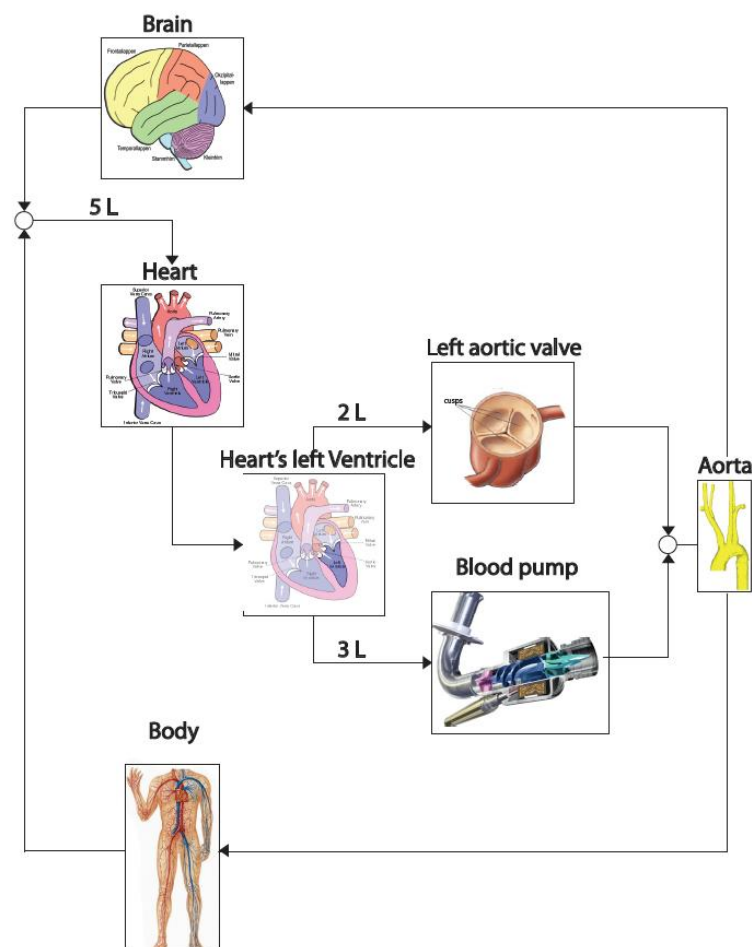
Figure 3.3: Blood flow circuit for a patient using LVAD (here MicroMed DeBakey axial blood pump)[12].

This hindrance triggered the development of mechanical circulatory support (MCS) devices that aimed at easing the effects of organ shortage by increasing pre-transplantation survival rates. The first type of MCS device is a Total Artificial Heart (TAH), which as its name

indicates replaces the patient's heart (the cardiac muscle is completely removed). This apparatus is capable of generating a full scale physiological blood flow (up to 10 l/min), and it serves as a "bridge-to-transplant", with remarkable results. Ventricular Assist Devices (VADs) are the other type of MCS devices, and they involve a significantly less invasive approach, as they are designated for cardiac support rather than total heart replacement. Implanted on the heart's left ventricle, a VAD pumps blood through a ventricular bypass at a rate of up to 10 l/min, thus effectively reducing the ventricle's workload. VADs are intended as "bridge-to-transplant" solutions too, and according to clinical data indications, they allow 50% – 66% of the patients to survive until a suitable donor organ is found [48]. Figure 3.3 demonstrates the exact function of a VAD, and the blood pumping workload shared between the implant and the impaired heart. Since the failing heart is not removed, VADs find application beyond the "bridge-to-transplant" principle. They are also used in "bridge-to-destination" therapies, where they offer some lifespan prolongation to patients with minimal chances of receiving a donated organ, and in "bridge-to-recovery" therapies, which aim at long-term recovery of the heart in pediatric and non-chronic heart patients [49] .

3.2.1 Shear field and hemolysis in rotary blood pumps

Besides pumping efficacy, mechanically induced hemolysis is a crucial designing criterion for rotary blood pumps. An obvious disadvantage of VADs is the local exposure of blood extreme non-physiological flow conditions, such as high pressures and shear rates. The MicroMed DeBakey pump for instance [50], has a widely varying pressure profile along the impeller as illustrated in Figure 3.4. Lowest pressure values (blue shading) correspond to a difference of $\delta = p_{local} - p_{atmospher} = -13.3\ kPa$ to the atmospheric pressure and are encountered at the blades' roots, whereas the highest values reach up to $\delta = 20\ kPa$ approximately, occurring on the tips of the impeller's blades.
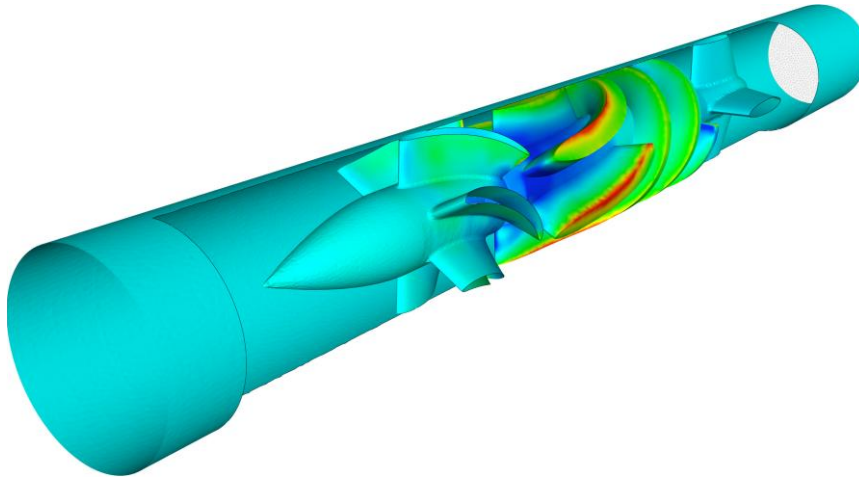
Figure 3.4: Pressure profile on MicroMed DeBakey VAD[50].

A peak atmospheric pressure difference of 16.0 kPa – 17.2 kPa is recorded as the physiological range of blood pressure at rest [51]. A pressure difference of 20.0 kPa corresponds to the condition classified as stage 1 hypertension, and is, in contrast to the case of medical hypertension, constantly exerted on the flow. The elevated shear-stress levels on the other hand, have proven to be aiding thrombus formation and hemolysis, both of which can rapidly deteriorate the patient's condition. Hemolysis may trigger splenomegaly and jaundice, while thrombus formation can lead to the buildup of clots, reducing the pump's performance or even causing it to fail, as Figure 3.5 indicates. In some cases, the developed thrombi can even cause thrombo-embolization, a life-threatening medical incident [52].

Figure 3.5: Thrombus formation in the different parts of MicroMed DeBakey VAD [52]

A systematic reduction of these events, and the revelation of the design tips in VADs typical geometry are the key points that are discussed comprehensively in chapter 4.

Chapter 4

Artificial kidney for kidney extracorporeal support

4.1   Introduction

One potential consequence of chronic kidney disease (CKD) is end-stage renal disease - ESRD (also known as end-stage kidney disease or end-stage kidney failure) that requires expensive renal replacement therapy in the form of dialysis or transplantation. Presently, over 2 million ESRD patients worldwide owe their lives to different dialysis related processes. This figure is expected to increase further by a growth rate of 6% annually [53]. Potential factors that can trigger a chronic kidney disease include: first and foremost age (older than 60 y.o.), hypertension, diabetes, cardiovascular diseases, and of course history of the disease in the family [54]. By acute renal failure, excess toxins that are normally regulated by kidney, must be removed and controlled "artificially". There are more than 20 molecules which their levels must be adjusted for uremic patients and urea is one of the most important molecules and has been recognized as a marker molecule to estimate the dose of dialysis therapy in order to indicate the efficiency of a dialysis treatment [55].

Several dialysis processes are currently being used for dialysis patients, among them, high and low flux hemodialysis are more frequent rather than other methods such as peritoneal dialysis, Hemodiafiltration etc.

The perspective of state of the art emphasizes that greater effort is placed in manufacturing with high levels of standard and possibly lower production costs as well as the possibility of reducing weight and residuals after disposal [56]. According to the present state of the art, new developments either in methods or devices must meet at least one of following parameters: innovative, simple and cheap or designed for individualized therapies [56]. Innovative technologies are noteworthy and attractive to create more and more sophisticated dialyzers for those countries in which hemodialysis has reached a high level of technology and the healthcare systems can afford the financial burden of such technological innovations. Miniaturization of dialysis system under the general concept of portable artificial kidney and some effort on Implantable or/and Bioartificial kidney are in this category, however these are still under research and development. The second category will be the development of simple and cheap dialyzers for those countries in which dialysis is not available for all patients yet. Individualized therapies to adapt the therapy to the specific physiological conditions of patients' kidney e.g. by means of a precise control of body water and its removal. This can be precisely monitored by bio impedance analyzes [56].

Beside the aforementioned criteria, hemolysis is still one of the main challenges of dialysis treatment methods. Ronco [57] showed filtration and backfiltration, which typically happens in hemodialyzers, can change the hematocrit along the fibers. This hematocrit changes may lead to change of viscosity and shear stress inside the blood flow and intensifies the sublethal blood trauma [37, 58]. The impact of this effect will be intensively and quantitatively discussed in chapter 7-9.

In this chapter, an introduction of renal function and related disorders (especially caused by local hematocrit) as well as current therapies and approaches esp. Hemodialysis is presented. Then, a glance to mass transfer phenomena in dialysis and defining relevant terms and concept is presented as a basis for chapter 7-9. In addition, new research and development approaches and trends also are mentioned.

4.2   Overview of renal function

Renal function is delivered by paired, fist-sized, bean-shaped organs, the kidneys, located behind the peritoneum against the posterior abdominal wall [6]. The kidneys serve several essential regulatory roles. The main separation functions of the kidney are [59]:

   i.   Eliminating the water-soluble nitrogenous end-products of protein metabolism
   ii.   Maintaining electrolyte balance in body fluids and get rid of the excess electrolytes
   iii. Contributing to obligatory water loss and discharge excess water in the urine
   iv.   Maintaining acid-base balance in body fluids and tissues

Kidneys processes blood, or rather plasma, to be more accurate, in order to fulfill these functions. The concentration of solutes in body fluids varies significantly, depending on the location, yet all the compartments maintain remarkably constant in volume and composition, in spite of internal and external stresses. The general outcome of normal renal function is a net disposal of water, electrolytes, and soluble waste products from the blood stream. In other words, kidney is in charge of the major regulatory mechanisms that control volume, osmolality, electrolyte and nonelectrolyte composition, as well as pH of the body fluids and tissues [6, 8].

Each kidney is consists of a multitude parallel mass transfer units (over a million), which are all nourished from the renal arteries, and subsequently return the processed blood to the systemic circulation through the renal veins, while simultaneously they collect waste liquid and solutes through the calyx of each kidney into the ureter and from there into the urinary bladder

[6, 60]. These functional units are called nephrons and can be regarded as a sequential arrangement of mass transfer mechanisms i.e. glomerulus, proximal tubule, and distal tubule (see Figure 4.1) between two fluid streams: blood and urine.
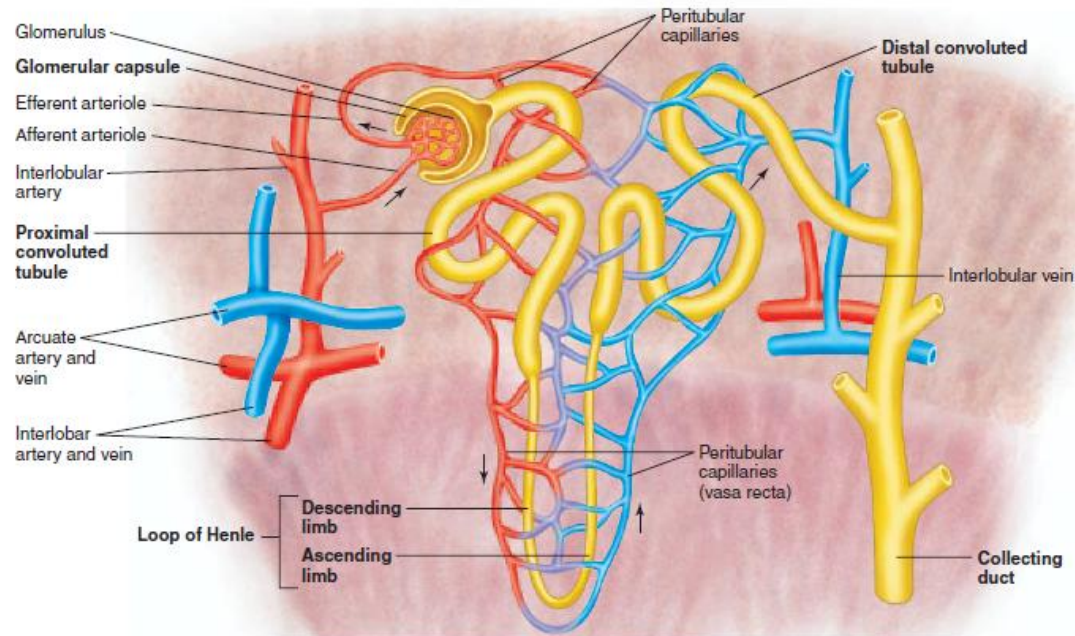
Figure 4.1: The nephron tubules and associate vessels[8].

Kidney function is facilitated by several mechanisms, and each substance is cleared via an individual mechanism that take place along the nephron tubules (see Figure 4.2). In fact, kidney takes advantage of two major mass transfer phenomena: ultrafiltration, which results in the separation of large amounts of extracellular fluid through plasma filtration in the glomeruli, and a combination of passive and active tubular transport of electrolytes and other solutes, together with the water in which they are dissolved, in the complex system provided in the rest of the nephron.
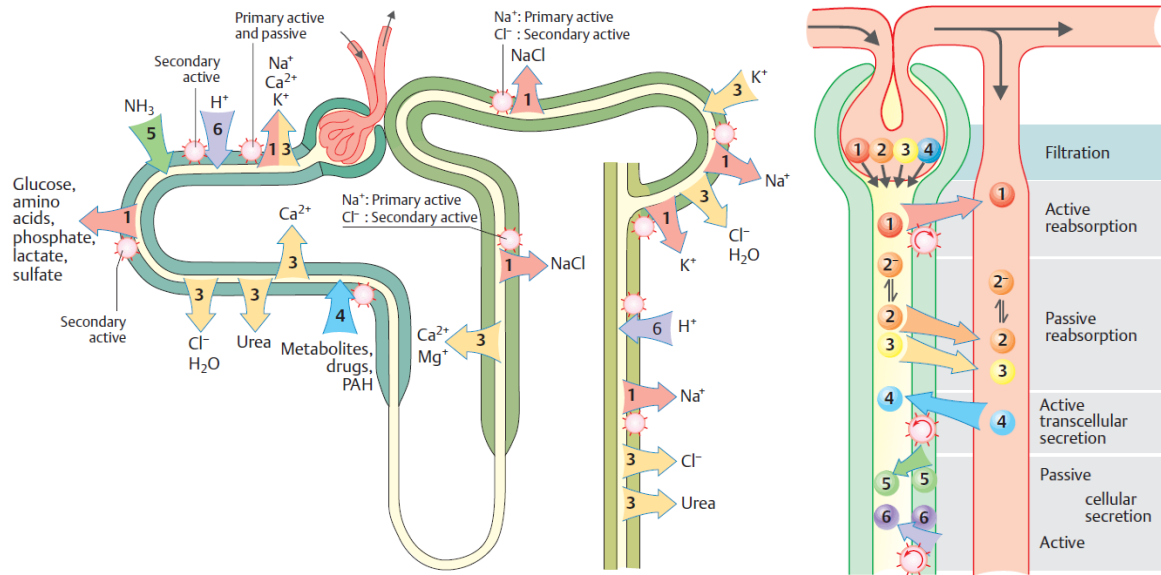
Figure 4.2: Overview of important transport processes along the different parts of nephron (right), Tubular transport mechanisms (left)[6].

Toxins to be removed

The uremic retention solutes that need to be removed from the patients' blood stream, in cases of acute or chronic renal failure, are commonly referred to as uremic toxins. Chief amongst them are urea, creatinine and uric acid – all of them waste products with low molecular weight (60 ~ 186 Da) – perpetually generated by protein metabolism. Other toxins less frequently encountered due to lower concentrations, demonstrate significantly higher molecular weight (500 ~ 40,000 Da), bordering the cut-off limit of the glomerular membrane. They are therefore named "middle molecules" (MM) [61], and despite having an unidentified specific toxicity, are often the topic of research since experimental evidence has proven their implication in renal failure pathogenesis [62]. The low molar concentration of "middle molecules" indicates an improved disposal by convection in comparison to diffusion. Solutes with molecular weight greater than the cut-off limit of the membrane are not be disposed through the membrane, yet in some diseases, primarily non-renal, they have to be eliminated by means of artificial methods (e.g. apheresis, or hemoperfusion). Such substances can be lipoproteins, antibodies of specific diseases (e.g. autoimmune diseases) and protein-bound endogenous and exogenous toxins.

 The "European Uremic Toxin Work Group" has systematically been studying the uremic toxins, and classifies them accordingly under small, middle and large molecular weight categories [62]. Solutes with molecular weight less than 500 belong to the small molecule class,

whereas those with molecular weight between 500 – 40,000 constitute the middle molecule category. Finally, substances of MW > 65,000 fall into the large molecule group. Some of the most common and frequently studied uremic toxins have been selected and their key properties are featured in Table 4.1, Table 4.2 and Table 4.3.

Solute	MW	C_P(mmol/l)	C_{MU}(mmol/l)	C_{max}(mmol/l)
Urea	60	<6.7	38.3	76.7
Oxalate	90	$3.33 * 10^{-3}$	0.05	0.08
Creatinine	113	<0.11	1.20	2.12
β- guanidinopropionic acid	131	$<2.5*10^{-5}$	$2.2 *10^{-4}$	$5.0 * 10^{-4}$
α-keto-o-guanidinovaleric acid	151	$<2.0*10^{-4}$	n.a.	$9.3*10^{-4}$
Uric acid	168	<0.4	0.50	0.87
Guanidonosuccinic acid	175	$1.7*10^{-4}$	0.04	0.27
l-methylinosine	179	$<2.8*10^{-5}$	$1.4*10^{-3}$	$2.6*10^{-3}$
Xanthosine	284	$8.4*10^{-5}$	$3.4*10^{-4}$	$7.8*10^{-5}$
N^2, N^2 -dimethylguanosine	311	$2.9*10^{-5}$	$7.6*10^{-4}$	$1.3*10^{-3}$

Table 4.1: Low molecular weight uremic toxins (based on[62]), C_P: normal plasma concentration, C_{MU}: mean plasma concentration in uremic patients, C_{Max}: maximal plasma concentration in uremic patients.

Solute	MW	C_P(mmol/l)	C_{MU}(mmol/l)	C_{max}(mmol/l)
Neuropeptide Y	4 272	$<1.9*10^{-8}$	$1.5*10^{-8}$	$2.7*10^{-8}$
β2 microglobulin	11 818	$<1.7*10^{-4}$	$4.7*10^{-3}$	$8.5*10^{-3}$
Cystatin	13 300	$<1.2*10^{-4}$	$8.9*10^{-4}$	$1.5*10^{-3}$
Interleukin-6	24 500	$5.4*10^{-10}$	$3.8*10^{-9}$	$1.3*10^{-8}$
κ-Ig light chain	25 000	$1.4*10^{-3}$	$2.8*10^{-3}$	$1.1*10^{-2}$
Tumor necrosis factor-α	26 000	$5.1*10^{-10}$	$4.4*10^{-9}$	$1.6*10^{-8}$
Interleukin-1β	32 000	$<5.0*10^{-9}$	$1.3*10^{-8}$	$5.3*10^{-8}$

Table 4.2: Middle molecular weight uremic toxins (based on [62]), C_P: normal plasma concentration, C_{MU}: mean plasma concentration in uremic patients, C_{Max}: maximal plasma concentration in uremic patients.

Solute	MW	C_P(mmol/l)	C_{MU}(mmol/l)	C_{max}(mmol/l)
Methylglyoxal	72	$6.5*10^{-4}$	$1.5*10^{-3}$	$2.0*10^{-3}$
Putrescine	88	$2.4*10^{-4}$	$8.8*10^{-4}$	$1.5*10^{-3}$
p-cresol	108	$5.6*10^{-3}$	0.19	0.38
Homocysteine	135	<0.01	0.06	0.20
Hippuric acid	179	<0.03	1.38	2.63
Indoxyl sulfate	251	$2.4*10^{-3}$	0.21	0.94
Pentosidine	342	$1.5*10^{-4}$	$2.6*10^{-3}$	$8.7*10^{-3}$
Leptin	16 000	$5.3*10^{-7}$	$4.5*10^{-6}$	$3.1*10^{-5}$

Table 4.3: Protein bound toxins (based on [62]), C_P: normal plasma concentration, C_{MU}: mean plasma concentration in uremic patients, C_{Max}: maximal plasma concentration in uremic patients.

Although in this study, the focus points is on the hematocrit change (concentration of the blood cells), but the concentration of the other toxins especially those with high molecular weight which has a low transfer rate is very similar to the hematocrit. This issue will be discussed later.

4.3 Renal failure and need for therapy

The first signs of renal insufficiency become apparent when GFR, which is usually measured by creatinine clearance, falls significantly below the one third of the normal value [59]. In that stage, plasma and/or the extracellular concentration of uremic toxins that can only be disposed via the glomeruli (e.g. creatinine and urea) increase dramatically. The latter can be a sign of progressive renal failure, which translates into a continuous decay of renal function over a period of months to years. This decay is accompanied by the loss of waste product excretion ability, the inadequate osmoregulation, and the subsequent imbalance in water and electrolyte concentrations. ESRD is diagnosed by the excessive levels of creatinine (approx. 15 mL/min), which in conjunction with the retention of water and solutes oppressing the cognitive CNS functions trigger a uremic coma reaction. An empirical assessment of a viable creatinine clearance would set the minimum level at 8 mL/min (i.e. 11.5 L/day or 80 L/week[1]) [59].

Total absence of renal function limits the lifespan of an otherwise healthy individual to 7-10 days. However, as clinical practice indicates, even a minimal residual renal clearance (K_R), below the level necessary for survival, can prove substantial for the wellbeing of uremic patients, perhaps because the natural kidney, however sick, remains capable of eliminating middle molecular weight substances, whereas the artificial kidney is mostly effective in eliminating water and small molecules.

4.4 Moschcowitz syndrome

Moschcowitz syndrome, also known as Thrombotic Thrombocytopenic Purpura (TTP), is a rare disorder of the blood-coagulation system, causing the formation of wide microscopic clots in the small blood vessels all over the body [63, 64]. These clots, scientifically termed thrombi, can have a detrimental effect on the internal organs, especially on the heart and brain. The development of an effective treatment for these thrombi with plasma exchange brought the fatality rate from 90% to 10% [65].

Most TTP incidents are directly related to the inhibition of ADMATS13 enzyme, a metalloprotease that cleaves large multimers of von Willebrand factor (vWF) into smaller units. The elevated number of vWF multimers in the bloodstream, trigger an augmented platelet adhesion in areas of endothelial injury, especially at arteriole-capillary junctions.

---

[1] These figures correspond to the definition of adequate dialysis in ERSD patients, representing the time-averaged clearance achieved by a much more effective but intermittent blood filtration process.

Any erythrocytes passing near the micro-clots are subjected to membrane damage due to high shear stress that eventually leads to an uncontrolled rupture, causing anemia and schistocyte formation. Furthermore, thrombosis and cellular injury wane the blood flow, which results in organ failure. Contemporary therapy relies on renal support and plasmapheresis, in order to reduce the amount of circulating ADAMTS13 antibodies, and to restore the normal blood levels of the enzyme [66]. This disorder is worth mentioning because of the non- physiological flow conditions, and the activation of platelets in small vessels that leads to mechanical blood damage. It is a naturally occurring case related to the topic of the present study, where mechanical blood trauma takes place in the body resulting in the formation of micro clots.
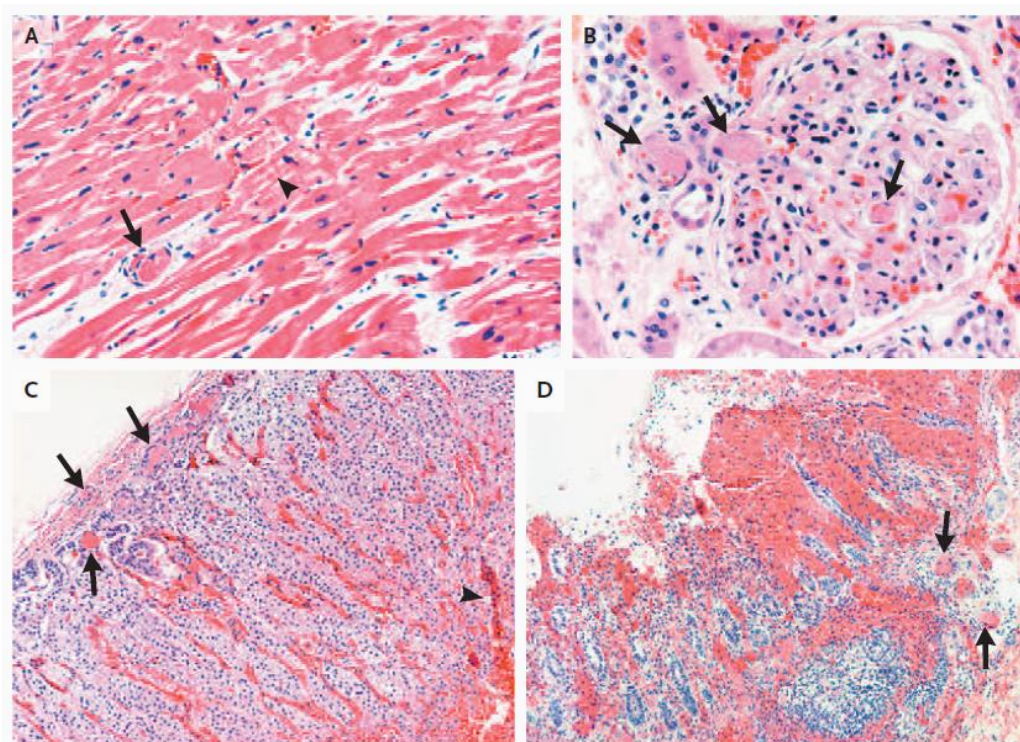
Figure 4.3: Tissue Specimens Obtained at Autopsy from a Patient with Abnormalities Characteristic of Thrombotic Thrombocytopenic Purpura[65], A specimen from the heart (Panel A) shows multiple intra myocardial micro thrombi (arrow), hemorrhage, and early ischemic changes, with scattered foci of contraction-band necrosis (arrowhead). A specimen from the kidney (Panel B) shows characteristic micro thrombi in an afferent arteriole, the glomerular hilum, and glomerular capillaries (arrows). A tissue specimen from the adrenal gland (Panel C) shows characteristic subcapsular micro thrombi (arrows), with congestion of cortical arterioles and medullary parenchymal hemorrhage (arrowhead). A specimen from the cecum (Panel D) shows submucosal micro thrombi (arrows).

4.5 Treatment of renal failure and renal transplantation

4.5.1 History

Abel, Rowntree, and Turner of Johns Hopkins Medical School are considered the founding fathers of dialysis, since they first managed with their experiments to remove toxic substances from blood and drain excess water volume, through an exchange process and with the implementation of a membrane [67, 68]. Until the first half of 20th century, uremia was a fatal condition that could be triggered either by an acute episode of renal failure or by the chronic progressive deterioration of kidney function. These pioneers first demonstrated the feasibility of dialysis in 1913, as a technique of balancing solute concentrations in plasma with those in an appropriately formulated washing solution. This observation was not accompanied by any clinical application for various reasons, chief amongst them: the fabrication limitations imposed by the difficulty of manufacturing suitable exchange membranes, and the precarious blood anticoagulation methods existent at that time. The sole synthetic permeable membrane material available at the dawn of 20th century was Collodion, a nitrocellulose film precipitated from an alcohol, ether, or acetone solution (cellophane was invented in the 1930s). Heparin was also unknown at the time, and the obtainable anticoagulants made continuous blood processing a hazardous process even in laboratory animals.

The first artificial kidney was developed in 1944, by the Dutch Kolff consisting of a long segment of cellophane sausage tubing coiled around a drum rotating in the thermo-stabilized bath filled with a hypertonic, buffered electrolyte solution, called dialysate. This device had adequate yet marginal capacity to treat human acute renal failure.

Inouye and Engelberg (1953) invented a coiled cellophane tube arrangement as an upgrade to Kolff's device that was stationary and disposable. Soon, Kolff and Watschinger (Cleveland Clinic) reported a variant of this design, the Twin Coil, which became the standard in clinical practice for the following years.

Repeated treatment required for chronic renal failure, was materialized in 1959 by Scribner and Quinton, who introduced techniques for prolonged access to the blood stream. The latter, combined with improvements in the design and the application of hemodialysis equipment, permitted the implementation of chronic intermittent hemodialysis for long-term preservation of ESRD patients[69]. At the same time Kiil reported the outcome of his research with a flat plate dialyzer design, where blood would flow between two sheets of cellophane supported by solid mats with grooves for the circulation of dialysate [70]. This design – initially developed

by Skeggs and Leonard, McNeill, and Bluemle and Leonard – not only required less blood volume to operate, but also achieved blood/dialysate circulation with a relatively low pressure difference [71]. In contrast to coil dialyzers, where a long blood path necessitated a high blood pressure at the exchanger's inlet, flat plate dialyzers facilitated metabolite mass transfer across the membrane by diffusion alone, without the obligatory water flux deriving from high transmembrane pressure. When ultrafiltration (net filtrate volume permeated through membranes with a purely convective transport) was necessary, circulating the dialysate at sub atmospheric pressures would do the trick. The growing number of home dialysis patient, augmented the invention and optimization of such devices.

By 1965, the first mass produced home dialysate preparation and control units were commercially available industrially. Soon thereafter home dialysis programs based on the twin coil or flat plate dialyzers ensued. At that time home treatment would cost considerably less than hospitalization, and in the United States, Social Security would not yet cover the cost of ESRD therapies.

In the same year, Bluemle and his colleagues studied the optimal way of packing the maximum membrane area in the minimum volume, in order to reduce the size of the exchange device and minimize the priming volume [71]. The outcome of their survey was a tightly packed bundle of parallel capillaries. By 1967, Lipps and associates reported the first clinical experience with hollow fiber dialyzers, which have since dominated hemodialysis technology [72].

Concurrently, Henderson and associates (1967) proposed an alternative solution to the limited mass transfer achieved with hemodialysis equipment by diffusion alone [73]. They advocated that a purely convective transport (ultrafiltration) through membranes more permeable to water than the original cellulose would increase the effective clearance of metabolites larger than urea. The lost extracellular volume would be replaced by infusing large volumes of fresh saline into the blood at the inlet or the outlet of the dialyzer, to replenish the lost water and electrolytes. The process was termed Hemodiafiltration or, sometimes, diafiltration. It becomes apparent that the efficacy of hemodialysis with a given device depends on the duration of the procedure. Nowadays, intermittent maintenance dialysis can be offered in treatments of 10 hours (or less) divided in 3 sessions per week.

In 1976, Popovich and Moncrief described the procedure of continuous ambulatory peritoneal dialysis (CAPD), where lavage of the peritoneal cavity is conducted as a continuous form of mass transfer through introduction, equilibration, and drainage of dialysate on a repetitive basis

4–6 times a day [74]. A sterile solution containing electrolytes and dextrose is fed without a pump (only gravitational forces) into the peritoneal cavity through a permanently installed transcutaneous catheter. After equilibration with capillary blood over several hours, this dialysate is drained by gravity into the original container and the process is repeated with fresh solution. During the dwell periods, toxins and other solutes are exchanged by means of diffusion, whereas water transfer is induced by the osmotic pressure difference due to the high dextrose concentration in the treatment fluid. However, the cost of providing fresh plasma to replace the discarded material renders plasmapheresis impractical for frequent, repeated procedures, and plasmapheresis is mainly employed for other clinical indications.

4.5.2   Current approaches

The main dialysis treatments currently offered by the majority healthcare systems can be listed as hemodialysis, hemofiltration and hemodiafiltration. Here, these techniques will be described fine differences between the various methods will be explained.

4.5.2.1   Hemodialysis

Hemodialysis is a process in which clearing the blood of toxic substances and electrolytes adjustment while removing excess water by a membrane exchange process is driven by diffusion along a concentration gradient across a semipermeable membrane (see Figure 4.4). Mass exchange is performed in the hemodialyzer. A semi-permeable membrane compartmentalizing the two fluids, blood and dialysate, by permitting the crossing of small and medium solutes and by cutting off the larger ones. Depending on the molecular weight cut-off (MWCO) of the membrane so called low-flux (molecular cut-off at about MW 10000) and high-flux (molecular cut-off at about MW 60 000) membranes are used. The dialyzer is perfused in an extracorporeal circuit on one side of the membrane with the blood of the patient at a rate of 200 to around 400 ml/min. On the other side of the membrane the dialyzer is perfused with the dialyzing fluid at a rate of 500 ml/min in a countercurrent mode in order to maximize solute exchange rate [75]. In such a way, the main marker toxins, e.g., urea, creatinine, will be eliminated from the patient's bloodstream after a time consuming therapy session. The dialyzing fluid contains sodium, potassium, calcium, magnesium, chloride,

glucose and bicarbonate under a defined concentrations to regulate the electrolytes during the treatment.

However, the excess water defined as the difference between the wet weight (patient weight before starting the treatment) and dry weight (weight after last dialysis session) is not effectively discarded by diffusion, and if it remains untreated may cause hypervolemia and various edemas (peripheral, pulmonary, etc.). For these purpose, the semi-permeable membrane is equipped with a secondary mechanism, ultrafiltration. This procedure has a convective nature, since fluid crosses through pores from the one side of the membrane to the other. The driving force for ultrafiltration is the pressure gradient between the two sides of the membrane, generated by the roller pumps propelling the two liquids. In the other word, hemodialysis is not only run with a pure diffusion mechanism but also it is integrated by a convection mechanism.
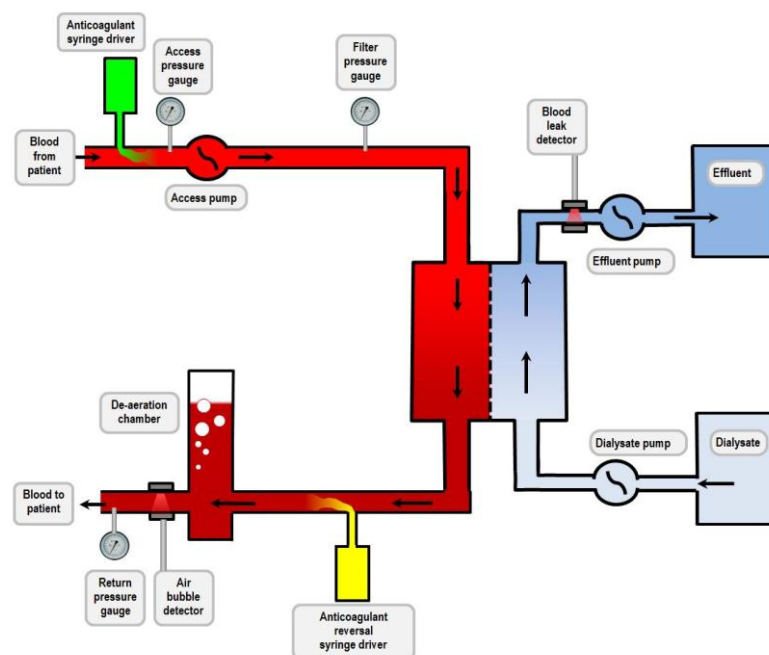
Figure 4.4: Schematic presentation of a hemodialysis extracorporeal circuit (based on [76]).

Osmosis and the reverse osmosis, principally made by blood proteins that cannot travel through the membrane, play a part mostly in connection to ultrafiltration in hemodialysis. In an attempt to balance the concentration of such substances inside and outside the hollow fibers, a certain amount of liquid from the outside compartment penetrates the membrane and dilutes the fluid within, thusly reducing the concentration of said substances[77]. This mechanism is frequently

met in nature, and as a matter of fact the cells of the human body use it abundantly to adjust their content in agreement with the status of their environment [78].

4.5.2.2   Hemofiltration

Hemofiltration has a purely convective nature imitating the filtration process in the glomerulus of the natural kidneys and it achieves the desired elimination of some middle molecular weight toxins as well as low molecular weight ones from the bloodstream by draining large amounts of plasma. Hemofilters have larger pores in comparison to hemodialyzers, which increase sieving coefficient by permitting more liquid and solutes of higher molecular weight to depart the bloodstream. Depending on the TMP, all solutes smaller than the membrane pore size pass the filter with nearly the same concentration as in the blood depending on their sieving coefficients (SC). In this direction the rest of the extracorporeal circuit is also designed to compensate the filtered volume as Figure 4.5 illustrates. Hemofilter clears blood from solutes of a higher molecular weight spectrum including very low concentrated uremic toxins that may be responsible for severe uremic symptoms.

Dialysate is not required in this treatment, therefore the respective inlet is either completely omitted or blocked. The pump designated for dialysate circulation is reallocated to the filtrate outlet, where it produces negative pressure (suction) that increases filtration through the capillary membrane.

To prevent dehydration of the patient due to the excessive liquid discharge, a replacement fluid is infused directly in the blood line, before and/or after the hemofilter. The fluid administration prior to the filter dilutes the erythrocyte concentration in blood, and avoids reaching extreme values during the filtration process that might consequently affect the hemorheological properties of the flow. Likewise, the post-dilution is necessary to restore hematocrit to nominal levels and to top-up blood with the essential solutes and nutrients that are eliminated by the hemofilter. The composition of the fluid includes isotonic solution and some bicarbonate generating base (e.g. lactate, acetate or bicarbonate itself) [79].
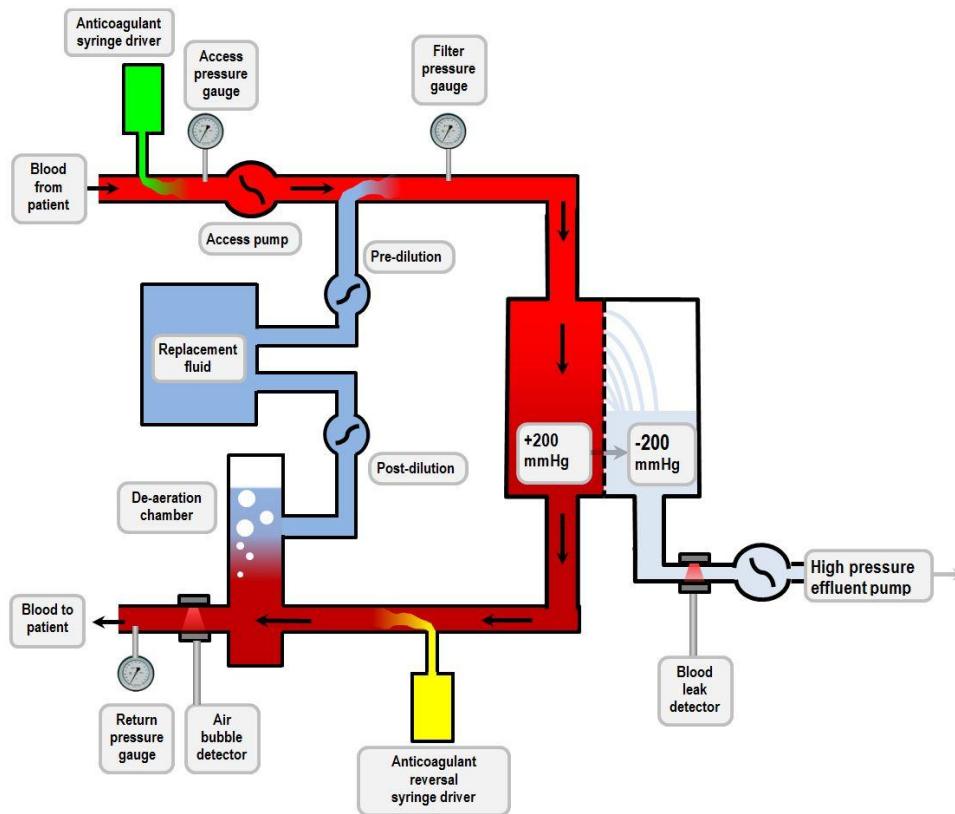
Figure 4.5: A schematic presentation of the extracorporeal circuit for Hemofiltration therapy (based on [76]).

Hemofiltration therapy is serves in two modes: intermittent and continuous. Intermittent is suitable for outpatients visiting the hospital every two days to receive a treatment lasting 3-5 hours. Continuous hemofiltration, as described by Kramer et al [80], is offered by intensive care units and addresses patients suffering from excessive accumulation of liquid in their bodies. Further variations of this therapy arise from the distinction of the vessel blood originates from and returns to (artery/vein). Hence, CVVH refers to continuous veno-venous hemofiltration, whereas CAVH indicates an arterial blood supply.

4.5.2.3 Hemodiafiltration

Hemodiafiltration (HDF) combines the low-molecular-weight solute clearances achieved in hemodialysis through a diffusive solute transport and the relatively higher clearances of the larger uremic toxins (so-called middle molecules) as achieved with hemofiltration through a convective solute transport. Therefore HDF provides considerable advantages over both hemodialysis and hemofiltration in which small and large solutes are removed efficiently[81].

Since dialysate is also used in this treatment, the layout of the homologous subsystem of the extracorporeal circuit (Figure 4.6) is identical to that of a hemodialysis circuit. The synchronous implementation of dialysate and replacement fluid raises the cost of this therapy.
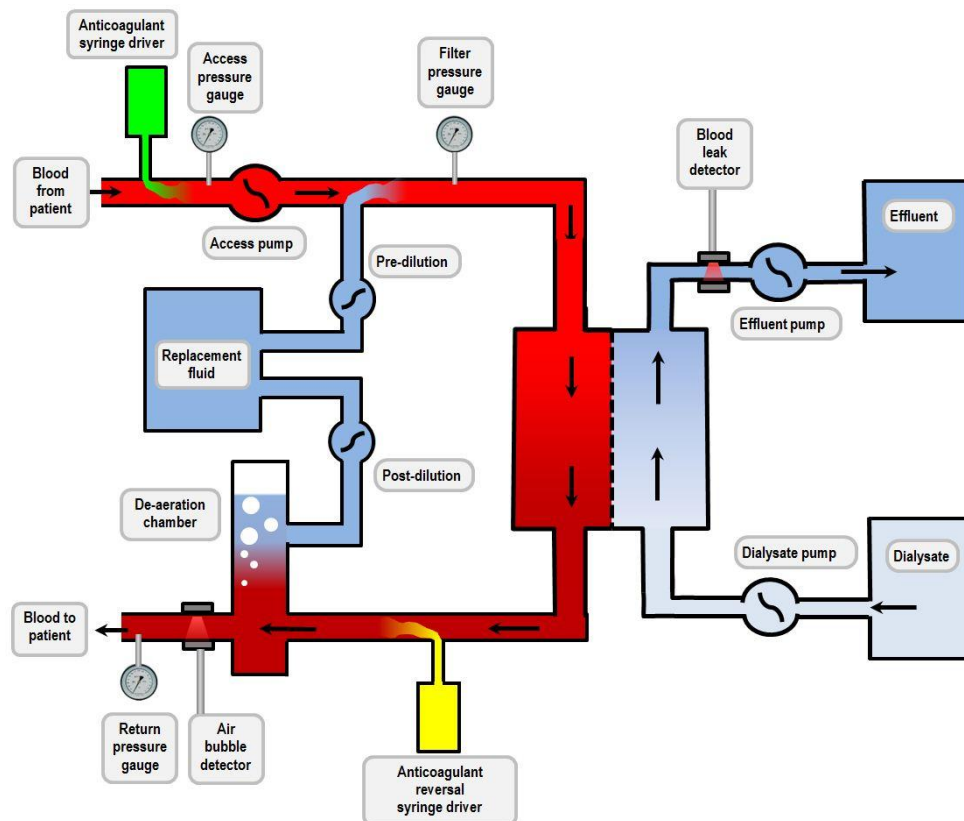
Figure 4.6: The schematic presentation of the extracorporeal circuit for Hemodiafiltration treatment (based on [33]).

4.6   Mass transfer in dialysis

Water and solute removal from the bloodstream with the implementation of an artificial kidney is achieved by three driving forces: 1) Solute diffusion due to a concentration gradient between the two sides of the semipermeable membrane, 2) Water ultrafiltration and solute convection triggered by hydrostatic and osmotic pressure gradients, 3) Water migration as a result of an osmotic gradient.

Dialysis is by its nature a separation process, where one or more solutes "diffuse" across a selective membrane as a result of a concentration difference between the two membrane sides. Yet contemporary dialyzers are designed to combine diffusion with convection, in order to amplify their efficacy in waste disposal.

During a dialysis treatment these two procedures take place simultaneously in the same apparatus, whereas in the natural kidney they occur sequentially in a cascade of glomerular filtration and tubular reabsorption, concluded by the final adjustments in the collecting tubule.

The removal of water and solutes from blood is done by passive transport across semipermeable, polymer capillaries similar to those used in the chemical process call dialysis. Functionally, an artificial kidney (hemodialyzer or simply dialyzer) is a device in which water and solutes are transported from one flow compartment to another. One fluid stream is blood; the other is dialysate: a solution comprises of electrolytes, buffers, and nutrients. The solute concentration as well as the hydrostatic and osmotic pressures of the dialysate are adjusted to achieve transport in the desired direction (e.g., to remove urea and potassium ions while adding glucose or bicarbonate to the bloodstream) [76]. Efficiency of mass transfer is governed by two and only two independent parameters. One, which derives from mass conservation requirements, is the ratio of the flow rates of blood and dialysate [82]. The other is the rate constant for solute transport between the two fluid streams [83]. This rate constant depends upon the overall surface area of membrane available for exchange, its permeability, and such design characteristics as fluid channel geometry, local flow velocities, and boundary layer control, all of which affect the thickness of stationary fluid films, or diffusion barriers, on either side of the membrane.

4.6.1   Filtration & backfiltration affecting hematocrit

So far it was implicitly assumed that differences in concentration across the membrane provide the sole driving force for solute transfer. In clinical hemodialysis, however, the blood phase is usually subject to a higher hydrostatic pressure than the dialysate phase. As a result, water is removed from the plasma by ultrafiltration, dragging with it some of the solutes into the dialysate. Ultrafiltration capability is a necessary consequence of the transmembrane pressure required to keep the blood path open with flat sheet or wide tubular membranes. It is also clinically useful to remove the water accumulated in the patient's body in the interval of dialysis. Ultrafiltration can be enhanced by increasing the resistance to blood flow at the dialyzer outlet, and thereby raising blood compartment pressure, by subjecting the dialysate to a negative pressure or by utilizing membranes more permeable to water than the common cellophanes.

Whenever water is removed from the plasma by ultrafiltration, solutes are simultaneously removed in a concentration equal to or lower than that present in the plasma. For small, rapidly diffusible molecules such as urea, glucose, and the common electrolytes, the rate of solute removal almost keeps pace with Permeability that of water, and ultrafiltrate concentration is the same as that in plasma. With compounds characterized by a larger molecular size, the rate of solute removal lags behind that of water. Indeed with some of the largest molecules of biological interest, ultrafiltration leads to an actual increase in plasma concentration during passage through the artificial kidney.

Backtransport addresses the return of water and solutes from the dialysate back to the bloodstream, as occurs along the capillary membrane of a dialyzer. It comprises the mechanisms of: (1) backdiffusion, a molecular transition along a concentration gradient, and (2) backfiltration, a convective mechanism driven by the local pressure gradient across the membrane [84, 85].

This pressure gradient is defined as transmembrane pressure (TMP) by the following formula:

$$TMP = P_b - (P_d + \pi_b)$$

Where P_b and P_d are the hydrostatic pressures of blood and dialysate respectively, while π_b refers to blood's osmotic pressure. When TMP receives positive values, the hydraulic flow has a direction from blood towards the dialysate side (filtration), whereas negative values designate the occurrence of backfiltration [86].
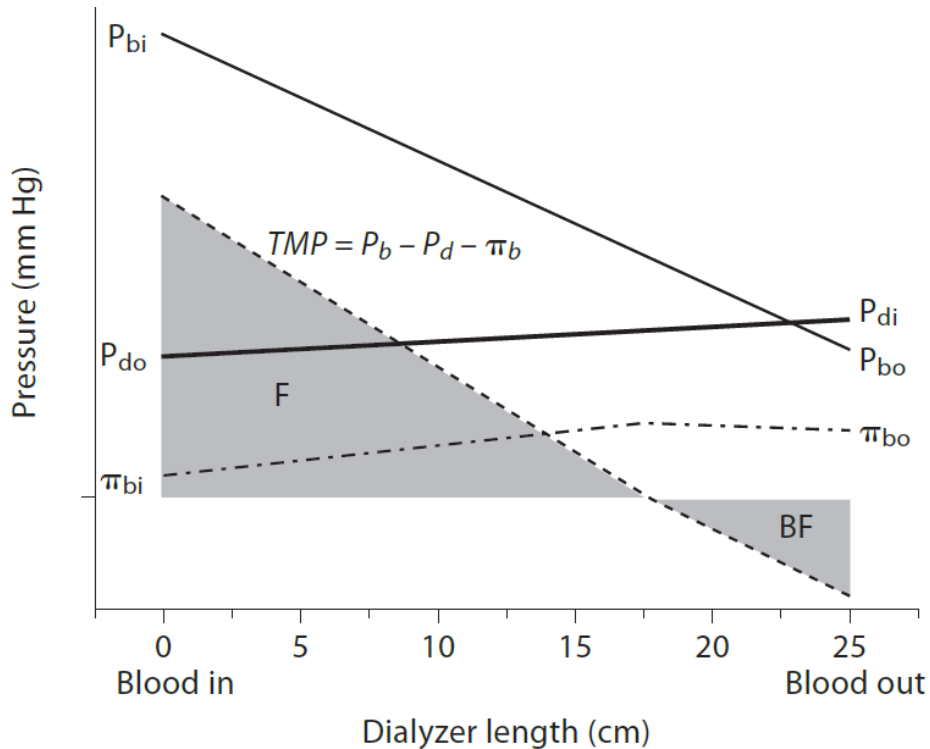
Figure 4.7: Pressure profiles along the dialyzer contributing to filtration (F) and backfiltration (BF). TMP = Transmembrane pressure; P_{bi} = inlet hydrostatic blood pressure; P_{bo} = outlet blood pressure; P_{di} = inlet hydrostatic dialysate pressure; P_{do} = outlet dialysate pressure; π_{bi} = inlet oncotic blood pressure; π_{bo} = outlet oncotic blood pressure (according to[87]).

Filtration will generally increase hematocrit level, but beyond the point of zero TMP, backfiltration reduces hematocrit again to some extent.

Ultrafiltration can be defined as the difference between blood flow entering the dialyzer and blood flow leaving the dialyzer

$$F = Q_{bi} - Q_{bo}$$

The requirement for mass conservation can be revised as

$$Q_{bi}C_{bi} = Q_{bo}C_{bo} + K_b(C_{bi} - C_{di})$$

amount of solute in the incoming blood   amount cleared in dialyzer

amount of solute in the outgoing blood

4.7   Membranes

4.7.1   Membranes materials and morphological structure

Since the first cellulosic dialysis membrane which has been used in 1913 by Abel and Rowntree [67] there were many developments on membrane polymers and membrane geometry. There are three types of membranes currently used in hemodialyzers and hemofilters: cellulose, modified cellulose and synthetics.

Cellulose: It is obtained from processed cotton. Cuprophan® once was the most common type of hemodialyzer membrane until 1990. Cellulosic membranes are also called regenerated cellulose: the membranes are hydrophilic and have low-flux permeability.

Modified cellulose: Cellulose polymer is a straight chain polymer having a large number of free hydroxyl groups on the glucose units. In the cellulose acetate membrane, varying number of these acetate groups are used to substitute OH group. In the modified cellulose (Hemophan®) membrane, some of the surface hydroxyl groups are chemically replaced by a tertiary amino compound.

Synthetic: The synthetic membranes used in hemodialysis therapy are made from different polymers like polyacrylonitrile (PAN), polyamide (PA), polysulfone (PSu) and polymethylmethacrylate (PMMA). The main purpose of developing synthetic membranes was to create more porous membranes which can better simulate the filtration process of the natural kidney thereby removing higher molecular weight uremic toxins so-called such as β2 microglobulin (β2 M) [88].

Dialysis membranes may be either symmetric (almost all cellulosic membranes, PMMA, PAN and AN69ST®) or asymmetric (PA and PSu). Asymmetric structures have a thin inner separation layer on the blood side that essentially determines the sieving properties of the membrane, and at least one support layer that provides mechanical strength in order to withstand TMP. The size and morphology of this support layer varies considerably from membrane to membrane. For high-flux membranes such as PA or polyarylethersulfone, the support layer is characteristically either a figer type or macrovoid structure. Membranes like the Fresenius Polysulfone® have a sponge-like structure, gradually increasing in porosity from blood side to dialysing fluid side.

The polymer chemistry and structure essentially determines the biological and physical behavior of a dialysis membrane. Physical differences also exist between cellulosic and

synthetic membranes. Cellulosic membranes must be made relatively thin (wall thickness of dry fiber in the range of 6.5 to 15 μm) in order to achieve high diffusive solute transport and have a uniform (symmetric) structure of the fiber wall. Such membrane structure cannot sustain the high TMP necessary in convective dialysis treatments such as HF or HDF [88] .

Synthetic membranes are thicker (>20 μm) and may be either symmetric or asymmetric. They permit high water permeability to allow use in hemofiltration. An asymmetric structure implies a thin blood-contacting 'skin' layer (approximately 1 μm) and a support layer that includes the rest of wall thickness. The pore structure of this support layer, which varies considerably among the various synthetic membranes [89, 90] is much more open than the skin layer and has little influence on the trans-membrane solute removal capability. For example, pore diameter of PMMA membrane varying between 2 to 10 nm [91].

A hemodialysis tailored membrane for example, has the smallest pore size on average, because only fine solutes with a maximum molecular weight of 11 kDa should be permitted through (low-flux dialyzers). Hemofiltration, on the other hand, demands a high flux of liquid, hence the membranes suitable for this procedure demonstrate a noticeably higher molecular weight cut-off (ca. 1000 kDA). Hemodiafiltration membranes are similar to those implemented in high-flux dialyzers, which have a MW cut-off of 60 kDA.
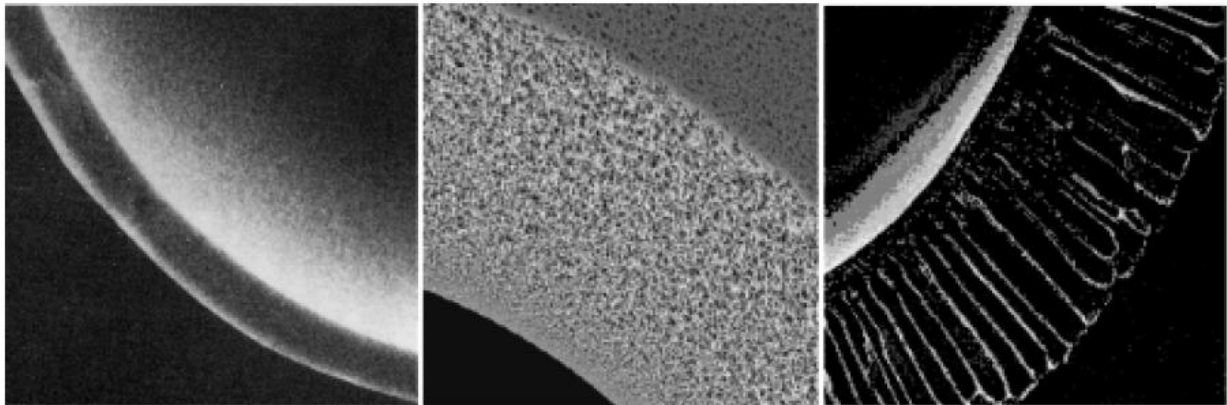
Figure 4.8: Different membrane structure depending on the type of polymer and used for the production (adapted from[88]): Cellulose (left); Polysulfone (middle); polyamide (right).

The surface charge is another important feature of membranes and influences solute transport across the membrane. Zeta potential is used to describe the electrical charge on the membrane. It is the charge that develops at the interface between a solid surface and its liquid medium. The zeta potential indicates the degree of repulsion between adjacent charged particles in its

contacting medium (e.g. blood) and the membrane. Most cellulosic membranes are negatively charged. Synthetic membranes can be also classified according to their negative charge in the order: AN69® (-89 mV) > PAN DX (-85 mV) > SPAN (-70 mV) > PMMA (-25mV) > PSu (-2.5 mV), the others are mostly neutral [92].

4.7.2   Membrane biocompatibility

Biocompatibility has been defined as the ability of a material or device or system to perform without a clinically significant host response [93]. Interactions between blood and the artificial surface of the membrane are the cause of unwanted side-effects during renal replacement therapy. Different biological systems are activated during blood material interaction. Inadequate membrane biocompatibility as well as non-physiological flow pattern stimulate a variety of responses, including activation of the coagulation and complement system, activation of platelets and leukocytes, and production of cytokines and free oxygen radicals [59]. Although they initiate locally, these responses cause systemic changes to the blood and the body behavior. They may also change the surface and transport properties of the membranes used. However, it should be recalled that the treatment of biocompatibility is not solely related to the biomaterials used but rather depends also on the blood fluid dynamics in the membrane device and the whole extracorporeal blood circulation loop, as well as on how blood is handled in extracorporeal circulation[59].

Chapter 5

Rotary blood pumps: experimental studies on red blood cell distribution and trauma at non-uniform shear region devices

5.1   Introduction

Despite the considerable progress accomplished by contemporary artificial organs towards blood trauma minimization, the latter still remains a serious complication in therapies depending on prolonged mechanical circulatory support of internal organs, e.g. ventricular assist devices (VADs), hemodialyzers and oxygenators [2-4]. The destruction of red blood cells, as shown already in 1968, may also occur in the form of sublethal damage, in addition to red blood cells lysis, acting as a limiting factor for long term therapeutic applications [94]. Several investigations have been performed to standardize a defined degree of hemolysis rate for different flow conditions [95-97]. The resulting hemolysis leads to other complications such as promotion of chemical platelet activation, and initiation of the coagulatory response [98]. In order to optimize blood flow inside these devices, improvements have been made in the hemocompatibility of applied biomaterials, and design characteristics. Although this has led to a significant drop in thrombus development in VADs, the reduction of the mechanical destruction of RBCs to an acceptable level, is still facing several challenges [99-102].

Unquestionably, as frequently reported, one of the main causes of hemolysis is the shear stress applied on RBCs [103, 104]. However, the shear stress levels generated by a blood pump or VAD, for a constant rotational speed of the impeller, varies with respect to duration and the exact geometrical location inside the pump [12, 105]. Up to now, most models and simulations of shear stress distribution have been performed under the assumption of a homogenous distribution of RBCs along the pump's geometry [12, 105, 106]. Nonetheless, in the present chapter, it is demonstrated that the possible effect of an inhomogeneous RBCs distribution, caused by shear stress variation and velocity gradient, should be strongly considered. This issue can be corroborated by the fact that RBCs "escape" high shear regions [107], also indicated by the Fahreus Lindqvist effect in the microcirculation rheology [19]. Moreover, Yen and Fung [17] demonstrated that the distribution of RBCs inside bifurcating capillaries is influenced by the velocity ratio in the branches, and they also proved that hematocrit in a vessel with higher flow velocity is respectively higher. Furthermore, several studies presented various quantitative models to investigate inhomogeneous solid particle distributions caused by variations in shear stress [108-110].

Here, a new approach to mimic the flow conditions in a rotary blood pump and their effect on an inhomogeneous distribution of RBCs is reported. An innovative Couette system, equipped with appropriate blades, was designed in order to investigate the relationship between RBCs

distribution and shear stress induced hemolysis. The final objective of this study, in this chapter, is to provide new insights into design modifications for special rotary blood pumps and for other blood contacting devices.

5.2 Theoretical background

An important fluid dynamic aspect of two phase systems is the shear-induced particle migration (11-18). Considering that also for blood in a shear field, as shown on the upper part of Figure 5.1, a "lift force" [108, 111], is exerted on RBCs which is perpendicular to flow direction and towards higher velocity region, i.e. approaching the rotating inner cylinder. This force leads by increasing of shearing time to an accumulation of the cells in the region of higher velocities as reported also in (Evans et al.[112]).
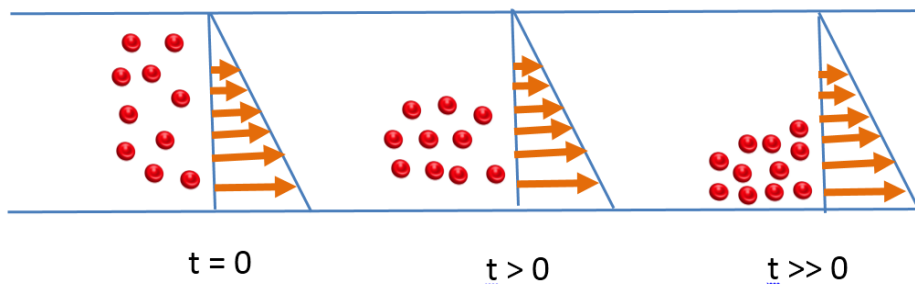
Figure 5.1: Schematic representation of a laminar Couette flow pattern containing RBC shaped particles, realized by two coaxial cylinders (stationary outer - rotating inner): and particle

This regional changes lead to variation of "local" hematocrit values. It is now necessary to evaluate the shear rate which is governing (existing in) this region. Another important issue is the consideration of the resulted shear stress on erythrocytes which is a nonlinear function of shear rate and hematocrit because of non-Newtonian behavior of blood.

Existing reports using the method of computational fluid dynamics (CFD) deal with fluid dynamic behavior of blood flow patterns [12]. According to their CFD results (Behbahani et al. and Taskin et al. [57, 105]) a broad range of shear fields appear in a rotary blood pumps approximately from 500 up to 36,000 s^{-1}[12].

Therefore as it is described in section 6.4, a specific model study seems to be useful to investigate the effect of this large variation of shear regions upon a two phase fluid such as is

the case for blood in order to investigate more specific, the RBC trauma in connection with particularly rotary blood pumps.

5.3   Cell migration hypothesis

In this section, shear induced particle migration will be shortly reviewed and then "cell migration hypothesis in the case of blood as a two phase liquid will be introduced.

The rheological behavior of particle suspensions is a longstanding topic in fluid mechanics, which has attracted great attention since the Segre and Silberberg's [24] report on the inertial migration of non-interacting particles in a Poiseuille flow and Leighton and Acrivos [109] report on the hydrodynamic diffusion of spherical particles in concentrated suspensions. Generally, particle suspensions are considered complex fluids because their rheological behavior exhibit a high dependency on particle size and surface area, concentration, density, elasticity, etc. It is shown that the viscosity of two phase fluids is a function of 1) particles properties: particle radius, density, concentration; 2) suspending medium characteristics: viscosity and density; 3) flow parameters: temperature, shear rate and time.

Small particles in a shear field as shown in Figure 5.2 experience a lift force perpendicular to the direction of flow [109]. The shear lift originates from the inertia effects in the viscous flow around the particle and is fundamentally different from aerodynamic lift force.
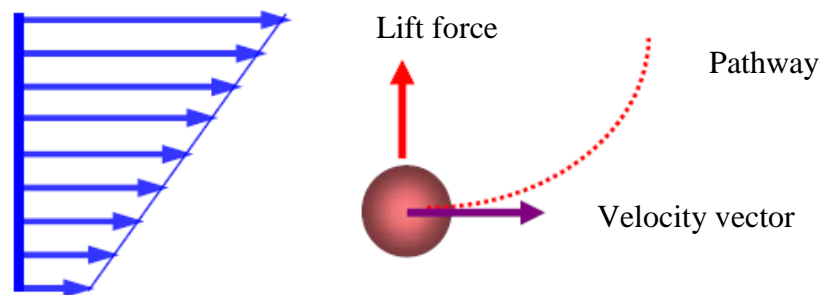
Figure 5.2: Schematic draw of forces exerted to a particle in shear field.

Leighton and Acrivos (1985) obtain the expression for the lift on the spherical particles resting on a plane substrate expressed as [111]:

$$F_{lift} = 0.576\, \rho\, d^4 \dot{\gamma}^2$$

Where ρ is the density of the medium, d is the particle diameter and $\dot{\gamma}$ is shear rate. The force is always pointing away from the wall.

Shearing of fluids having a significant volume fraction of solid particles leads to cross-streamline migration, resulting in higher local concentrations in regions of low shear. In a Poiseuille flow, this drives particles from the walls to the center of the channel. The local increase in viscosity as a result of this migration acts as a feedback mechanism, blunting the velocity profile and increasing the local shear rate near the walls. The final steady profile is achieved when particles are redistributed such that the suspension stresses are once again balanced.

In "Cell Migration Hypothesis", we assumed that in two phase fluid, blood, the red blood cells might behave like particles suspended in plasma. If blood, while passing a special geometry, experience a shear field, a lift force will exert to the red blood cells leading to a migration of the cells in the shear filed and consequently different local hematocrits will appear. The rheology of the blood, under this condition and considering the possible feedback mechanism mentioned above, will be very complicated. Thus, assumption of homogenous distribution of red blood cells would be very far beyond reality. The objective of this chapter is to show how big is the impact of shear induced cell migration on the resulted hemolysis inside a Couette device mimicking a rotary blood pump.

5.4   Couette flow

In this chapter, two different Couette systems were used which enables us to make a very precise and known flow pattern. Therefore, here the Couette system in general is introduced and later in materials and methods, our own modified systems will be described. Couette System (CS) consists of two coaxial cylinders that can rotate at individual rotational speeds around their common axis (Figure 5.3).
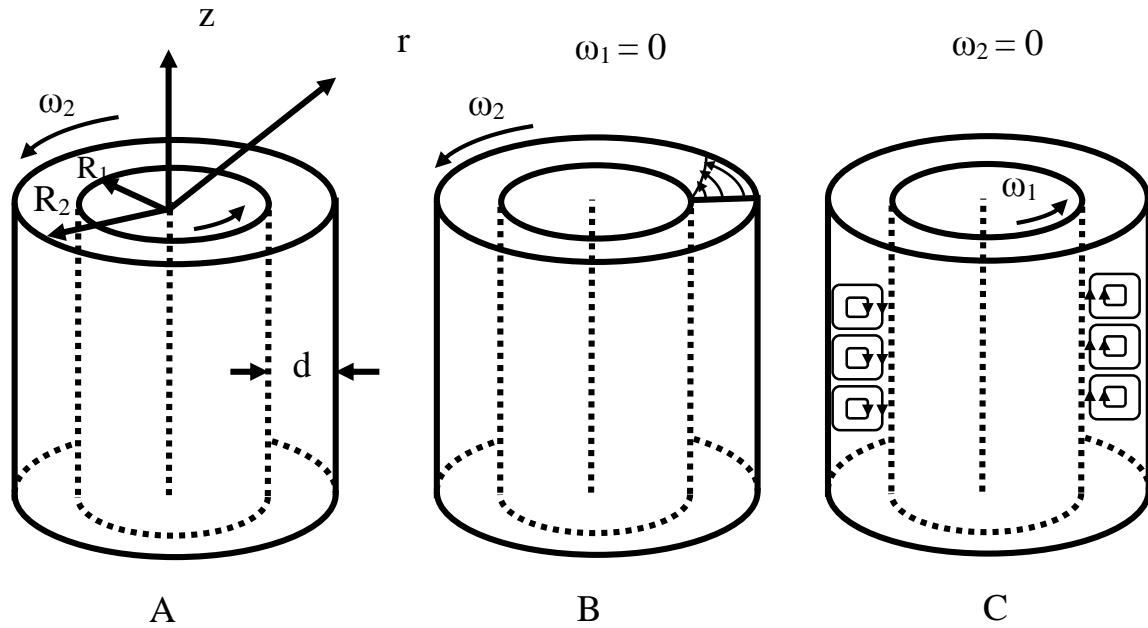
Figure 5.3: Co-axial cylindrical Couette-system: A) counter-rotation cylinders , B) outer cylinder is rotating with a laminar Couette flow characteristic C) inner cylinder is rotating generating aditionalythe Taylor vortices (when Ta> Ta$_{crit,}$).

If the gap size (difference between the radius of inner and outer cylinder is small, Couette-system generates a laminar flow in low rotational speed which imitating the flow between two parallel plates. However, Taylor [113] showed that its especial geometry can lead to a strong influence of the non-linear convective terms in the Navier-Stokes equations. It is translated to a wide variety of flow patterns that can be generated with the Couette system (Figure 5.4). Reynolds number for especial geometry of Couette system at the inner and outer cylinders can be defined as:

$$Re_{in} = \frac{\omega_1 R_1 d}{\nu} \qquad and \qquad Re_{out} = \frac{\omega_2 R_2 d}{\nu}$$

As shown in Figure 5.4, if only the outer cylinder is rotated ($Re_{in} = 0$), only Couette flow pattern will be appeared. However if the inner cylinder or both cylinders are rotated, depends on the Re_{in} and Re_{out}, different laminar or/and turbulence flow patterns might be appeared such as Taylor-vortex, spiral turbulence and featureless turbulence flow. Although most of the flow patterns in Couette system cannot be obtained analytically, but there are two exceptions, the simple Couette flow and the Taylor vortex flow. The latter flow pattern has been described analytically by G.I. Taylor [113]. For other cases, analytical solutions of the Navier-Stokes equations can only be derived under certain simplifying assumptions. If the derivation of an

analytical solution is impossible or too challenging it might more convenient to solve the Navier-Stokes equations numerically.
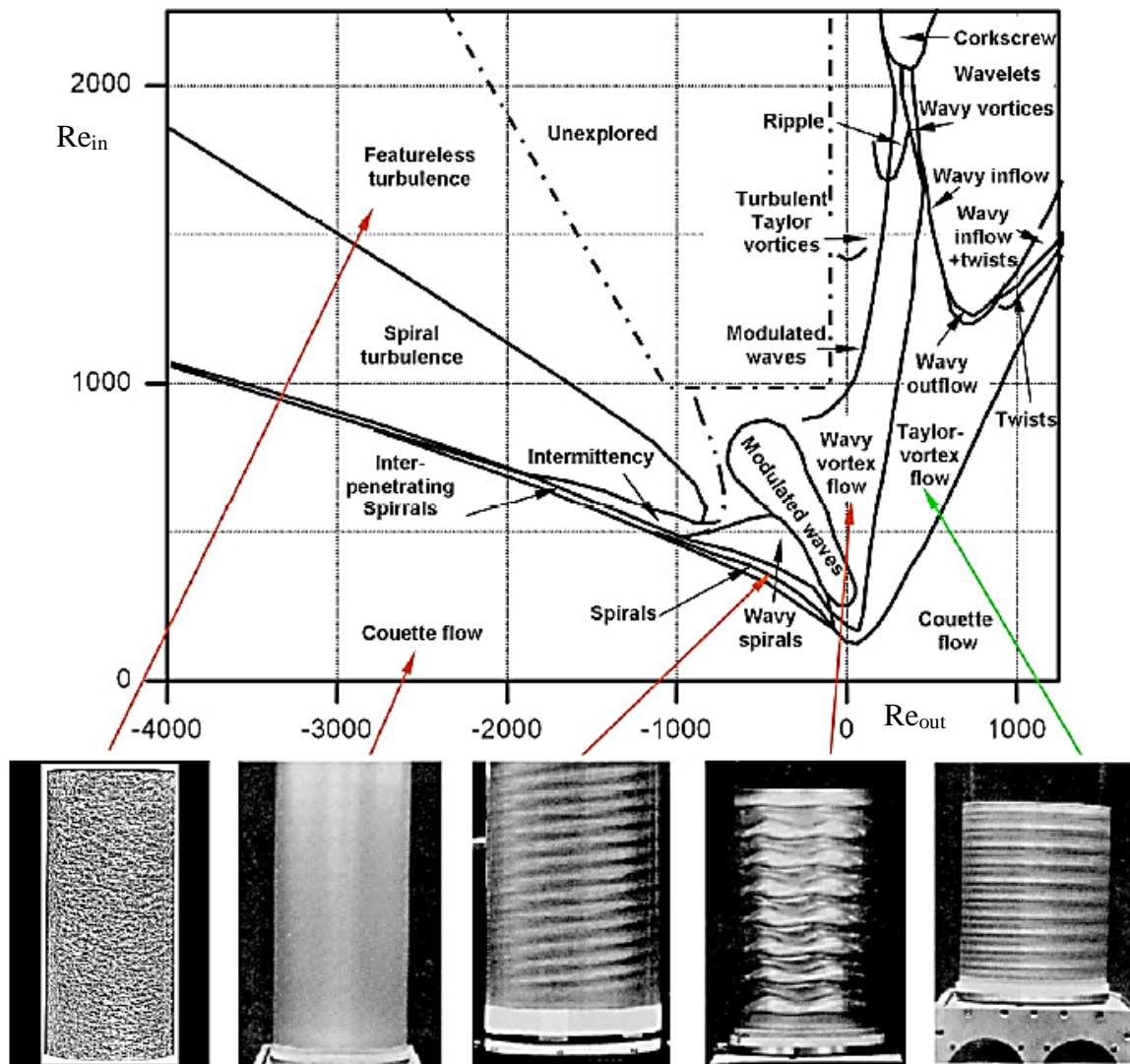
Figure 5.4: Flow patterns observed in the Couette- system generated with different Reynolds numbers for inner and outer cylinder [113-115].

The Taylor vortex flow shows the development of a characteristic flow structure made up of three-dimensional vortices winding around the inner cylinder. They are generating because of the rising inertial forces that push the fluid outwards by increasing rotational speed. These vortices scale with the geometry and their appearance depends on the angular velocity difference between outer and inner cylinder as well as the ratio of their respective radii.

The Taylor number Ta is generally used to characterize Couette systems with fixed outer cylinder and is defined as [31, 115]:

$$Ta = \frac{\omega_1 R_1}{\nu R_2} ((R_2 - R_1)^3 \frac{R_1 + R_2}{2})^{0.5} \qquad \text{(Eq. 5.4.1)}$$

Where R_1 and R_2 are radius of inner and outer cylinder, d is the gap size, ω is rotational speed of inner cylinder and ν is kinematic viscosity. The square of the Taylor number Ta^2 indicates the ratio of the centrifugal force to the viscous force. At a critical value of $Ta^2_{critical} = 1708$ (that is Ta = 41.3), it is observed that the circular Couette flow changes into the Taylor vortex flow with steady and rotationally symmetric perturbations, so called Taylor vortices. As already mentioned, Taylor vortices are appearing only when the inner cylinder is rotated and generating a Taylor number greater than critical value or for some specific Reynolds numbers when both are rotated. It is realized that only by rotation of the outer cylinder, Taylor vortices will never appear.

5.5   Materials and methods

5.5.1   Developing a couette flow model

A Couette flow system was designed in order to experimentally simulate two different types of flow situations. The basic shape of a Couette flow system consists of two coaxial cylinders (inner cylinder radius r_1=34 mm and outer cylinder radius r_2= 35 mm) realizing laminar Taylor-Couette flow when the inner cylinder rotating. The inner cylinder can rotate at different speeds while the outer cylinder is stationary. A second version of the system was created by modifying the basic geometry as shown in Figure 5.5.A: a thin blade with a width of 1mm and a length of 0.8 mm was mounted on the inner cylinder, thus generating a smaller gap (0.2 mm instead of 1mm) between the tip of the blade and the outer cylinder housing.

The mean shear rate $\dot{\gamma}$ can be calculated as [115-117]:

$$\dot{\gamma} = \frac{2R_1{}^2 \omega_1}{R_2{}^2 - R_1{}^2} \qquad \text{(Eq. 5.5.1)}$$

Where $\omega_1 = 2\pi n_1$ and n is rotational speed.

A

B
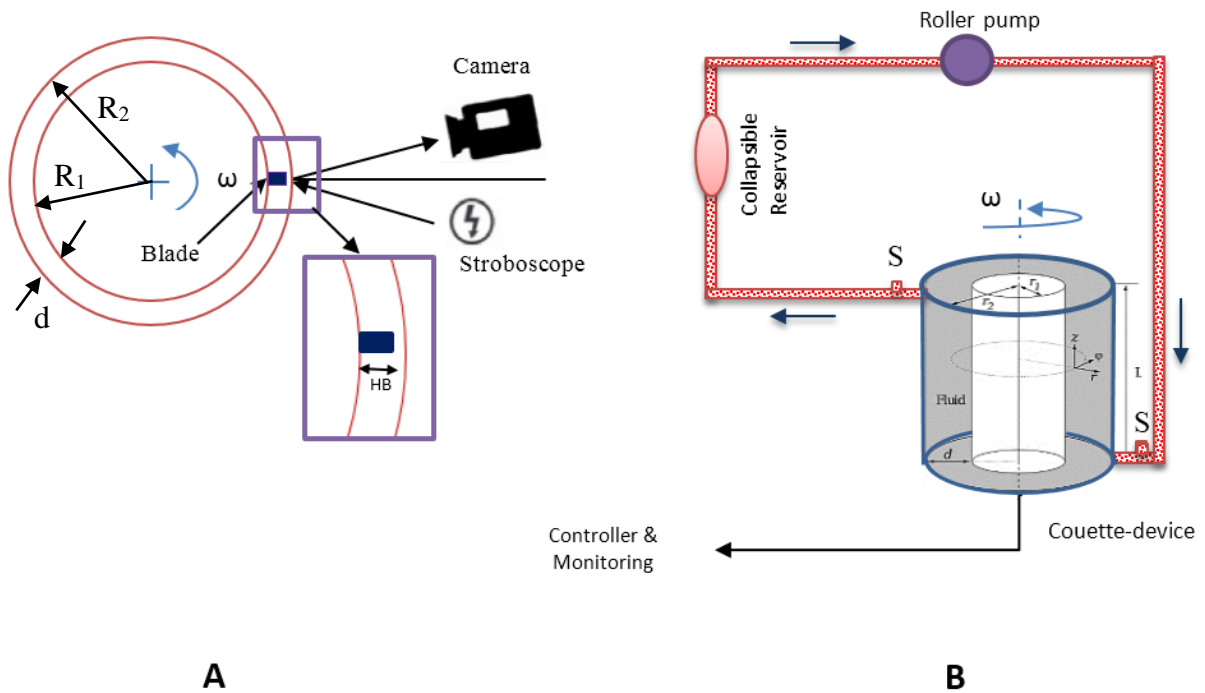
Figure 5.5: Cross section of the Couette device along with the visualization arrangement (A), and schematic representation of the circulating system configuration (B)(see text).
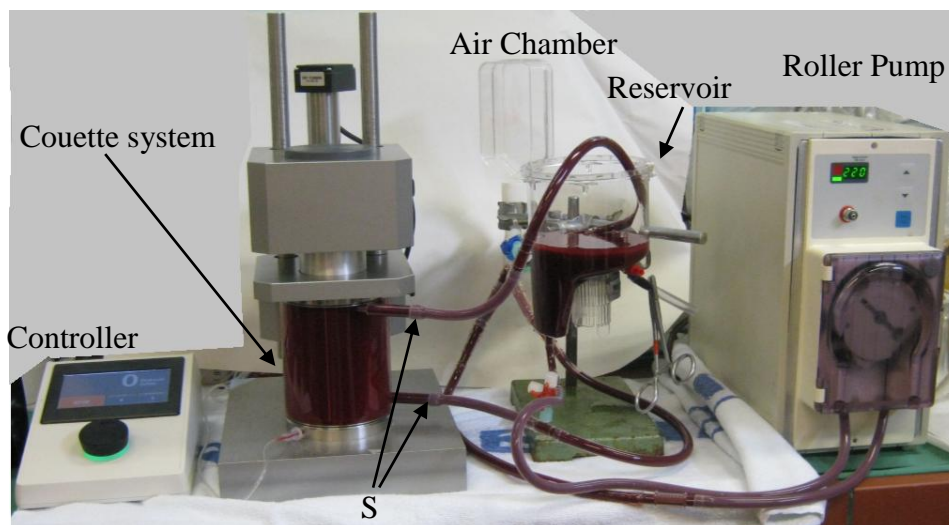
Figure 5.6: Photograph of the actual experimental setup illustrated schematically in Figure 5.5 for recirculating system.

5.5.2   Circulation circuit

A recirculation circuit with a priming volume of 500 ml as shown in Figure 5.5.B was developed in order to set the desired shear field exposure time by pumping velocity. Fresh

porcine blood from a local slaughterhouse was obtained and anticoagulated with 5000 UI heparin per liter blood. Different hematocrit values were prepared by hemo-concentration or -dilution using native plasma.

The priming volume of the Couette device i.e. gap volume is 22 ml while the total priming volume increases to 500 ml, when the apparatus is incorporated in a recirculating loop (clamps open position, Figure 5.5.B). Shear exposure time in the circulating system depends directly on the axial blood flow velocity which is adjusted by means of a calibrated roller pump. The blood flow rate, Q_b, varies up to 300 ml/min, and a small collapsible reservoir, which dampens the pump pulsations and compensates for the fluctuations produced by drawing blood from sample ports (S) is integrated into the circuit. A combined stroboscope and camera system was employed for visualizing the RBCs distribution (Figure 5.5.A). The rotational speed of the inner cylinder and the pulse frequency of the stroboscope were synchronized to take photographs of the blade at a defined position.

5.5.3   Evaluation of hemolysis

The resulting hemolysis was quantified by using a spectrophotometer to measure the absorbance of light at wavelengths of 540 and 680 nm in mg per dl (Pharmacia Biotech, Cambridge, England). For the non-recirculating Couette system, the amount of hemolysis was evaluated as a dimensionless damage index which is defined by the following formula [97]:

$$DI = \frac{fPHb_{native\ blood} - fPHb_{sheared\ blood}}{Hb_{concentration}} \qquad \text{(Eq. 5.5.2)}$$

 In the experiments with the circulating system a normalized index of hemolysis (NIH) is usually applied according to Equation 5.5.3 [95, 96]:

$$N.I.H. = \frac{\Delta C_{Hb}.V.(1 - Hct)}{\dot{Q}_b.t} \qquad \text{(Eq. 5.5.3)}$$

where Q_b is the blood flow rate, V the total priming volume and t the shearing time. However in this chapter, for recirculating system, to have a more straightforward comparison with the data of non-recirculating Couette system, the Equation 5.5.2 is also used.

5.6   Results

The following results show the data for generated hemolysis performed in the non-recirculating Couette system with and without integrated blade. The shear rate in the non-recirculating

Couette system without blade at a rotational speed of 300 rpm is calculated to be equal to 1100 s^{-1}. However, the same system with a blade can generate a shear rate of 5300 s^{-1} in the gap between the blade tip and outer cylinder. Figure 5.7 shows a comparison of the resulting DI for both cases.
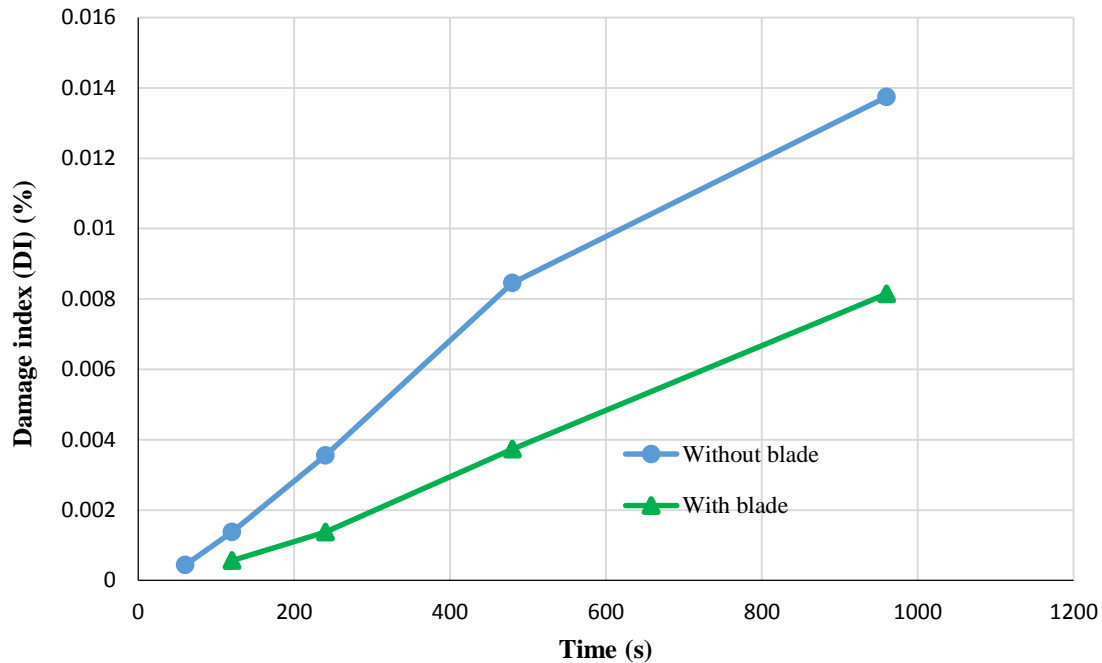
Figure 5.7: Enhancement of damage index (DI) (whole blood, Hct = 0.36) over time with the established shear rates at constant rotational speed of 300 RPM in the Couette device with and without blade.

It is shown that at the lower shear rate level of 1100 s^{-1}, produced by the blade-free Couette system, has resulting hemolysis values which are higher in comparison to those measured in the presence of the blade, which locally generates a much higher shear rate of 5300 s^{-1} in the narrow gap region.

In fact, the homogenous distribution of RBCs is disturbed in the system with the blade.

This phenomenon can be visually investigated using the combination of a stroboscope and a camera, having photographs of the blade tip taken every 15 (s) as shown in Figure 5.8.

Two sets of experiments were performed at shear rates of 8900 and 10700 s^{-1}. Figure 5.8 shows the stroboscopic pictures at 30 s and after 5 minutes of shearing for both shear rates. Other visualization attempts will be explained in section 5.6.
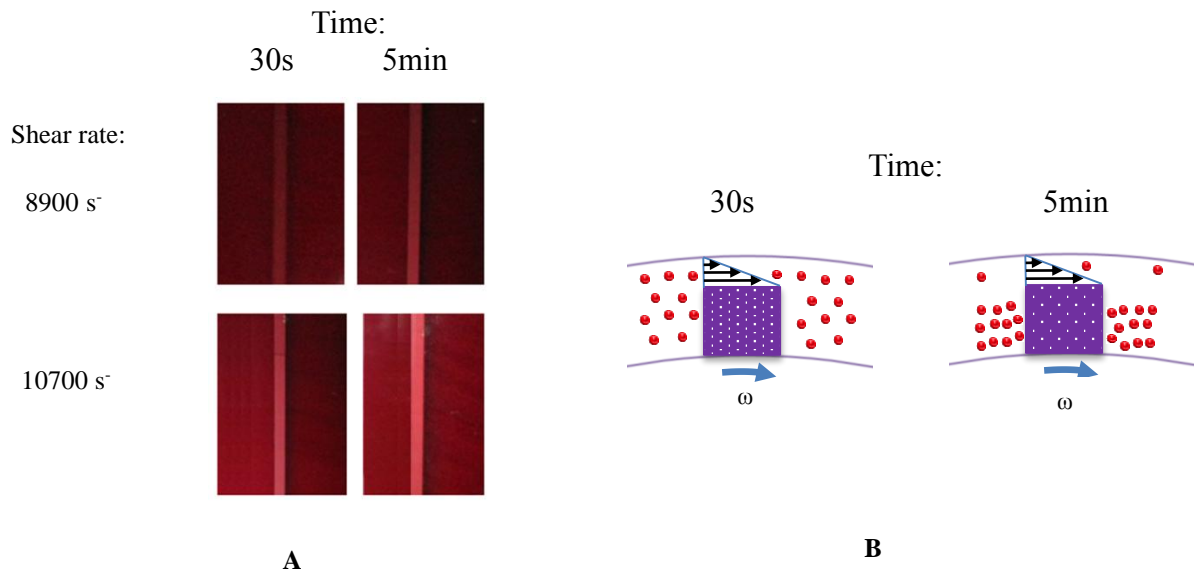
Figure 5.8: Stroboscopic photographs of the Couette device at two different time sequences, and for two distinct shear rates, in the presence of the blade. Note that the lighter color strip in the range of the blade tip surface area indicates a decrease in RBCs concentration (A). A graphic

In the figure above, it is clearly visible that with increasing shearing time the space between the blade tip and the outer cylinder is becoming lighter in color tone, for each individual shear rate.

In order to investigate the possible effect of a non-homogenous distribution of RBCs, i.e. local hematocrit variation, a set of experiments were subsequently performed. Different blood volumes were prepared, with a range of hematocrit values between 0.10 and 0.70. In the first series, the samples were exposed to increased shear rates, up to 3600 s^{-1}, whereas in the second series were sheared at a constant shear rate, with different periods, up to 16 minutes. The results for both experimental arrangements, i.e. with and without blade, are depicted in Figure 5.9 and Figure 5.10.
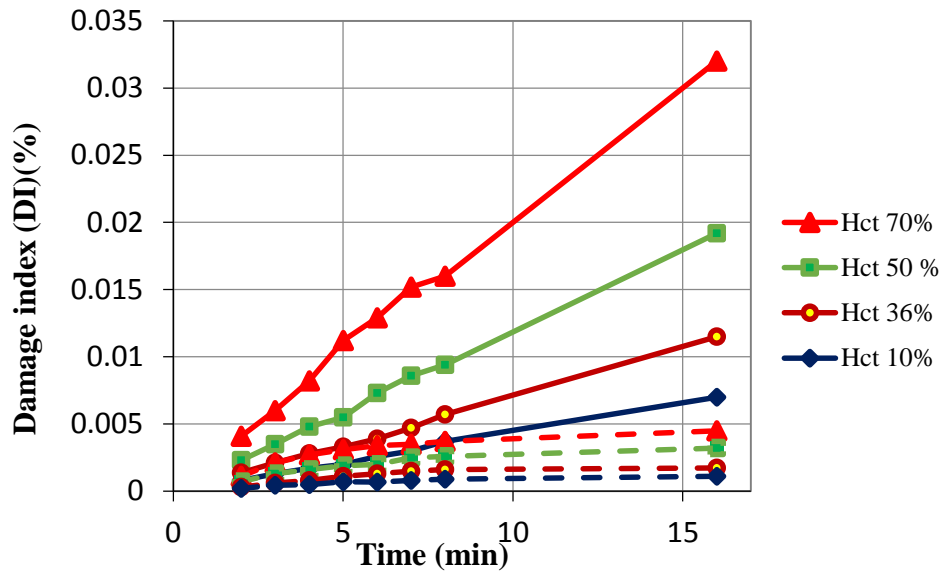
Figure 5.9: Solid lines: normal Couette gap. Dashed lines: Couette gap with inserted blade.
Damage Index (DI) by increasing of shear time for hematocrit values from 10 to 70 %.at a
shear rate of 1100 s^{-1}.

As it becomes apparent in Figure 5.9, the values of DI generally drop with decreasing hematocrit values, for constant shear rate of 1100 s^{-1}. Although in the definition of DI, the effect of hemoglobin concentration variation is standardized (Equation 5.5.2), it is nevertheless interesting to observe that here its values are higher for increased hematocrit values in both arrangements, with and without blade, as it will be discussed further below.
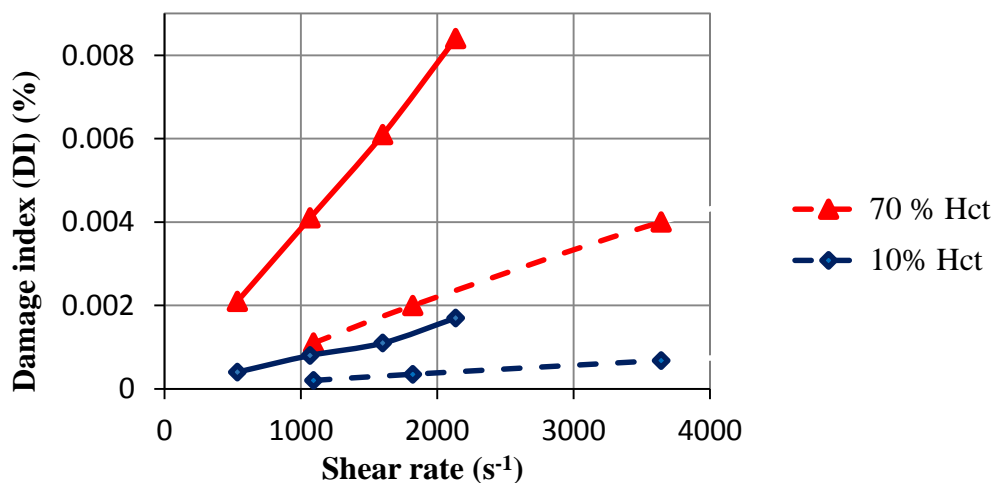
Figure 5.10: Solid lines: normal Couette gap. Dashed lines: Couette gap with inserted blade.
Damage Index (DI) by increasing of shear rate for hematocrit values of 10 and 70 % at a
constant shearing time of 120 s.

In order to adapt the system to the clinical applications of rotary blood pumps, the blood was recirculated in the loop as shown in Figure 5.5.B for the circulating system configuration. The results are depicted in the following figure (Figure 5.11). It demonstrates again a lower hemolysis level in the presence of the blade, in comparison to the blade-free arrangement, for the same rotational speed of 300 RPM.
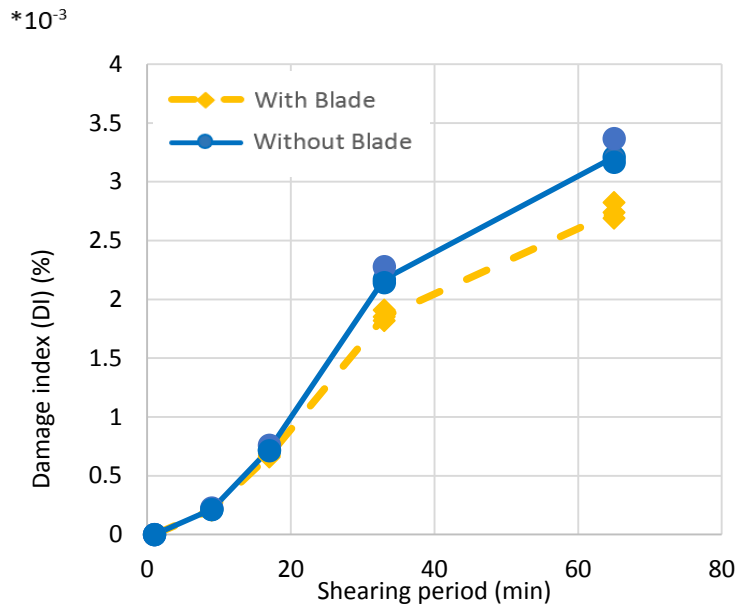
Figure 5.11: Damage index of hemolysis (DI) versus shearing time in the circulating system, with, and without blade for the same rotational speed of 300 RPM.

As already said, it is typical to calculate and consider the NIH for recirculating system, however, in the Figure 5.11, DI is shown. It allows us to have a simpler comparison with the presented data in previous chapters. Nonetheless, the results are reported as normalized index of hemolysis in Figure 5.12. The significant difference between NIH values for the cases with and without blade is clearly can be seen in this graph. Based on the definition of NIH which is reported as the change in plasma free hemoglobin over time, the values for a very long time becomes smaller. That is why the values at 65 minutes decreasing. However, even in this case, the trend of lower values in the presence of the blade can be seen explicitly.
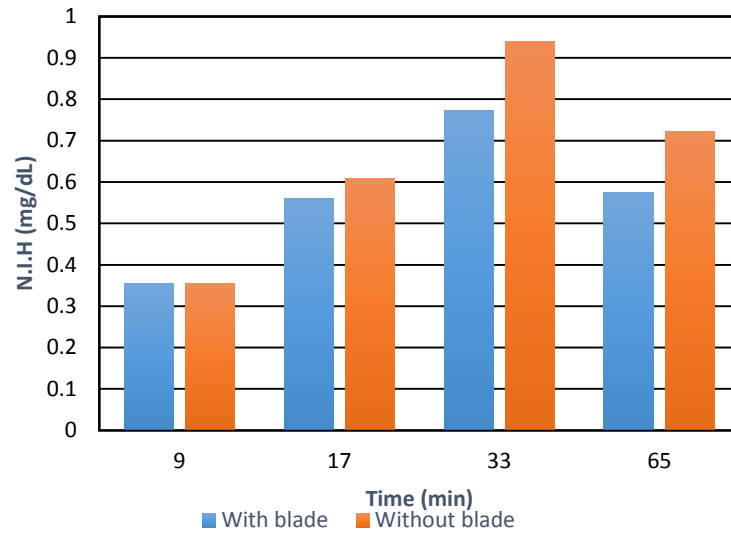
Figure 5.12: Normalized Index of Hemolysis (NIH) versus shearing time in the circulating system, with, and without blade for the same rotational speed of 300 RPM.

5.7 Visualization studies

5.7.1 Blood

In fact, in the system with blade the homogenous distribution of RBCs is disturbed. This phenomenon can be visually inspected using the combination of a stroboscope and a camera, with photographs taken every 15 s from the blade tip side as shown in Figure 5.5.A. Two sets of experiments were performed at shear rates of 8900 and 10700 s^{-1}. Figure 5.8 shows the stroboscopic pictures at 30 s and 5 minutes shearing for both shear rates. In that figure as well as Figure 5.13, it is clearly visible that with increasing shearing time the space in between the blade tip and outer cylinder is getting lighter in each individual shear rate.
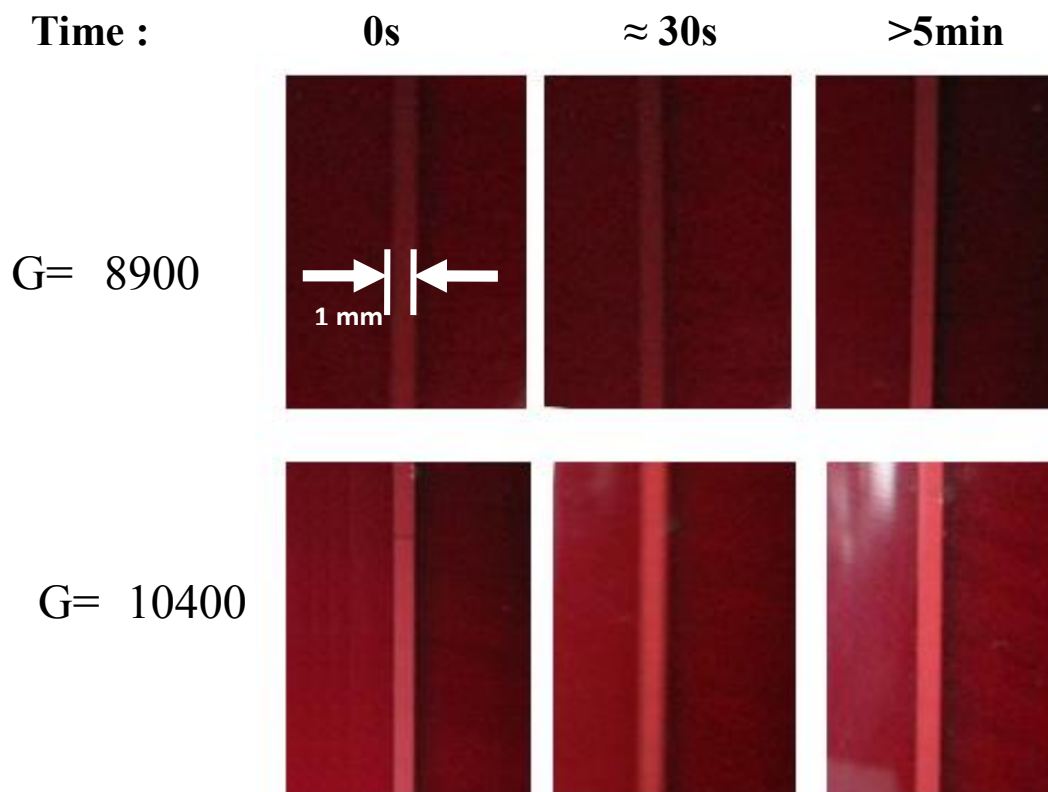
Figure 5.13: Visualization of the hypothesis of shear induced particle migration using porcine blood.

5.7.2   Particles Descurainia Sophia (Khakshir) with D < 200µm

Another visualization experiment were conducted using an aqueous suspension of some non-water soluble particles called Khakshir. The average particle size was less than 100 µm and therefore they could easily pass through the gap. In this configuration, the gap size was 3mm (radius of inner cylinder= 30 mm,radius of outer cylinder= 20 mm and the height of blade= 7 mm) which is in the same ratio in comparison to the modified Couette system with blade.

Figure5.14 : Visualization of the hypothesis of shear induced particle migration using "Khakshir" particles in water.

The main advantage of this method was that it is possible to count the particle and visually realizing the concentration difference.

In the Figure 5.14, it is clearly shown, that particles concentration decreases drastically in the space between the tip of the blade and the outer cylinder.

5.7.3 Fine particles (emulsion of dyed soap particles in fluorocarbon (FC-43))

Similarly, the hypothesis of the migration of particles towards low shear regions is evidenced using an emulsion of Fluorocarbon (FC-43) and colored soap particles (Figure 5.15). Fluorocarbon (FC-43) is FC-43 is a clear, colorless, fully-fluorinated liquid. Like other Fluorinert electronic liquids, Fluorinert liquid FC-43 is thermally and chemically stable, compatible with sensitive materials such as biologic materials and even blood, nonflammable, practically nontoxic and leaves essentially no residue upon evaporation. This unique combination of properties makes Fluorinert liquid FC-43 ideal for many research applications. The possibility to make uniform emulsion with aqueous solutions was the main reason to select it as continues phase for this visualization.
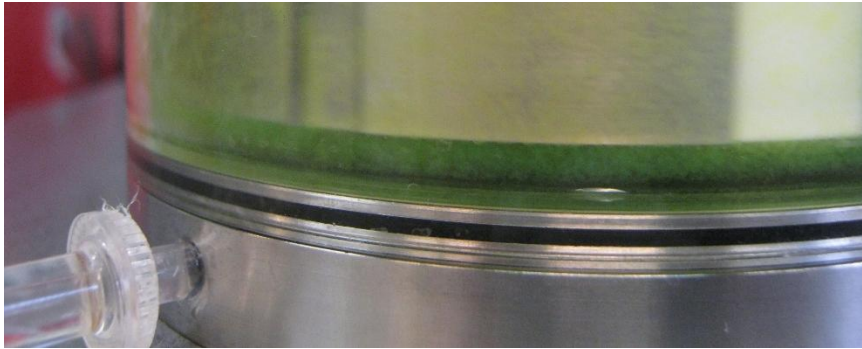
Figure 5.15: Axial migration to low shear region below the inner cylinder, note the higher concentration of green soap particles suspended in fluorocarbon (FC-43).

5.8   Discussion

Shear induced hemolysis in blood contacting devices has been investigated since the initiation of their clinical applications. However, the regional distribution of RBCs inside such devices has not been yet systematically investigated. In other words, the local hematocrit value is not considered in the total outcome of the resulting hemolysis. In spite of that, different shear regions, e.g. inside different parts of rotary blood pumps, have already been discussed and reported [12, 105]. The presently introduced Couette device with the possibility of inserting fixed blades, as already shown in Figure 5.5, renders the existence of different shear regions as an experimental model, mimicking the shear variations inside such devices.

Figure 5.7 demonstrates, as a matter of fact, that DI intensifies with increased shearing time, however, interestingly it is observed that the higher hemolysis values were produced in the blade-free configuration with a lower shear value. This phenomenon directly contradicts the general expectation that higher shear rates intensify hemolysis, as it is also used in models for hemolysis estimation [103, 118, 119]. The major cause of this phenomenon lies in the variation of red cells distribution inside the different shear regions.

This hypothesis is corroborated by other experiments and is presented in Figure 5.8. It can be concluded that there is a reduced local hematocrit value between the blade tip and the outer cylinder, which increases with prolonged shear exposure time. A similar phenomenon was reported by Evans et al [112] during investigations with suspended solid particles. This time-dependent effect obviously occurs due to the migration of red cells towards the reduced velocity gradients, near the inner cylinder; and consequently leads to a hemoconcentration close to the rotating inner cylinder (Figure 5.8.B).

Figure 5.9, as mentioned in the results, demonstrates significantly increased DI values for higher hematocrit levels. This increase is particularly emphasized in the case of the blade-free configuration (Figure 5.9.A). However, for higher hematocrit values, e.g. over 10%, it is obvious that DI-increase is almost linear in the blade-free configuration, in contrast to the configuration with the blade, which exhibits asymptotic behavior. It is assumed that these different behaviors are the result of the shearing time, causing the proposed migration of the cells to the lower shear regions, i.e. closer to the inner cylinder, in Figure 5.8. In general though, the generated hemolysis is lower in the presence of the blade than in the blade-free Couette configuration.

The relationship between the generated hemolysis and shear rate at different hematocrit values has been presented in Figure 5.9.B. In this context, the relationship between the shear stress and shear rate is an important topic that needs to be acknowledged. Figure 5.16 shows the non-linear impact of increasing hematocrit on the resulting shear stress values for different shear rate levels. According to Equation 5.5.2, Damage Index is independent of the hemoglobin concentration in blood plasma. However, the impact of hematocrit on hemolysis within each of the investigated shear stress regimes should be considered. Therefore, it is interesting to note as an example of the disproportionate increase in shear stress that the DI value for a hematocrit of 70 % is four times higher than that for 10% at a shear rate of 1000 s-1 (Figure 5.9.B).

Cell migration to the lower shear regions occurs also in the circulating system as demonstrated in Figure 5.11. In general, NIH values are slightly lower in the Couette device where the blade is present, in comparison to those of the blade-free Couette device at a constant rotational speed of 300 RPM.

In this configuration the total priming volume of the circulation system amounts to 500 ml, which includes the gap volume in the Couette device (22 ml). The same tendency is observed in this case as well, as RBCs recirculate in the gap of the device, i.e. less DI values in the presence of the blade. It confirms once again the hypothesis of RBC migration to the lower shear regions.
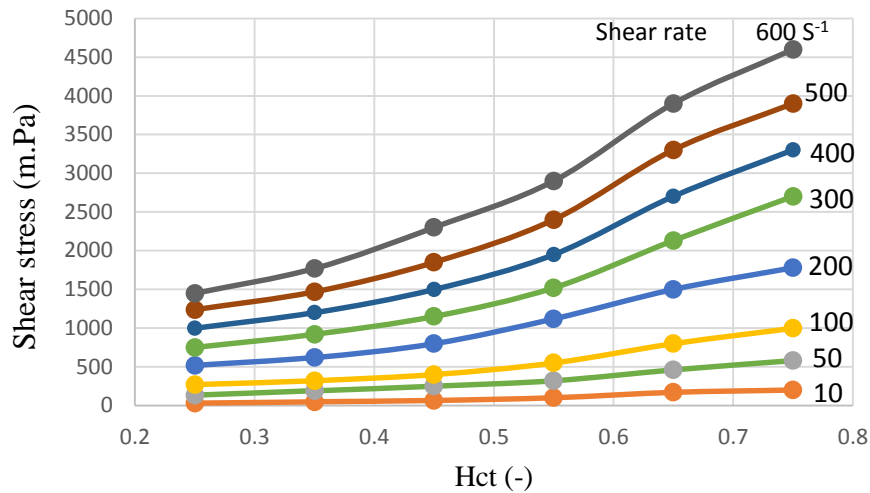
Figure 5.16: Significant increase of shear stress by elevation of hematocrit value at different shear rates based on literature data for human blood [31, 40].

Consequently introduction of a single threshold or as often reported critical shear stress will not represent the total performance of this kind of pumps rather than a mean value of the sum of a total effect of different established shear rates at different part of the pump. This is in accordance to so called shear stress history and "damage accumulation" introduced by Yeleswarupa et al [120].

Yeleswarupa et al showed that the hemoglobin released in the old population of the old cells exceeds dramatically that in the young population. The values for whole (mixed) blood is statistically in between in regard to proportion of old and young cells. Therefore hemolytic effect of shear stress is varying by the age of the red blood cells (30).

They proposed a damage index that records the accumulated damage due to time dependent shear stress i.e. damage history experienced by cells.

Lee et al (31) reported about a long-term intermittent cyclic system in which the blood was recirculated in alternatingly higher and lower shear regions. They compared the cumulative effect of cyclic shearing exposure upon stiffness of RBC membrane to a continuous shear flow (Couette). They observed that the cyclic shear stress irreversibly stiffened the cell membrane however less than as in continuous shearing Couette device. Above mentioned report elucidates the need for improved modelling systems to predict cellular trauma within the unsteady flow environment of mechanical circulatory assist devices. In fact, the red blood cells in rotary blood

pumps experience a wide range of cyclical shear stress which is highly non-uniform and changing swiftly.

As shown in figure 5.4., Taylor vortices are appearing by exceeding the Taylor critical value only when the inner cylinder is rotated or for some specific Reynolds numbers when both are rotated. This vortices never appear by only rotation of the outer cylinder. In the case of modified Couette flow device including a blade representing the impeller of rotary blood pumps which was used as the main test case, it is worth mentioning that the blade disturbs the flow pattern and does not allow the vortices to be produced. It is postulated that a laminar flow pattern is generated between the tip of the blade and outer cylinder with a high shear rate while a bulk flow produced in front of the blade possessing a low shear rate. It was also visually confirmed that in the case of modified Couette flow device, no vortices can be observed. In fact, all other flow patterns mentioned in figure 5.4 such as spiral and featureless turbulence, Couette flow, Taylor vortices, turbulent Taylor vortices, wavy vortex flow, wavy spiral and etc. can be produced only in the case of Couette flow device with no flow disturbance (blade).

5.9   Conclusion

The effect of the distribution of RBCs on shear induced hemolysis has not been yet systematically investigated. In this chapter, the impact of RBC migration between high and low shear regions is demonstrated, after reliable evaluation of the resulting hemolysis, using an innovatively designed Couette device. The insertion of a blade in the gap between the two coaxial cylinders, along with the recirculation of blood through the device, mimics in a realistic way the critical phenomena causing blood trauma inside the rotary blood pumps. The stroboscopic visualization of the narrow gap that the blade establishes in the Couette device, reveals that local hematocrit values are time dependent and have a depreciative tendency. This redistribution of RBCs is the reason for the appearance and the establishment of local hematocrit values. Therefore as suggested here, in order to reduce hemolysis, the significant role of local hematocrit values should be taken into consideration in the future design improvement of blood contacting devices to provide optimal hemocompatibility.

Chapter 6

New modified semi empirical model for red blood cell trauma

6.1   Introduction

Design Optimization of blood contacting artificial organs depends on several criteria; among them, hemocompatibility and minimizing the blood trauma is still one on the main current challenges [3]. Blood trauma, itself is a general issue including various undesirable phenomena e.g. platelet activation and hemolysis. Hemolysis refers to release of intracellular content of RBCs into the surrounding plasma. RBC membrane breakdown is known as the common hemolysis mechanism [121]. Nevertheless, the permeation of hemoglobin through unruptured cell membrane also can lead to increase of free plasma hemoglobin (fPHb) level which is the marker of hemolysis. This subject is known as sub-lethal hemolysis.

Several datasets of hemolysis measurements are reported in the literature, yet in this chapters, the Wurzinger data, the 2D regression of which, implemented by Giersiepen [119], are often the primary reference in numerical assessments of blood damage, stating as hemolysis index (HI) are used.

$$HI = a_1 \, t^{a_2} \tau^{a_3}$$

Notwithstanding the widely acknowledged fact of overestimated blood damage [103] generated by an overheating seal during Wurzinger's experiments [103, 122], the power law equation introduced by Giersiepen is still widely used. This is justified by the fact that the equation's power constants, reproducing the cellular membrane's mechanical properties, are roughly precise, and the single one in need of revising is coefficient A, the overestimated one [104]. Approaching the problem from a statistical viewpoint, as Goubergrits et al. demonstrated in [104], can prove positively beneficial. This method involves Giersiepen equations and their adaptation to the lifespan of human blood cells (120 days for erythrocytes on average). The result of this approach is the modification of coefficient a_1 by a factor of 0.0416 ($a_{1_{corrected}} = a_1/24$), which in turn mitigates/moderates the exaggerated blood damage encountered in Wurzinger's experiments. Despite the confirmed disagreement and the criticism they have undergone, Wurzinger data reproduce a rational pattern, and therefore can still be used and referred to [122].

Prediction of RBC damage, caused by different types of mechanical stress in blood contacting components is an important factor during the process of modeling and designing such devices. The current and conventional approaches employed for modeling shear-induced blood damage are respectively based on continuous models, i.e. stress and strain based models [119], and threshold models, which is also known as the "all or nothing" blood damage models [123].

Both of these methods are established on empirical correlations that do not take entirely into consideration all the physical phenomena involving in blood trauma.

To overcome the limitations of the aforementioned empirical models, Vitale et al. proposed two alternative approaches based on "physical" interpretations of this subject namely the Permeability or sub-lethal (SUB) and the Non-uniform Threshold (NUT) models[4]. These two models were formulated by considering hemoglobin penetration through cell membrane and hemoglobin release after cell membrane breakdown. However, the modest agreement of their results with experimental data remains a substantial disadvantage. Moreover, each of these models is applicable in a limited range of shear stress[4].

In this chapter, a new semi-empirical model based on our experimental data obtained by in-vitro blood studies is introduce. Our proposed model also shows a good agreement with experimental data published in other literatures. In addition, blood damage through a wide range of shear stress, i.e. up to 610 Pa, can be accurately predicted using this novel approach.

In the present chapter, the Wurzinger dataset were used for human blood. However, since the currently proposed model sufficiently correlates with this dataset by considering the aforementioned amended factor introduced by Goubergrits et al., it can be safely assumed that it can also be applied to other datasets with minor modifications (recalculation of the parameters' optimal values).

6.1.1   Theoretical background

Free plasma hemoglobin (fPHb) in NUT model is assumed to be released through the ruptured cell membranes of RBCs. In this model, according to the evidences presented by Yeleswarapu et al.[120], cellular resistance to shear stress varies between different RBCs and corresponds to their age's distribution. Therefore, a rupturing threshold time exposing to shear stress, t_{th}, can be defined for each individual RBC based on its age. The fraction of burst RBCs at time t, η, can be defined as following [4]:

$$\eta\,(t,\tau) = \int_0^t PDF\,(t,\tau;\bar{t},\delta^2)dt_{th} \qquad\qquad \text{(Eq. 6.1.1)}$$

Where PDF is a gamma probability density function of t and τ with two constant parameters of $\bar{t}$ and δ^2. $\bar{t}$ is, itself the average membrane breakdown time of RBCs and δ^2 is the variance

of $PDF(t_{th}|\tau)$. RBCs' Damage Index (DI) is basically determined by the following equation[97]:

$$DI = \frac{\Delta C_{Hb,Pl}}{C_{Hb,WB}}$$ (Eq. 6.1.2)

Where $\Delta C_{Hb,Pl}$ is the difference of fPHb before and after shearing and $C_{Hb,WB}$ is hemoglobin concentration of whole blood. By substituting and simplifying the relevant equations, DI in a NUT model can be formulated accordingly:

$$DI_{NUT}(t,\tau;\bar{t},\delta^2) = \frac{\eta\,(t,\tau)}{1-Hct_i\,(1-\eta\,(t,\tau))}$$ (Eq. 6.1.3)

Where Hct_i is the initial value of hematocrit. The values of δ^2 and $\bar{t}$ are calculated by using curve fitting on the literature dataset published by Heuser and Opitz [124].

Unlike the NUT model, SUB model assumes that the permeation of fPHb through unruptured RBCs membrane, while the cells exposed to shear stress. Based on Fick's law, the transmembrane flux of hemoglobin, J_{Hb}, is defined as a function of concentration difference between the hemoglobin inside a RBC, $C_{Hb,RBC}$ and plasma hemoglobin, $C_{Hb,Pl}$ [67].

$$J_{Hb} = k\,(C_{Hb,RBC} - C_{Hb,Pl})$$ (Eq. 6.1.4)

where the permeability coefficient of hemoglobin through RBC membrane, k, depends on shear stress intensity, exposure time, and mechanical behavior of RBCs' membrane.

By substituting the relevant equations, DI in SUB model can be written as:

$$DI_{SUB}(t,\tau;a,b) = 1 - \exp(-a[(\exp b\tau) - 1]\,t)$$ (Eq. 6.1.5)

The two constant parameters in Equation 6.1.5 (i.e. a and b which represent only the mechanical behavior of RBC membrane) should be obtained experimentally.

6.2 Materials and methods

Since hemolysis comprises both permeation of hemoglobin through RBC membrane as well as release of hemoglobin by RBC membrane breakdown, our proposed model is structured combining SUB and NUT models. In this respect, the synergy of the two physical phenomena behind blood trauma in a more realistic combined model can be considered. In order to validate our proposed model, an experimental setup containing a Couette device was employed.

The proposed model is a combination of both SUB and NUT models which we call it SN model, hereafter. DI in SN model is defined as the following:

$$DI_{SN}(t,\tau;\bar{t},\delta^2,a,b,c) = c * DI_{NUT}(t,\tau;\bar{t},\delta^2) + (1-c) * DI_{SUB}(t,\tau;a,b) \quad \text{(Eq. 6.2.6)}$$

where c is the proportionality coefficient, corresponds to the proportion-magnitude of NUT towards SUB model.

6.2.1 Experimental procedure

As shown in Figure 6.1, the Couette flow system comprising two coaxial cylinders was designed and constructed in order to generate a uniform shear flow (inner cylinder radius, r_1 = 34 (mm); and gap width, d= 1 (mm)). In this system, inner cylinder can rotate independently with the rotational speed of ω while the outer cylinder is stationary.
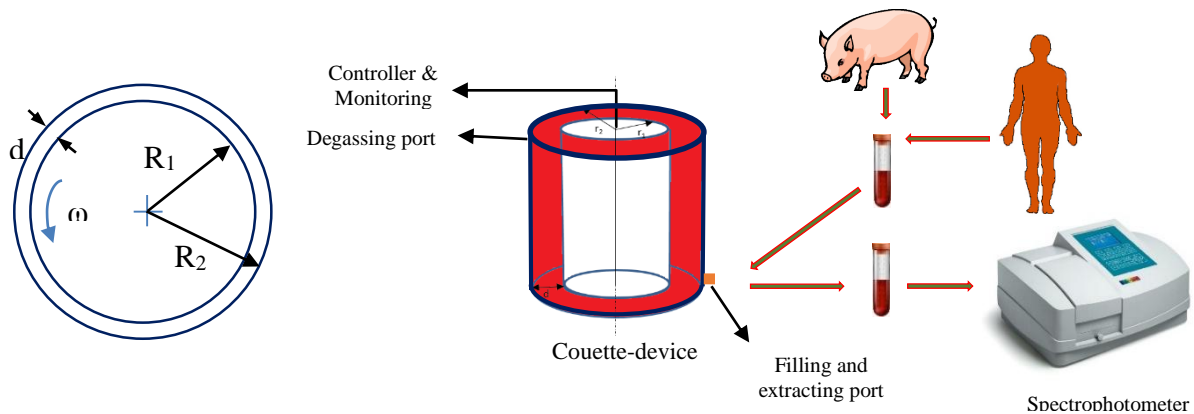
Figure 6.1: Graphical representation of the experimental procedure.

The experiments were conducted with freshly obtained porcine and human blood, adjusting hematocrit values at 36 %. Shear stress exposure time was set 120 (s). The generation of fPHb was measured with a spectrophotometer (Pharmacia Biotech, Cambridge, England) at the two wavelengths namely 540 and 680 (nm).

6.2.2 Data interpolation

In order to obtain parameters a and b in SN model, a curve fitting method was performed on experimental data using the R2014b version of MATLAB software. During this process, it was assumed that in low shear ranges (<6.5 (Pa)) the role of cell membrane breakdown is negligible.

Therefore, considering the SUB model, parameters *a* and *b,* were determined empirically by measuring hemolysis levels in a Couette device, where the flow remains within a low shear stress range. Accordingly, the extrapolated values of *a* and *b* are applicable for higher shear rates (since they are considered shear stress independent, refer to Equation 6.1.5) in SUB model. Other parameters (i.e. c, t̄ and δ²) can be calculated based on a and b values subsequently.

In order to validate the proposed model two different generally recognized data set, i.e. Heuser et al. [124] for porcine blood and Wurzinger et al. [97] for human blood, were utilized.

6.3   Results

6.3.1   Comparison of the predicted hemolysis with measured values

In order to calculate parameters a and b, hemolysis of both human and porcine blood was measured in different lower shear stress ranges. In this respect, DI was measured at different shear stresses in the range of 1 to 6.4 (Pa) at a constant shear stress exposure time (120 s) and hematocrit value (36%). The results of measured hemolysis values (DI), along with the predictions of the SN model, assuming c=0 (see discussion), are illustrated in Figure 6.2.
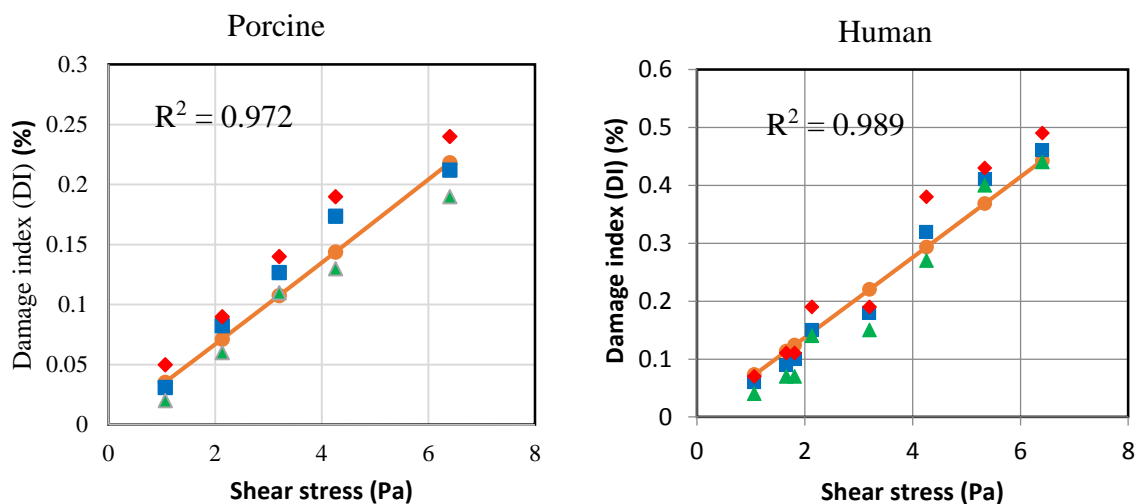
Figure 6.2: Hemolysis measurements (points) for porcine and human blood and the predicted course by SN model assuming c=0 (solid lines) for various shear stress values up to 6.4 Pa.

As it is shown in Figure 6.2, there is a good correlation between the experimentally measured data and the predicted course by SN model as a function of shear stress. According to this figure, parameters *a* and *b* can be extracted as presented in Table 6.1.

.

Blood Species	Human	Porcine
a (s^{-1})	0.0015	0.0003
b (Pa^{-1})	0.0038	0.0092

Table 6.1: Parameters a and b used in SN model

6.3.2   Model validation for porcine blood

In NUT model, according to homoscedasticity hypothesis [4], δ^2 is assumed as shear stress independent. The course of DI_{SN} was interpolated by curve fitting on the dataset of Heuser et al.[124], considering the values of *a* and *b* provided in table 1. In order to figure out the parameters c and $\bar{t}$ under a constant value of δ^2, different shear stress levels (132, 262, 378, 443, 498, 553 and 610 Pa) were employed. For each shear stress, hemolysis prediction of SN model was interpolated to calculate the values of these parameters. Table 6.2, summarizes the calculated parameters for porcine blood.

τ (Pa)	132	262	378	443	498	552	610
$\bar{t}$ (s)	0.92	0.89	0.81	0.75	0.68	0.67	0.51
δ^2 (s^2)				0.33			
c (-)	0.03	0.04	0.13	0.17	0.19	0.40	0.41

Table 6.2: The derived values of c and $\bar{t}$ for the relevant shear stress cases (porcine blood).

Figure 6.3 depicts a comparison of SN model with SUB and NUT models and with data obtained by Heuser et al.[124]. Their experiments were performed using porcine blood and DI data achieved by rotational viscometer at shear stress ranges from 132 to 610 (Pa) and exposure time from 3 to 700 (ms)[124].
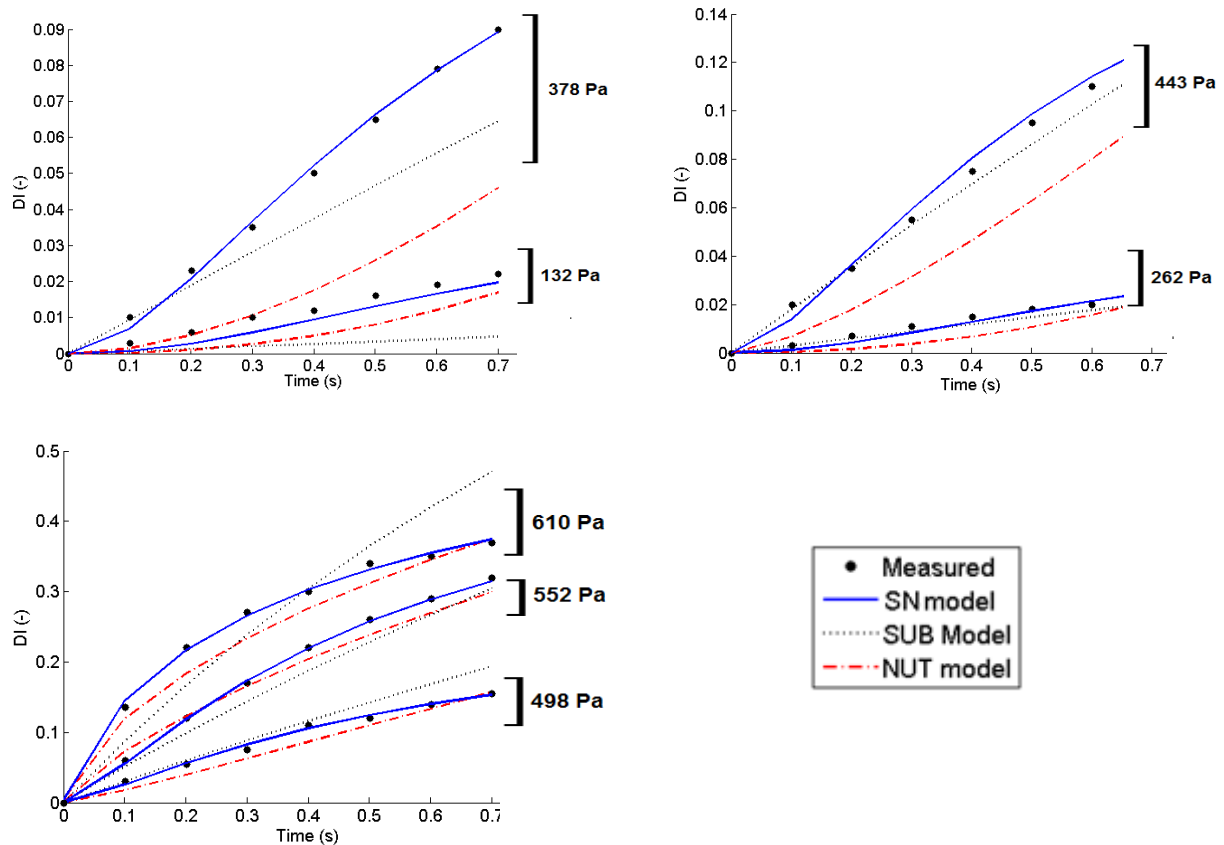
Figure 6.3: Prediction of the damage index (DI, solid lines) with the three different models: SN, NUT and SUB at different shear stress ranges (●indicates the measured values with porcine blood [124]).

Model validation for human blood

Figure 6.4 demonstrates the comparison between DI_{SN}, DI_{NUT}, DI_{SUB} and the dataset reported by Wurzinger et al. [97]. Their experiments were performed using human blood with hematocrit of 40 ±5 % and shear stress ranges from 120 to 535 (Pa) at applied shear stress exposure time of 14, 56, 113, 700 (ms)[97]. Similar to model validation to porcine blood, in order to calculate the optimal values of these parameters for human blood at each shear stress, hemolysis prediction of the SN model was interpolated. Table 6.3, summarizes the calculated parameters of c and $\bar{t}$ for human blood.

τ (Pa)	120	255	355	450	535
$\bar{t}$ (s)	0.6075	0.495	0.448	0.24	0.1075
δ^2 (s²)			0.12		
c (-)	0.07	0.12	0.35	0.76	0.94

Table 6.3: The derived values of c and $\bar{t}$ for the relevant shear stress cases (human blood).
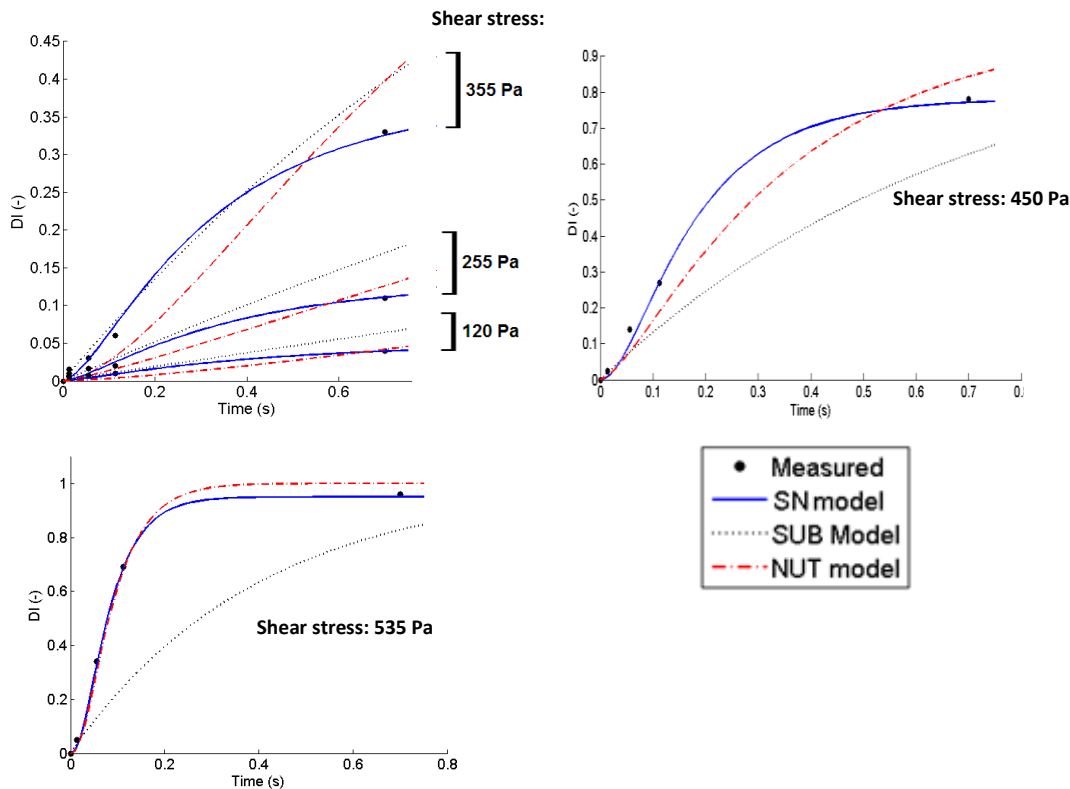
Figure 6.4: Prediction of the damage index (DI, solid lines) with the three different models: SN, NUT and SUB at different shear stress ranges(● indicates the measured values with human blood [97]).

6.4   Discussion

Based on Figure 6.2, an appropriate agreement between measured DI and DI predicted by SN model confirms the validity of neglecting hemolysis caused by cell membrane breakdown in this range of shear stress. It also reinforces the applicability of this assumption in the low shear stress ranges (<6.5 Pa) for both human and porcine blood.

Figure 6.3 explicitly shows a noticeable agreement between SN model and measured data. However DIs predicted by SUB and NUT models demonstrate remarkable deviations in respect with experiment at different shear stress ranges. This observation can be justified by missing

the contribution of hemolysis caused by membrane cell breakdown in SUB model as well as missing the contribution of sublethal hemolysis in NUT model.

Likewise, in the case of human blood, as it is demonstrated in Figure 6.4, there is a very fine accordance between DI predicted by SN model and measured ones at different shear stress levels whilst there are noticeable discrepancies between experimental data and DIs predicted by both SUB and NUT models.

Typically, a good agreement between a semi-experimental method and real data necessitates profound comprehension of the physical aspects related to the studied phenomena, as well as meticulous definition of the model's conditions. During the goal determination phase of this investigation, the aforementioned points were carefully considered in order to broaden the model's range of validity. On these grounds, both SUB and NUT models were combined in the presented model. The achieved agreement between the introduced model and actual data with shear stress values ranging up to 610 Pa, is the result of considering the principal, if not all, and most significant physical causes of hemolysis.

In regard to threshold time, the higher the value of $\bar{t}$, the more time a RBC can undergo a defined shear stress before the rupture of its membranes. The values presented in Table 6.2 show a descending trend for $\bar{t}$ when shear stress increases. This behavior can be rationalized if it is considered how drastically the probability of rupturing increases when shear stress rises as shown in Figure 6.5.

It is interestingly demonstrated in Figure 5 that mean value of threshold time ($\bar{t}$) for human RBCs generally lower that of porcine for shear stress ranges of 120 to 610 (Pa). Moreover, $\bar{t}$ for both human and porcine RBCs falls below 1 second at the mentioned shear ranges. In addition, Figure 6.5 obviously shows that by increasing shear stresses $\bar{t}$ for both human and porcine RBCs reduces correspondingly. However, it is noticeably reveal that the rate of $\bar{t}$ reduction is considerably higher for human in comparison with porcine erythrocytes. Based on this, the human erythrocytes seems to be more fragile than those of porcine. However, less reports on this specific phenomenon can be found in the literature.
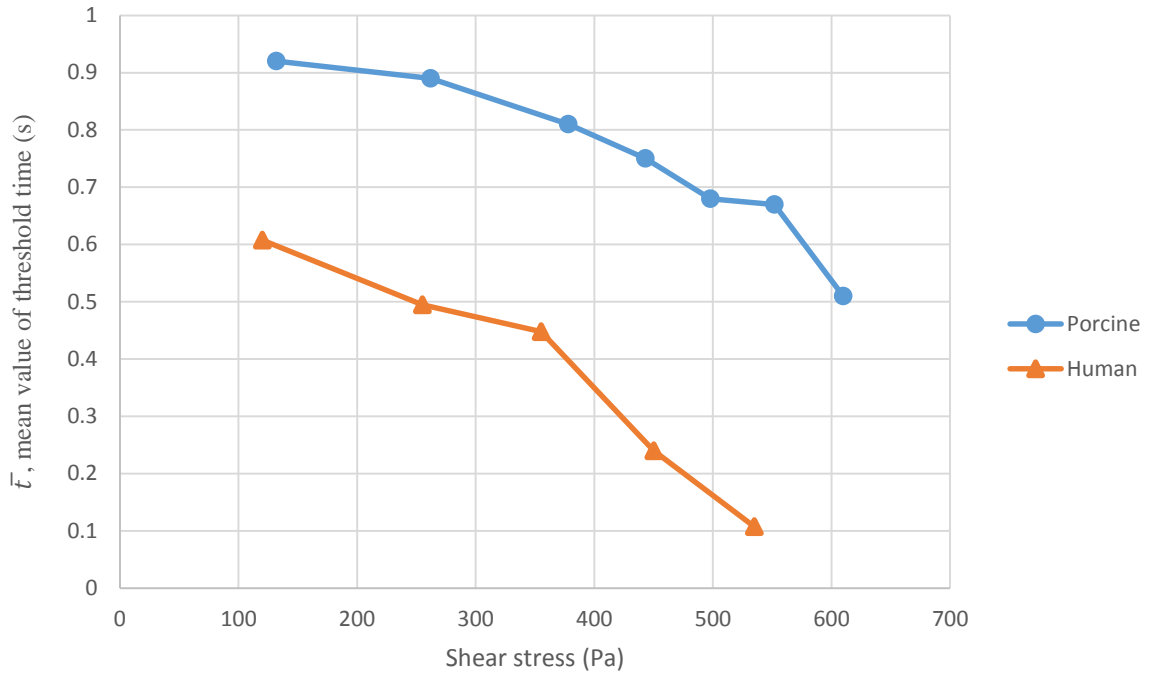
Figure 6.5: Mean value of threshold time ($\bar{t}$) as a function of shear stress.

Parameter *c* addresses the ratio of DI resulted by RBCs membrane breakdown (DI_{NUT}) to total DI ($DI_{NUT} + DI_{SUB}$). The values of parameter c obtained at diverse shear stress levels can be used to assess the proportion of each phenomenon (fPHb released by permeation or by cell membrane breakdown). Figure 6.6 represents the parameter c for both human and porcine blood at shear ranges between 120 and 610 (Pa).
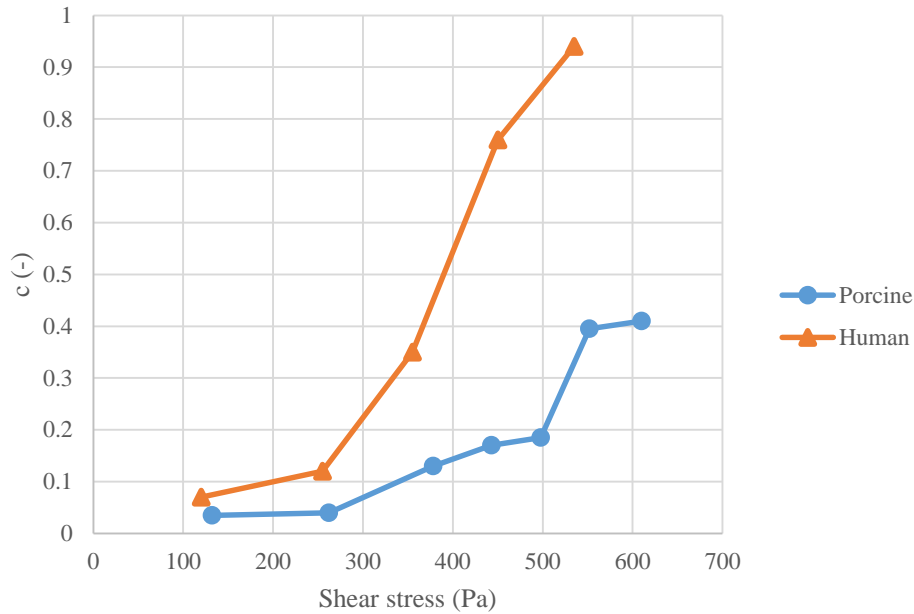
Figure 6.6: Proportion of the hemolysis mechanisms, c (calculated by permeation and cell rupture model) as a function of shear stress variations.

As illustrated in Figure 6.6, an increase of shear stress affects in an increase of the contribution of cell membrane rupturing in total hemolysis. For example, for the shear stress values of 450 and 443 Pa, respectively for human and porcine blood, c value for each are 0.76 and 0.17. It means at 450 Pa for human blood, 76% of total hemolysis is originating from cell membrane breakdown and the rest of 24% from sub-lethal mechanism. Whereas, in the case of porcine blood the influence of originated hemolysis from sub-lethal mechanism is dominated (by 83%) and only 17% of that is made through cell membrane destruction. It is remarkably demonstrated in Figure 6.56 that by increasing shear stresses, hemolysis in human blood is resulted more by cell membrane breakdown than that of porcine blood. Also here, less reports on this specific effect can be found in the literature.

Based on Figure 6.6, c can be calculated as below:

$$c_{Porcine} = 2 * 10^{-6}\, \tau^2 + 3 * 10^{-4}\, \tau + 0.018$$

and

$$c_{Human} = 4 * 10^{-6}\, \tau^2 + 5 * 10^{-3}\, \tau + 0.014$$

This figure shows that the assumption of c=0 at low shear stress ranges, used for calculating the parameters a and b in SN model, is reliable.

6.5   Conclusion

In contrast to previous models, the new model introduced here, offers a significantly higher agreement with the experimental data by considering the dominant phenomena in each shear stress range. The fact that all possible physical phenomena are taken into account, makes this model more realistic and at the same time enhances its agreement to the literature data for both human and porcine blood.

A prediction of the proportion of each phenomenon which serves to better understand the hemolysis mechanism becomes possible with this modelling. Ultimately, it is worth mentioning that besides describing the main hemolysis causes, semi-empirical models, due to their nature, can additionally augment a model's predictive capability both qualitatively as well as quantitatively. Determining the value of ($\bar{t}$), the average time after which cell membrane breakdown occurs under the applied conditions, is one of the phenomenological outcomes become possible with the proposed approach. Another outcome of using this semi-empirical model is to make possible to compute the proportionality coefficient c, and thereby to quantitatively predict the ratio between the involved phenomena in hemolysis. In other words, using here introduced model, the prediction of the dominant hemolysis mechanisms for human and porcine blood in a wide range of shear stress up to over 500 Pa and their percentages is possible.

Chapter 7

Hemodynamics and hemorheology in dialysis: effect of hematocrit variation

7.1   Introduction

Hemodialysis (HD) from the biomedical engineering point of view is a complex process and is thought for ESRD (end-stage renal disease) patients who have to undergo every other day, in order to eliminate artificially the toxic substances accumulating in the systemic blood, balancing the electrolytes as well as to discharge the excess water in their body. Such treatments last approximately 4-5 hours, during which the patient has to lie on a resting position, while his blood recirculates continuously through an extracorporeal circulation system including a hemodialyzer. The actual time these people have to invest for their therapies exceeds the 600 hours per annum (almost a complete month), which accordingly means that their blood cells spend this long time outside their natural environment and are under a trauma risk.

The stress exerted on blood cells by these intermittent treatments is widely acknowledged and investigated, yet it has not been optimally solved so far. This usually shear stress resulting to blood trauma, i.e. the destruction of erythrocytes that leads to the release of hemoglobin into the surrounding plasma. Here again it is measured its degree by the amount of free plasma hemoglobin. As already mentioned in the previous chapter, hemolysis is a depends on the degree of   shear stress and exposure time, but it is also affected by the surface hemocompatibility of the extracorporeal circuit's components mainly by dialyzer itself because of rather high surface area [31, 125].

As already mentioned in chapter 4, several different techniques such as hemofiltration, hemodiafiltration and hemofiltration are used for therapy of uremic patients. Therefore when in the following we talk about dialyzer, all of these methods are meant. The presented model is also applicable for artificial liver in which a dialyzer is employed as a part of the system. Blood flow rate through a dialyzer's fibers is relatively low (in contract to cardiac assist devices), which renders to lower grades of shear stress. On the other hand, the exposure time is much higher than those devices for one blood passage cycle due to low blood flow rate. Therefore, the rate of hemolysis cannot be neglected, especially when an elevated concentration of free hemoglobin released in the bloodstream (PfHb) can lead as it is reported to severe deterioration of the patient's condition and mortality e.g. for anaemic patients [126, 127].

The ability to monitor and minimize hemolysis is therefore imperative for uremic patients in order to minimize red blood cell destruction undergoing long term extracorporeal circulation of their blood.

In the case of those patient who are using the peritoneal technique, this modeling approach is not applicable. Because this therapeutical method does not require such filtration process happens in the hollow fibers.

7.2   Modeling

First, a model predicting the hematocrit variation and filtration rate along the dialyzer (fibers) length is formulated. The predicted filtration rate can be translate to the removal rate of excess water from the patients' body which is clinically important to be precisely controlled. The model introduced here is based on the modelling of filtration and backfiltration process for a single hollow fiber. High flux dialyzers are made of capillary membranes with micro-pores, which permit a noticeable amount of mass transfer between the blood and the dialysate compartment. The driving force for this exchange can be either a concentration difference through a diffusion mechanism or a pressure gradient through a convection mechanism. By these considerations, a prediction of the hemodynamic characteristics and mass transfer of the flow within the fibers is not as simple as it would seem. The impact of filtration and backfiltration on the fluid dynamics is affected by the pressure gradients, which in turn is influenced by hematocrit that fluctuates according to the dominant phenomenon (filtration/backfiltration). In addition, a rise in hematocrit affects viscosity in a homologous manner, which leads to a considerably wider range of shear stress values [31, 32]. In other words the hemodialysis process is an extraordinarily dynamic procedure, where the major parameters influence one another through a feedback mechanism and that makes determination of the outcome very complicated.

Notwithstanding the complexity of the dialysis procedure, advanced mathematics would most definitely provide a viable solution for the estimation of each parameter at a given point. A mathematical model would prove a valuable tool for the monitoring phase of the procedure, and could also presumably assist in discovering any flaws in the dialyzer's structure that may lead to an optimization of its design.

This study is explicitly established on conceiving methods of estimating the course of hematocrit along a fiber's length. A sophisticated mathematical model that yields Ultrafiltration Rate (UFR), Transmembrane Pressure (TMP) and ultimately the course of hematocrit (Hct) is formulated for this purpose. The results are validated by relevant in-vitro hemodialysis experiments, specifically designed according to the needs of this project (1st

validation case: twin module HD circuit, 2nd validation case: single module HD circuit with inverse flows). Our goal is to introduce this model as an eligible implement for the optimization of the operational conditions governing hemodialysis, and the minimization of blood trauma risk. This would be achieved by predicting the course of hematocrit and the development of viscosity in the capillary membrane, thus acquiring a more accurate map of the shear stress field. In addition, this model could pave the way for further development of the dialyzer's design through reconsideration of its geometrical characteristics (length, number of fibers, fiber diameter).

7.2.1   Model formulation

The mathematical model introduced in this chapter is founded on specific blood flow parameters that can be readily assessed and verified by the later introduced experimental procedure. These quantities include flow properties such as the flow rate of each liquid at the respective inlet (Q_{bi} and Q_{di}) and the ultrafiltration coefficient K, the dialyzer's geometrical characteristics (fiber length L and inner diameter D_i), as well as liquid properties (viscosity constants k and n – for hemodynamic analysis).

The independent variable in this model is the effective length of the hollow fibers l, ranging from 0 to L. Correspondingly, the unknowns flow rate, $Q_b(l)$, pressure, $P_b(l)$ and the hematocrit value, $Hct(l)$, can be identified as functions of the independent variable.

The present chapter hosts three variations of the introduced mathematical models differing in terms of complexity as well as in the working fluid media. At first, the model considering water as fluid medium is introduced, followed by the simplified and the advanced blood application models. Water, with its well defined rheological parameters, is undoubtedly an excellent candidate as working medium in the majority of fluid dynamics oriented investigations, and in this case it is used as proof of the model's application feasibility. The simplified blood model on the other hand, considers a constant oncotic pressure, in order to obtain an analytically practicable and solvable differential equation. Finally, the advanced blood model is defined on the basis of having minimal simplifications on the already mentioned oncotic pressure as a function of hematocrit, in an attempt to achieve now the highest possible agreement with the experimental data.

7.3 Model for water as fluid medium

As demonstrated by [75, 128], the flow distribution is minimally altered in the radial direction, nevertheless it can considered as "almost" uniform. Hence, the model can be applied on any fiber of the capillary membrane, as long as the inlet flow rate values in both compartments (blood – dialysate) remain constant. Aim of the water model is to predict the flow rate and the pressure drop along the dialyzer's fibers. The following schematic illustrates the volume flux balance as regarded by the mathematical model. Figure 7.1 shows a single hollow fiber that we established the model around it. In this figure, the inlet and outlet of the fiber (blood compartment) are considered as the water inlet and outlet for this modelling. Also in the dialysate compartment water flows and the only driving for water filtration and backfiltration is the pressure difference. The filtered water is also depicted as Q_f. The indices indicate the fluids: w = water, f = filtrate and d = dialysate, i and o indicate inlet and outlet.
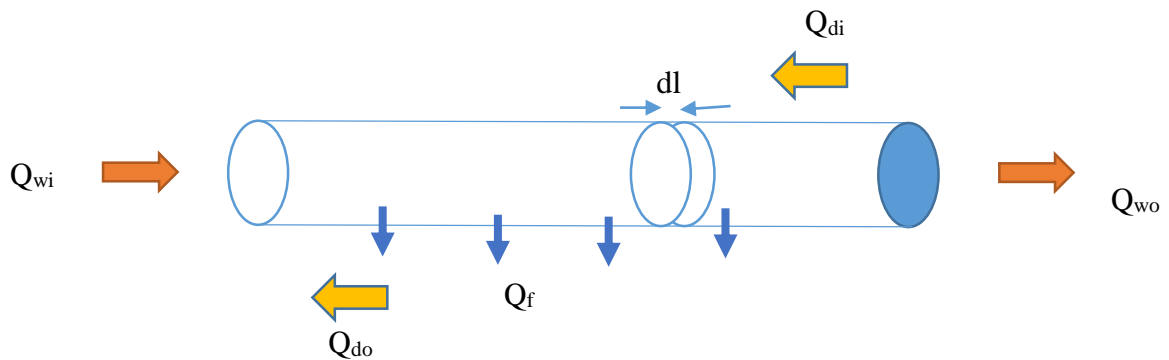
Figure 7.1: Schematic presentation of a hollow fiber of a dialyzer surrounded by dialysate in its compartment and filtration taking place across its length. w = water, f = filtrate and d = dialysate, i= inlet, o= outlet.

7.3.1 Assumptions

The following assumptions are adopted during the model establishment phase:

7.3.1.1 Dialysate pressure

Here it is assumed that pressure in dialysate compartment changes linearly, thus

$$P_d\left(l\right) = \frac{P_{di}-P_{do}}{L}\,l + \,P_{do} \qquad\qquad \text{(Eq. 7.3.1)}$$

7.3.1.2   Shear rate

Shear rate inside the hollow fibers has a non-linear progression and can be plainly regarded as the average shear rate in a pipe, based on Severs and Austin as stated below [129]:

$$\dot{\gamma} = {8V}/{D} = {4Q}/{\pi R^3} \qquad \text{(Eq. 7.3.2)}$$

7.3.1.3   Viscosity

Water viscosity is considered constant at room temperature [130]:

$$\mu = 1 \, mPa.s \qquad \text{(Eq. 7.3.3)}$$

7.3.1.4   Flow distribution

The flow distribution is considered as uniform between the fibers. According to Ronco et al [75, 128] flow distribution exhibits a minor deviation between peripheral and centrally situated capillaries which can be neglected. Therefore, it is postulated that this assumption lead to a minimal deviation. Under the assumption of a homogeneous flow distribution:

$$Q = N. \, Q_i^{fiber}$$

And

$$K = N.K^{fiber}$$

Where N is the number of fibers, and Q_i^{fiber} is the flow rate at the inlet of each fiber.

7.3.2   Model formulation

Based on all the previous assumptions, the composition of the model will commence. The amount of the filtrate flow for a single fiber in a microscopic volume element with the length of dl according to Fick's law can be assessed [57]:

$$dQ_f = N.K^{fiber} \, A \, \Delta P_{tm} \qquad \text{(Eq. 7.3.4)}$$

$$dQ_f = K \, A \, \Delta P_{tm}$$

$$dQ_f = K \, (2\pi R \, dl) \, [P_w(l) - P_d(l)] \qquad \text{(Eq. 7.3.5)}$$

By integrating both sides of the last equation over length:

$$Q_f(l) = \int_0^l K \, (2\pi R) \, [P_w(l) - P_d(l)]dl \qquad \text{(Eq. 7.3.6)}$$

$$Q_f(l) = (2\pi RK)\left[\int_0^l P_w(l)\,dl - \int_0^l \left(\frac{P_{di}-P_{do}}{L}\,l + P_{do}\right)dl\right] \qquad \text{(Eq. 7.3.7)}$$

$$Q_f(l) = c_1\left(\int_0^l P_w(l)\,dl - c_2 l^2 - c_3\,l + c_4\right) \qquad \text{(Eq. 7.3.8)}$$

Where $c_1 = 2\pi RK$, $c_2 = \frac{P_{di}-P_{do}}{2L}$ and $c_3 = P_{do}$.

It is also known:

$$Q_w(l) = Q_{wi} - Q_f(l) \qquad \text{(Eq. 7.3.9)}$$

$$Q_w(l) = Q_{wi} - c_1\left(\int_0^l P_w(l)\,dl - c_2 l^2 - c_3\,l + c_4\right) \qquad \text{(Eq. 7.3.10)}$$

On other hand:

$$\Delta P_w = P_{wi} - P_w(l) = \int_0^l dP_w \qquad \text{(Eq. 7.3.11)}$$

Since hollow fibers resemble cylindrical pipes and the flow is laminar, Hagen–Poiseuille equation for ΔP can be used:

$$\Delta P_w = \frac{8\,\mu\,l\,Q_w}{\pi R^4} \qquad \text{(Eq. 7.3.12)}$$

Similarly:

$$dP_w = \frac{8\,\mu}{\pi R^4}\,Q_w(l)\,dl \qquad \text{(Eq. 7.3.13)}$$

By substitution:

$$\Delta P = P_{wi} - P_w(l) = \frac{8\,\mu}{\pi R^4}\int_0^l Q_w(l)\,dl = \frac{8\,\mu}{\pi R^4}\int_0^l \left[Q_{wi} - c_1\left(\int_0^l P_w(l)\,dl - c_2 l^2 - c_3\,l + c_4\right)\right]dl \text{ (Eq. 7.3.14)}$$

From the derivative of Equation 7.3.14 the following equation is obtained:

$$-\acute{P}_w(l) = \frac{8\,\mu}{\pi R^4}\left[Q_{wi} - c_1\left(\int_0^l P_w(l)\,dl - c_2 l^2 - c_3\,l + c_4\right)\right] \qquad \text{(Eq. 7.3.15)}$$

Whereas the second derivative yields:

$$\acute{P}_w(l) = \frac{8\,\mu}{\pi R^4}\left[c_1(P_w(l) - 2c_2 l - c_3)\right] \qquad \text{(Eq. 7.3.16)}$$

Equation 7.3.16 is a second order linear ordinary differential equation. By solving this inhomogeneous second-order linear ordinary differential equation, the general solution of $P_b(l)$ will be obtained from:

$$P_w(l) = al + b$$

Where a and b are constants. Assuming the boundary conditions of:

$$P_w(0) = P_{wi}$$

$$P_w(L) = P_{wo}$$

Then the particular solution will have the following form.

$$\boldsymbol{P_w}(l) = \frac{P_{wo} - P_{wi}}{L} \, l + \boldsymbol{P_{wi}} \qquad \text{(Eq. 7.3.17)}$$

By substituting $Pw(l)$ into equation 7.3.10, $Q_b(l)$ is obtained.

$$Q_w(l) = Q_{wi} - \pi RK \left(\frac{P_{do} - P_{di} + P_{wo} - P_{wi}}{L} \right) l^2 - 2\pi RK(P_{wi} - P_{wo})l - 2\pi RK \, (c_4$$
$$+ \, c_5) \qquad \text{(Eq. 7.3.18)}$$

Since $Q_w(0) = Q_{wi}$, the term $c_4 + c_5 = 0$, so:

$$\boldsymbol{Q_w}(l) = \boldsymbol{Q_{wi}} - \boldsymbol{\pi RK} \left(\frac{P_{do} - P_{di} + P_{wo} - P_{wi}}{L} \right) l^2 - 2\pi RK(\boldsymbol{P_{wi}} - \boldsymbol{P_{do}})l \qquad \text{(Eq. 7.3.19)}$$

Hence, for $Q_f(l)$ by consideration of equation 7.3.9:

$$\boldsymbol{Q_f}(l) = \boldsymbol{Q_{wi}} - \boldsymbol{Q_w}(l) = \boldsymbol{\pi RK} \left(\frac{P_{do} - P_{di} + P_{wo} - P_{wi}}{L} \right) l^2 + 2\pi RK(\boldsymbol{P_{wi}} - \boldsymbol{P_{do}})l \qquad \text{(Eq. 7.3.20)}$$

Net ultrafiltration rate can be defined as:

$$\boldsymbol{UFR} = \boldsymbol{Q_f}(L) = \boldsymbol{\pi RK} \, (\boldsymbol{P_{wi}} + \boldsymbol{P_{wo}} - \boldsymbol{P_{di}} - \boldsymbol{P_{do}})\boldsymbol{L} \qquad \text{(Eq. 7.3.21)}$$

For clinical applications, it is reasonable to define and use an average transmembrane pressure ($\overline{TMP}$), as reported by Ronco et al.[57]:

$$\text{(Eq. 7.3.22)}$$

$$\overline{TMP}(l) = \frac{1}{l} \int_0^l dP_{tm}(l). \, dl = \frac{1}{l} \int_0^l \left[\frac{P_{wo} - P_{wi}}{L} \, l + P_{wi} - \frac{P_{di} - P_{do}}{L} \, l - P_{do} \right] dl$$

The general solution will appear as:

$$\overline{TMP}(l) = \frac{1}{l}\left[\frac{P_{wo}-P_{wi}-P_{di}+P_{do}}{2L}\, l^2 + \left(P_{wi} - P_{do}\right)l\right] \qquad \text{(Eq. 7.3.23)}$$

Eventually, the average $\overline{TMP}$ and the overall UFR in a dialyzer with length L can be obtained from the following equations:

$$\overline{TMP}(L) = \frac{P_{wo}+P_{wi}}{2} - \frac{P_{di}+P_{do}}{2} \qquad \text{(Eq. 7.3.24)}$$

$$UFR = Q_f(L) = 2\pi RKL\, \overline{TMP}(L) \qquad \text{(Eq. 7.3.25)}$$

7.4   Simplified model for blood as fluid medium

In a similar manner, implementation of the mathematical model on a single fiber using blood as working medium, could be feasible by taking the aforementioned parameters into consideration. A single hollow fiber of a dialyzer with constant inlet flow rate for both blood and dialysate medium is presumed. Target of this model is to predict the flow rate of blood and dialysate, as well as the development of transmembrane pressure along the dialyzer's fibers. Furthermore, this model can estimate the course of hematocrit along a fiber's length, by assessing the net ultrafiltration rate. The geometry of a single capillary with respect to the volume flux balance, is depicted in the drawing below.
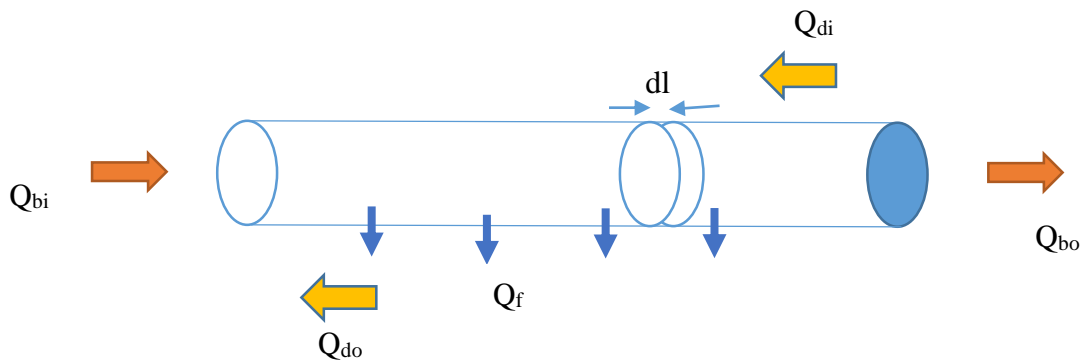
Figure 7.2: Schematic presentation of a single hollow fiber of a dialyzer surrounded by dialysate in its compartment and filtration taking place across its length. b = blood, f = filtrate and d = dialysate, i= inlet, o= outlet.

7.4.1 Assumptions

7.4.1.1 Dialysate pressure

Pressure in dialysate compartment changes in a linear fashion as described by equation 7.3.1.

7.4.1.2 Shear rate

Shear rate inside the hollow fibers has a non-linear progression and can be plainly regarded as the average shear rate in a pipe as described in equation 7.3.2.

7.4.1.3 Viscosity

Here for this modelling, an equation describing the relation between viscosity and shear rate is necessary, however there are a few reports in literature. Based on the Rosentrater [131], viscosity can be described as a power law equation given for porcine blood:

$$\mu = k \, \dot{\gamma}^{n-1} \qquad \text{(Eq. 7.4.1)}$$

Where k = 0.16 (Pa.s$^{0.39}$) and n= 0.39 (-).

In addition, viscosity is a function of hematocrit *Hct*, and according to Guth and Simha [132] it can be expressed in the following form:

$$\mu = \frac{\mu_i}{5}(1 + 2.5 \, Hct + 14.1 \, Hct^2) \qquad \text{(Eq. 7.4.2)}$$

These two functions can be merged into one as demonstrated below:

$$\mu = \frac{k \, \dot{\gamma}^{n-1}}{5}(1 + 2.5 \, Hct + 14.1 \, Hct^2) \qquad \text{(Eq. 7.4.3)}$$

On other the hand it is given that hematocrit changes along the fibers proportional to the ultrafiltration rate, and it can therefore be considered as a function of flow rate Q:

$$Hct \, (l) = \frac{Q_{bi} \, Hct_i}{Q_b(l)} = \frac{c_6}{Q_b(l)} \qquad \text{(Eq. 7.4.4)}$$

Where $c_6 = Q_{bi} \, Hct_i$. Hence viscosity along the fibers is:

$$\mu(l) = \frac{k\,\dot{\gamma}^{n-1}}{5}\left(1 + 2.5\,\frac{c_6}{Q_b(l)} + 14.1\,(\frac{c_6}{Q_b(l)})^2\right) \tag{Eq. 7.4.5}$$

Based on the previously reported equation for shear rate:

$$\mu(l) = \frac{k}{5}\,(\frac{4}{\pi R^3})^{n-1}\,(Q_b(l)^{n-1} + 2.5\,c_6 Q_b(l)^{n-2} + 14.1 c_6{}^2\,Q_b(l)^{n-3}) \tag{Eq. 7.4.6}$$

$$\mu(l) = c_7\,(Q_b(l)^{n-1} + 2.5\,c_6 Q_b(l)^{n-2} + 14.1 c_6{}^2\,Q_b(l)^{n-3}) \tag{Eq. 7.4.7}$$

Where:

$$c_7 = \frac{k}{5}\,(\frac{4}{\pi R^3})^{n-1}$$

7.4.1.4   Oncotic pressure

For simplification purposes, a constant average value for oncotic pressure is assumed [133]:

$$\pi\,(Hct = 0.4) = 24\,mmHg$$

7.4.1.5   Flow distribution

As mentioned in section 7.3.1, the flow distribution is considered as uniform between the peripheral and centrally situated fibers and the explained equations in this section are applicable.

7.4.2   Model formulation

The ultrafiltration rate taking place in a single fiber for a tiny voxel with length of *dl*, according to Fick's law can be replicated:

$$dQ_f = K^{fiber}\,dA^{fiber}\,\Delta P_{tm} \tag{Eq. 7.4.8}$$

Whereas for the complete fiber bundle in a dialyzer module, the net filtration rate is:

$$dQ_f = K\,dA\,\Delta P_{tm}$$

$$dQ_f = K\,(2\pi R\,dl)\,(P_b(l) - P_d(l) - \pi(l)) \tag{Eq. 7.4.9}$$

By integration of both sides over length:

$$Q_f(l) = \int_0^l K\,(2\pi R)\,(P_b(l) - P_a(l) - \pi(l)\,)dl \qquad \text{(Eq. 7.4.10)}$$

$$Q_f(l) = (2\pi RK)(\int_0^l P_b(l)\,dl - \int_0^l \left(\frac{P_{di}-P_{do}}{L}\,l + P_{do}\right)dl - \int_0^l(24\,mmHg)\,dl) \qquad \text{(Eq. 7.4.11)}$$

$$Q_f(l) = c_8\,(\int_0^l P_b(l)\,dl - c_9 l^2 - c_{10}\,l + c_{11}) \qquad \text{(Eq. 7.4.12)}$$

Where $c_8 = 2\pi RK$, $c_9 = \frac{P_{di}-P_{do}}{2L}$ and $c_{10} = P_{do} + 24\,mmHg$.

It is also known:

$$Q_b(l) = Q_{bi} - Q_f(l) \qquad \text{(Eq. 7.4.13)}$$

$$Q_b(l) = Q_{bi} - c_8\,(\int_0^l P_b(l)\,dl - c_9 l^2 - c_{10}\,l + c_{11}) \qquad \text{(Eq. 7.4.14)}$$

On the other hand:

$$\Delta P_b = P_{bi} - P_b(l) = \int_0^l dP_b \qquad \text{(Eq. 7.4.15)}$$

The fact that hollow fibers can be approximated as cylindrical pipes and the flow in them is laminar, permits the application of Hagen–Poiseuille equation for ΔP:

$$\Delta P_b = \frac{8\,\mu\,l\,Q_b^{fiber}}{\pi R^4} \qquad \text{(Eq. 7.4.16)}$$

And here:

$$dP_b = \frac{8}{\pi N R^4}\,\mu\,(l)Q_b(l)dl \qquad \text{(Eq. 7.4.17)}$$

By substitution:

$$\Delta P = P_{bi} - P_b(l) = \frac{8}{\pi N R^4}\int_0^l \mu\,(l)\,Q_b(l)dl \qquad \text{(Eq. 7.4.18)}$$

$$= \frac{8\,c_7}{\pi N R^4}\int_0^l (Q_b(l)^n + 2.5\,c_6 Q_b(l)^{n-1} + 14.1 c_6{}^2\,Q_b(l)^{n-2})\,dl$$

This equation using $P_b(l)$ from the derivative of Equation 7.4.14 can be rewritten:

$$\acute{Q}_b(l) = -c_8\,(P_b(l) - 2c_9 l - c_{10}) \qquad \text{(Eq. 7.4.19)}$$

$$P_b(l) = \frac{-\acute{Q}_b(l)}{c_8} + 2c_9 l + c_{10} \qquad \text{(Eq. 7.4.20)}$$

From equation 7.4.20, $P_b(l)$ is substituted into equation 7.4.18:

$$P_{bi} + \frac{\acute{Q}_b(l)}{c_8} - 2c_9 l - c_{10} = \frac{8c_7}{\pi NR^4} \int_0^l (Q_b(l)^n + 2.5\, c_6 Q_b(l)^{n-1} + 14.1 c_6{}^2\, Q_b(l)^{n-2})\, dl$$

(Eq. 7.4.21)

The derivative of Equation 7.4.21 over length yields:

$$\acute{Q}_b(l) = c_{12}\, Q_b(l)^n + c_{13}\, Q_b(l)^{n-1} + c_{14}\, Q_b(l)^{n-2} + c_{15}$$

(Eq. 7.4.22)

Where $c_{12} = {}^{8\, c_7\, c_8}/_{\pi NR^4}$, $c_{13} = 20\, {}^{c_7\, c_8 c_6\, c_{12}}/_{\pi NR^4}$,

$$c_{14} = {}^{112.8\ c_7\, c_8 c_6{}^2\, c_{12}}/_{\pi NR^4}$$

and $c_{15} = 2\, c_8\, c_9$.

Equation 7.4.22 is a second order non-linear ordinary differential equation. Its solution will yield $Q_b(l)$. Subsequently, substitution of $Q_b(l)$ into equation 7.4.20 will grant $P_b(l)$. Likewise, substitution of $Q_b(l)$ into equation 7.4.4, will result in $Hct(l)$.

$$Q_b(l) = \frac{c_{12}\, l^{n+2}}{n^2 + 3n + 2} + \frac{c_{13} l^{n+1}}{n^2 + n} + \frac{c_{14}\, l^n}{n^2 - n} + \frac{c_{15} l^2}{2} + c_{16} l + c_{17}$$

(Eq. 7.4.23)

where $c_{17} = Q_{bi}$, Derivative of Q_b will be:

$$\acute{Q}_b(l) = \frac{c_{12}\, l^{n+1}}{n+1} + \frac{c_{13} l^n}{n} + \frac{c_{14}\, l^{n-1}}{n-1} + c_{15} l + c_{16}$$

(Eq. 7.4.24)

After substitution $\acute{Q}_b(l)$ into equation 7.4.20:

(Eq. 7.4.25)

$$P_b(l) = -\frac{1}{c_8}\left(\frac{c_{12}\, l^{n+1}}{n+1} + \frac{c_{13} l^n}{n} + \frac{c_{14}\, l^{n-1}}{n-1}\right) - \frac{c_{16}}{c_8} + c_{10}$$

Application of boundary condition $P_b(0) = P_{bi}$: $c_{10} - {}^{c_{16}}/_{c_8} = P_{bi}$ and

$c_8 * (P_{do} + 3189 - P_{bi}) = c_{16}$, so $P_b(L) = P_{bo}$

Then

$$P_b(L) = -\frac{c_{18}}{c_8}\left(\frac{c_{12}\, L^{n+1}}{n+1} + \frac{c_{13} L^n}{n} + \frac{c_{14}\, L^{n-1}}{n-1}\right) + P_{bi}$$

(Eq. 7.4.26)

Where:

$$c_{18} = \frac{c_8 \, (P_{bi} - P_{bo})}{(\frac{c_{12} \, L^{n+1}}{n+1} + \frac{c_{13} L^n}{n} + \frac{c_{14} \, L^{n-1}}{n-1})}$$

Substitution into Equation 7.4.20 gives us blood flow rate:

$$Q_b(l) = \frac{c_{12} \, l^{n+2}}{n^2 + 3n + 2} + \frac{c_{13} l^{n+1}}{n^2 + n} + \frac{c_{14} \, l^n}{n^2 - n} + \frac{c_{15} l^2}{2} + c_{16} l + Q_{bi} \quad \text{(Eq. 7.4.27)}$$

Hence filtration rate can be calculated according to the formula below:

$$Q_f(l) = -c_{16} l - \frac{c_{15} l^2}{2} - \frac{c_{12} \, l^{n+2}}{n^2 + 3n + 2} - \frac{c_{13} l^{n+1}}{n^2 + n} - \frac{c_{14} \, l^n}{n^2 - n} \quad \text{(Eq. 7.4.28)}$$

$$UFR = Q_f(L) = -c_{16} L - \frac{c_{15} L^2}{2} - \frac{c_{12} \, L^{n+2}}{n^2 + 3n + 2} - \frac{c_{13} L^{n+1}}{n^2 + n} - \frac{c_{14} \, L^n}{n^2 - n}$$

$$\text{(Eq. 7.4.29)}$$

From the definition of $\overline{TMP}$ (average transmembrane pressure):

$$\overline{TMP}(l) = \frac{1}{l} \int_0^l dP_{tm}(l). \, dl \quad \text{(Eq. 7.4.30)}$$

$$\overline{TMP}(l) = \frac{1}{l} \int_0^l [P_b(l) - P_d(l) - \pi(l)] dl$$

$$\overline{TMP}(l) = \frac{1}{l} \int_0^l \left(\left(-\frac{\left(8 \, c_7 \big/ \pi N R^4 \right) l^{n+1}}{n+1} - \frac{\left(20 \, {}^{c_7 \, c_6 \, c_{12}} \big/ \pi N R^4 \right) l^n}{n} - \frac{\left(112.8 \, {}^{c_7 \, c_6{}^2 \, c_{12}} \big/ \pi N R^4 \right) l^{n-1}}{n-1} \right. \right.$$

$$\left. \left. + P_{bi} \right) - \left(\frac{P_{di} - P_{do}}{L} \, l + P_{do} \right) - 24 \right) dl$$

After integration and applying the boundary condition, the average transmembrane pressure in a dialyzer with length L can be calculated:

$$\overline{TMP}(L) = \frac{1}{L} \left(-\frac{P_{di} - P_{do}}{2L} L^2 + (P_{bi} - P_{do})L - \frac{\left(\frac{8\, c_7}{\pi NR^4} \right) L^{n+2}}{n^2 + 2n + 3} \right.$$
$$\left. -\frac{\left(\frac{20\, c_7\, c_6\, c_{12}}{\pi NR^4} \right) L^{n+1}}{n^2 + n} - \frac{\left(\frac{112.8\, c_7\, c_6{}^2\, c_{12}}{\pi NR^4} \right) L^n}{n^2 - n} \right) \qquad \text{(Eq. 7.4.31)}$$

Accordingly, the hematocrit value at any given point along the fiber is predicted by the following equation:

$$Hct\,(l) = \frac{Q_{bi}\, Hct_i}{Q_b(l)} = \frac{c_6}{Q_b(l)} = \frac{c_6}{\frac{c_{12}\, l^{n+2}}{n^2 + 3n + 2} + \frac{c_{13} l^{n+1}}{n^2 + n} + \frac{c_{14}\, l^n}{n^2 - n} + \frac{c_{15} l^2}{2} + c_{16} l + Q_{bi}}$$

(Eq. 7.4.32)

7.5   Advanced blood model for blood as fluid medium

The advanced blood model is almost identical to its already introduced simplified version, however it differentiates itself by not considering oncotic pressure as constant, whereas it is regarded as a function of hematocrit. A single hollow fiber of a dialyzer with constant inlet flow rate for both blood and dialysate medium is presumed as depicted in Figure 7.2. Goal of this model is to predict the flow rate of blood and dialysate, as well as the development of transmembrane pressure along the dialyzer's fibers. In addition, the advanced blood model can estimate with high precision the course of hematocrit along the length of the fiber, by assessing the net ultrafiltration rate.

7.5.1   Assumptions

7.5.1.1   Dialysate pressure

Pressure in dialysate compartment changes in a linear fashion as described by equation 7.3.1.

7.5.1.2   Shear rate

Shear rate inside the hollow fibers has a non-linear progression and can be plainly regarded as the average shear rate in a pipe as described in equation 7.3.2.

7.5.1.3 Viscosity

As mentioned in section 7.4.1, the rather complex course of viscosity can be described as in (Eq. 7.4.7). In order to solve the final differential equation analytically in the advanced model it is replaced with a polynomial equation as described below.

$$\mu(l) = 163 \frac{c_6^2}{Q_b(l)^2} - 28.7 \frac{c_6}{Q_b(l)} + 3.9 = 163\, Hct^2 - 28.7\, Hct + 3.9 \quad \text{(Eq. 7.5.1)}$$

As depicted in Figure 7.33, Eq. 7.4.7 shows remarkably high agreement with the above mentioned polynomial equation. Please not that, in order to operate with hematocrit values, the term $\frac{c_6}{Q_b(l)}$ is substitute by Hct (see Eq. 7.4.4).

y = 163.01x² - 28.703x + 3.926
R² = 0.999
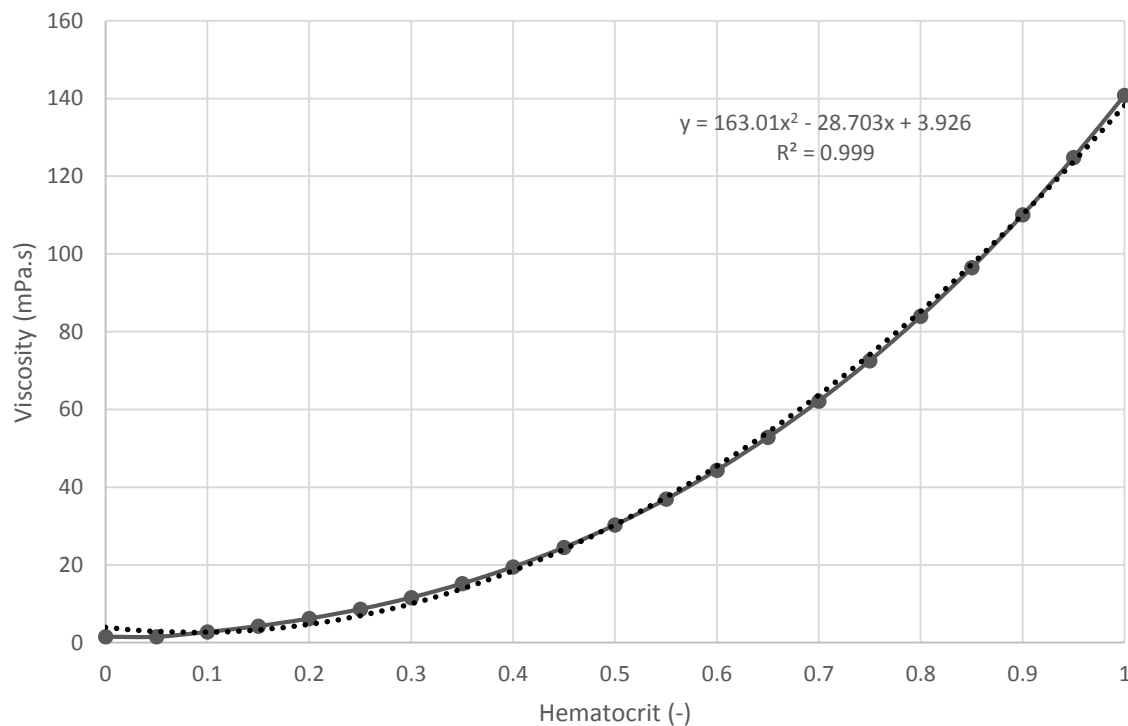
Figure 7.3: Comparison of viscosity calculated by equation 7.4.9 (dashed curve) with the simplified polynomial equation 7.5.1 (solid line).

7.5.1.4 Oncotic pressure

Oncotic pressure is considered to be a function of protein concentration in blood plasma. The relationship between pressure and protein concentration can be approximated by the following formula, first introduced by and Pappenheimer [134]:

$$\pi(c) = 2.1\, C_p + 0.16\, C_p{}^2 + 0.009\, C_p{}^3 \qquad \text{(Eq. 7.5.2)}$$

In this chapter it is assumed that the main volume of proteins generating oncotic pressure chiefly consists of albumin, which cannot permeate the capillary membrane. In addition, blood protein concentration and hematocrit share a linear relationship, therefore:

$$\pi(c) = 2.1\, Hct + 0.16\, Hct^2 \qquad \text{(Eq. 7.5.3)}$$

And

$$\pi(c) = \frac{2.1 c_6}{Q_b(l)} + \frac{0.16\, c_6{}^2}{Q_b(l)^2} \qquad \text{(Eq. 7.5.4)}$$
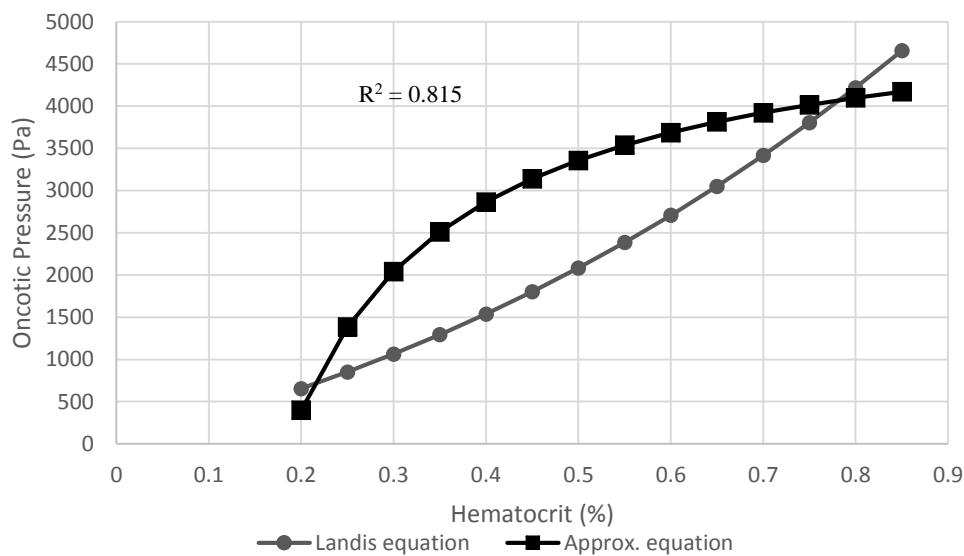
Figure 7.4: Approximation of the Landis equation for Oncotic Pressure with a simplified equation.

For simplification purposes an in order to be able to solve the final equation analytically, the oncotic pressure will be approximated by the following equation, which as the graph above demonstrates (Figure 7.4), shows some agreement to the original equation.

$$\pi(Hct(l)) = \frac{-984}{Hct(l)} + 5320 \qquad \text{(Eq. 7.5.5)}$$

7.5.1.5   Flow distribution

As mentioned in section 7.3.1, the flow distribution is considered as uniform between the peripheral and centrally situated fibers and the explained equations in this section are applicable.

7.5.2 Model Formulation

Ultrafiltration rate of a single capillary can be approximated by a microscopic volume with surface equal to the cross-section of the hollow fiber and length of *dl,* according to Fick's law:

$$dQ_f = K^{fiber} \, dA^{fiber} \, \Delta P_{tm} \qquad \text{(Eq. 7.5.6)}$$

Which for the dialyzer module as a whole it will become:

$$dQ_f = K \, dA \, \Delta P_{tm}$$

$$dQ_f = K \, (2\pi R \, dl) \left(P_b(l) - P_d(l) - \pi(l) \right) \qquad \text{(Eq. 7.5.7)}$$

Integration of Equation 7.5.7 over length yields:

$$Q_f(l) = \int_0^l K \, (2\pi R) \left(P_b(l) - P_d(l) - \pi(l) \right) dl \qquad \text{(Eq. 7.5.8)}$$

$$Q_f(l) = (2\pi R K) \left[\int_0^l P_b(l) \, dl - \int_0^l \left(\frac{P_{di} - P_{do}}{L} \, l + P_{do} \right) dl - \int_0^l \left({-984}/{Hct(l)} + 5320 \right) dl \right]$$

$$\text{(Eq. 7.5.9)}$$

$$Q_f(l) = c_8 \left[\int_0^l P_b(l) \, dl - \int_0^l \left({-984}/{Hct(l)} + 5320 \right) dl - c_9 l^2 - P_{do} \, l \right] \qquad \text{(Eq. 7.5.10)}$$

Where $c_8 = 2\pi R K$, $c_9 = \frac{P_{di} - P_{do}}{2L}$. It is known that:

$$Q_b(l) = Q_{bi} - Q_f(l) \qquad \text{(Eq. 7.5.11)}$$

$$Q_b(l) = Q_{bi} - c_8 \left[\int_0^l P_b(l) \, dl - \int_0^l \left({-984}/{Hct(l)} + 5320 \right) dl - c_9 l^2 - P_{do} \, l \right] \qquad \text{(Eq. 7.5.12)}$$

On the other hand:

$$\Delta P_b = P_{bi} - P_b(l) = \int_0^l dP_b \qquad \text{(Eq. 7.5.13)}$$

Hollow fibers can be regarded as cylindrical pipes, and the flow in them is laminar, therefore Hagen–Poiseuille equation [6] can be employed for *ΔP* estimation:

$$\Delta P_b = {8 \, \mu \, l \, Q^{fiber}}/{\pi R^4} \qquad \text{(Eq. 7.5.14)}$$

And here:

$$dP_b = \frac{8}{\pi N R^4} \mu\,(l)Q(l)dl \qquad \text{(Eq. 7.5.15)}$$

By substitution:

$$\Delta P = P_{bi} - P_b(l) = \frac{8}{\pi N R^4} \int_0^l \mu\,(l)\,Q_b(l)dl \qquad \text{(Eq. 7.5.16)}$$

$$= \frac{8\,c_7}{\pi N R^4} \int_0^l \left(163\,c_6^2\,Q_b(l)^{-1} - 28.7\,c_6 + 3.9\,Q_b(l)\right) dl$$

Equation 7.5.16 can be rewritten using $P_b(l)$ from the derivative of Equation 7.5.12:

$$\acute{Q}_b(l) = -\,c_8\,(P_b(l) - 2c_9 l - P_{do} + {^{984}/_{Hct(l)}} - 5320) \qquad \text{(Eq. 7.5.17)}$$

$$P_b(l) = \frac{-\acute{Q}_b(l)}{c_8} + 2c_9 l + P_{do} - {^{984}/_{Hct(l)}} + 5320 \qquad \text{(Eq. 7.5.18)}$$

Substitution of $P_b(l)$ from Equation 7.5.18 into Equation 7.5.16:

$$P_{bi} + \frac{\acute{Q}_b(l)}{c_8} - 2c_9 l - P_{do} + \frac{984}{Hct(l)} - 5320 \qquad \text{(Eq. 7.5.19)}$$

$$= \frac{8c_7}{\pi N R^4} \int_0^l (163c_6^2\,Q_b(l)^{-1} - 28.7c_6 + 3.9Q_b(l))\,dl$$

From the derivative of Equation 7.5.19 over length, it is obtained:

$$\acute{Q}_b(l) = \left(c_{12}\,Q_b(l)^{-1} + c_{13} + c_{14}\,Q_b(l)\right) \qquad \text{(Eq. 7.5.20)}$$

Where
$$c_{12} = {^{1300\,c_6^2 c_7\,c_8}/_{\pi N R^4}}\,, \quad c_{13} = 2\,c_8\,c_9 - 230\,{^{c_6\,c_7\,c_8}/_{\pi N R^4}}$$

$$\text{and } c_{14} = {^{31\,c_7\,c_8}/_{\pi N R^4}} + {^{984\,c_8}/_{c_6}}$$

Since c_{12} is several orders of magnitude smaller than c_{13} and $c_{14,}$ it can be neglected, hence Equation 7.5.20 becomes:

$$\acute{Q}_b(l) = c_{13} + c_{14}\,Q_b(l) \qquad \text{(Eq. 7.5.21)}$$

Equation 7.5.21 is a second order non-linear ordinary differential equation. Solving this will yield $Q_b(l)$. A subsequent substitution of $Q_b(l)$ into Equation 7.5.18, will provide us with $P_b(l)$. Finally $Hct(l)$ can be obtained by substituting $Q_b(l)$ into Equation 7.4.6.

$$Q_b(l) = \frac{c_{13}}{c_{14}} + c_{15}e^{\sqrt{c_{14}}\,l} + c_{16}e^{-\sqrt{c_{14}}\,l} + c_{17} \qquad \text{(Eq. 7.5.22)}$$

Where c_{15}, c_{16} and c_{17} are the integration constants.

Thusly, the derivative of $Q_b(l)$ will be:

$$\acute{Q}_b(l) = c_{15}\sqrt{c_{14}}\,e^{\sqrt{c_{14}}\,l} - c_{16}\sqrt{c_{14}}\,e^{-\sqrt{c_{14}}\,l} \qquad \text{(Eq. 7.5.23)}$$

Substitution $\acute{Q}_b(l)$ into Equation 7.5.18:

$$P_b(l) = -\frac{1}{c_8}\left(c_{15}\sqrt{c_{14}}\,e^{\sqrt{c_{14}}\,l} - c_{16}\sqrt{c_{14}}\,e^{-\sqrt{c_{14}}\,l}\right) + 2c_9 l + P_{do}$$
$$- \frac{984}{c_6}\left(\frac{c_{13}}{c_{14}} + c_{15}e^{\sqrt{c_{14}}\,l} + c_{16}e^{-\sqrt{c_{14}}\,l} + c_{17}\right) + 5320 \qquad \text{(Eq. 7.5.24)}$$

After the necessary simplifications:

$$P_b(l) = -c_{15}\left(\frac{\sqrt{c_{14}}}{c_8} + \frac{984}{c_6}\right)e^{\sqrt{c_{14}}\,l} + c_{16}\left(\frac{\sqrt{c_{14}}}{c_8} - \frac{984}{c_6}\right)e^{-\sqrt{c_{14}}\,l}$$
$$+ 2c_9 l + P_{do} + 5320 - \frac{c_{13}}{c_{14}} \qquad \text{(Eq. 7.5.25)}$$

Application of the boundary conditions for pressure: $P_b(0) = P_{bi}$ and $P_b(L) = P_{bo}$ grants us the values of the following constants:

$$c_{15} = 10^{-8} * (0.041 * TMP - 52.3)$$

$$c_{16} = 10^{-8} * (0.1356 * TMP - 37.1)$$

$$c_{17} = Q_{bi} - c_{15} - c_{16} - \frac{c_{13}}{c_{14}}$$

Application of the boundary condition for flow rate: $Q_b(0) = Q_{bi}$:

$$Q_b(l) = c_{15}e^{\sqrt{c_{14}}\,l} + c_{16}e^{-\sqrt{c_{14}}\,l} + Q_{bi} - c_{15} - c_{16} \qquad \text{(Eq. 7.5.26)}$$

Hence:

$$Q_f(l) = c_{15} + c_{16} - c_{15}e^{\sqrt{c_{14}}\,l} - c_{16}e^{-\sqrt{c_{14}}\,l} \qquad \text{(Eq. 7.5.27)}$$

$$UFR = Q_f(L) = c_{15} + c_{16} - c_{15}e^{\sqrt{c_{14}}\,L} - c_{16}e^{-\sqrt{c_{14}}\,L} \qquad \text{(Eq. 7.5.28)}$$

$$Hct\,(l) = \frac{Q_i\,Hct_i}{Q(l)} = \frac{c_6}{Q(l)} = \frac{c_6}{c_{15}e^{\sqrt{c_{14}}\,l} + c_{16}e^{-\sqrt{c_{14}}\,l} + Q_{bi} - c_{15} - c_{16}}$$

$$\text{(Eq. 7.5.29)}$$

The validation of introduced models in this chapter will be evaluated in chapter 8 and 9.

Chapter 8

Experimental model validation methods with hemodialyzers/hemofiltration circuits

8.1   Part 1: Hemodialysis circuit with serially connected dialyzers

Here, the experimental method is described which is applied for the validation of the mathematical models introduced in the previous chapter. In order to investigate the effects of filtration and backfiltration on the hematocrit fluctuation, described earlier in chapter 4, an in vitro circulation system is designed. Initially the reader will be familiarized with the Materials and Methods employed in this system, and eventually the obtained results will be compared with model predictions.

8.1.1   Materials and methods

Besides the usual components, specially tailored components are used and designed for this investigation. The working fluids, dialyzers, sensors and special components are described as following:

8.1.1.1   Working fluids preparation

Medical grade distilled water is used in this study as a preventative measure against nano particle depositions in the circuit leading to fouling the pores of the hollow fibers.

Blood investigations are carried out by using of fresh porcine blood (approx. 4-5 liters per experiment) gathered carefully in slaughterhouse, anticoagulated with heparin (10 units/ml blood), while isotonic solution (NaCl 0.9%) serves as a substitute for dialysate liquid. In addition, it is used for blood dilution in order to adapt the initial hematocrit value to the ranges typically measured during the clinical applications.

8.1.1.2   Dialyzers

The dialyzers implemented in this study were appreciatively provided by B.Braun Melsungen AG. A model from a high flux dialyzers type (xevonta Hi 18 with the surface area (1.8 m^2)) was selected in order to reach sufficient hematocrit values for blood investigations and additionally possessing the ideal geometrical characteristics of its outer shell. Water studies were carried out with a broader range of models Xevonta (Hi 10 / 15 / 18 / 23), in order to evaluate the impact of surface area and priming volume on UFR and TMP (see table 8.1). The

membrane material – Polysulfone (PSu) interlaced with Polyvinylpyrrolidone (PVP) – is identical in all four models.

	Hi 10	Hi 15	Hi 18	Hi 23
$V_{prim.}$ (mL)	54	90	103	135
L_{eff} (mm)	245	245	285	285
A_{eff} (m²)	1.0	1.5	1.8	2.3
d_{in} (μm)	195	195	195	195
t_w (μm)	35	35	35	35
N_{HF}	6600	10000	10300	13200

Table 8.1: Geometrical characteristics of all four dialyzer models used for validation purpose. V_{prim}: priming volume, L_{eff}: effective length, A_{eff} : effective surface area, d_{in}: inner diameter, t_w: hollow fiber wall thickness and N_{HF}: number of hollow fibers in each module.

8.1.1.3   Circuits components

Two peristaltic pumps (roller pumps) for hemodialyzer applied for their usual clinical flow rates were used. A third roller pump is used for recirculating the content of the blood reservoir, in order to keep the hematocrit constant and preventing the sedimentation. Two regular blood reservoirs were used for collecting the blood and dialysate fluid during the circulation (see Figure 8.1 and 8.2).

8.1.1.4   Pressure monitoring

A pressure monitoring device (Siemens SIRECUST 404) including pressure sensors was used in order to monitor continuously the pressure course along the circuit. Each dialyzer port is associated with one sensor. In the case that the system comprises two dialyzer modules, 6 pressure sensors are required (see Figure 8.1 and 8.2).

8.1.1.5   Pressure control and regulation

The revolutions of the two pumps driving the blood and dialysate fluid through the dialyzers are adjusted in the way that generate the typical clinical flow rates (i.e. 300mL/min for blood, and 500mL/min for dialysate). In order to control the ultrafiltration rate, a restrictor clamp is applied, as it is shown in Figure 8.1 and 8.2, to produce variable flow resistance. This clamp can either increase or decrease the pressure difference between the two flows, thus adjusting the driving force of convection.

8.1.1.6   Experimental circuits

The hemodialysis circuit features several special characteristics, major amongst, the implementation of two dialyzer modules in serial configuration, for elongation the dialyzer length by using two standard dialyzers. In this way, the monitoring of the hematocrit's course along the fibers' length is elongated.

Since sampling the blood from inside the fibers during an ongoing investigation is impossible, the sampling sites were located just before the inlet and after the outlet port of the dialyzer. In the case of the above mentioned serial configuration, a third sampling point was added between the two modules.

The connection between the two modules is completed in two ways: first, with a conventional connector between the modules, in order to control the stability of the flow parameters (pressure etc.) and to verify the validity of the results (filtration, Hct.). Second, by a custom made connector (when the caps are removed). This connector, called sleeve coupling, also bears a 3-way cocks on its surface that enables liquid sampling as well as pressure monitoring. This was necessary to find out the optimal connection of two dialyzers.

A closed loop configuration is utilized in both blood and water experiments (Figure 8.1 and 8.2). The main reasons for this choice is the ability to maintain constant priming volume conditions throughout the investigation period.

8.1.1.6.1 Circuit for investigations with water as fluid

The serially connected dialyzers set was initially tested with water providing filtration investigation without the influence of blood cells (actually pure blood plasma were also a reasonable option, however because of the risk of fouling the hollow fiber membrane pores and very close rheological characteristic to water, water is still a reliable choice). Therefore, Distilled water is used as a substitute for both blood and dialysate fluid therefore no diffusion taking place in the dialyzers between the two compartments. The sketch of this circuit is presented in Figure 8.1.
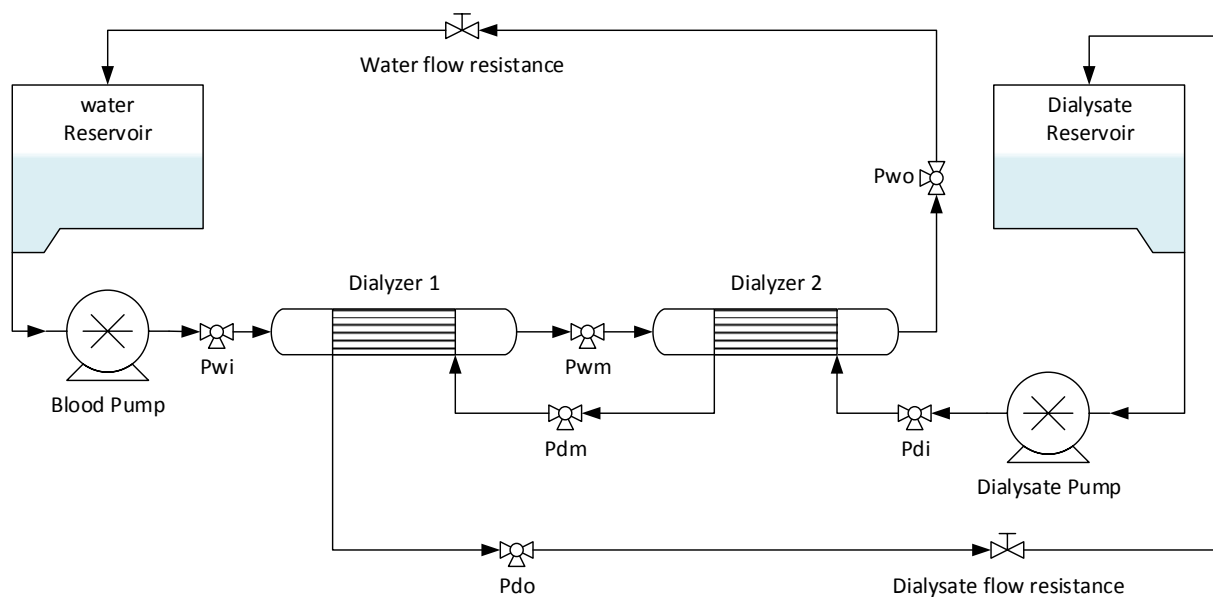
Figure 8.1: schematic representation of the experimental circuit with two dialyzers in serial connection, as used in experiments with distilled water. Pressure sensors are distinguished by the indications Pwi, Pwm, Pwo, Pdi, Pdm and Pdo.

8.1.1.6.2 Circuit for investigations with blood as fluid

Two modules in series circuit should be modify for blood experiments in compare to the circuit used for water, see figure 8.2. The tube connecting the dialysate reservoir directly to the blood reservoir, facilitates the filtrate return to the blood reservoir by means of hydrostatic pressure. Consequently, the net volume flux in both reservoirs remains constant, which means constant hematocrit in the blood reservoir throughout the experimental procedure.
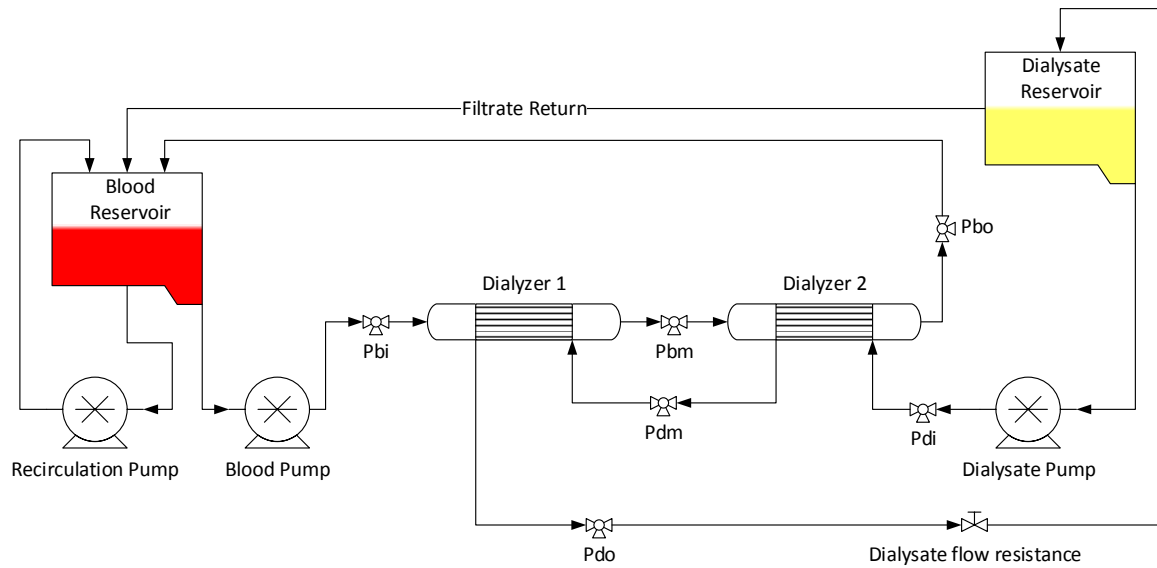
Figure 8.2: Graphical representation of the system built around two dialyzers connected in series. Pressure sensors are distinguished by the indications Pbi, Pbm, Pbo, Pdi, Pdm and Pdo.

8.1.1.7   Hematocrit adjustment

Blood samples are retrieved by means of syringes from the 3-way cocks along the blood compartment (*Pbi*, *Pbm* and *Pbo*). A glass capillary is then filled with the content of each syringe and placed into a specialized centrifuge (Heraeus Haemofuge) that spins with 12,000 rpm for 3 minutes. Upon completion of this phase, plasma in the capillaries is completely separated from the blood cells (sedimentation) and it is now possible to read the hematocrit-value of the sample with the assistance of a linear scale.

Usually the value of hematocrit in the blood reservoir needs to be adjusted, especially when the circuit is initially filled with fresh blood. This is accomplished by either adding some more isotonic solution, or by adjusting of the dialysate reservoir's volume, thus controlling the desired hematocrit-value. It is worth mentioning that the added solution should be isotonic in order to prevent lying the blood cells.

8.1.1.8   Pumps and sensors calibration

The pumps are calibrated for flow rate by means of volumetric measurement. It was carried out in accordance with the volumetric measurement principle, where the yield of the pump is collected in a volumetric cylinder for a defined timespan.

The pressure gauges are set to zero prior to initiation and after the system has been filled up with blood and dialysate for every experiment. A mercury manometer serving as reference is connected to the pressure monitoring device and they are subjected to the same fluid flow (e.g. pressurized air) and will be calibrated.

8.1.1.9   Calculation of UFR

Determining the ultrafiltration rate (UFR), the volume of filtrate that permeates from the capillaries to the surrounding space should be measured indirectly as following. During water investigation, when the experiment starts, time is recorded for every 200 mL decrease of the blood reservoir's level. This procedure is repeated at least three times for each experimental conditions. Ultrafiltration rate is subsequently defined as an average of obtained measurements.

During blood investigations, hematocrit-values are measured in outlet and inlet and ultrafiltration rate is calculated by implementation of mass conservation principle.

Equation 8.4.1 is the continuity equation for the total volume flux balance, whereas Equation 8.4.2 is the continuity equation for plasma flux balance. By substituting the first into the other, Equation 8.4.3 is obtained that yields UFR between the measuring points (e.g. inlet – outlet).

$$\dot{Q}_{Bi} - \dot{Q}_{Bo} - UFR = 0 \qquad \text{(Eq. 8.4.1)}$$

$$\dot{Q}_{Bi}(1 - Hct_i) - \dot{Q}_{Bo}(1 - Hct_o) - UFR = 0 \qquad \text{(Eq. 8.4.2)}$$

$$UFR = \dot{Q}_{Bi}\frac{Hct_o - Hct_i}{Hct_o} \qquad \text{(Eq. 8.4.3)}$$

8.1.2   Results for model validation

In order to validate the models introduced in chapter 7, in vitro investigations results are compared with model predictions.

Water model validation

Figure 8.3 illustrates the relationship between ultrafiltration rate and transmembrane pressure for four different dialyzer models in the water part investigations.
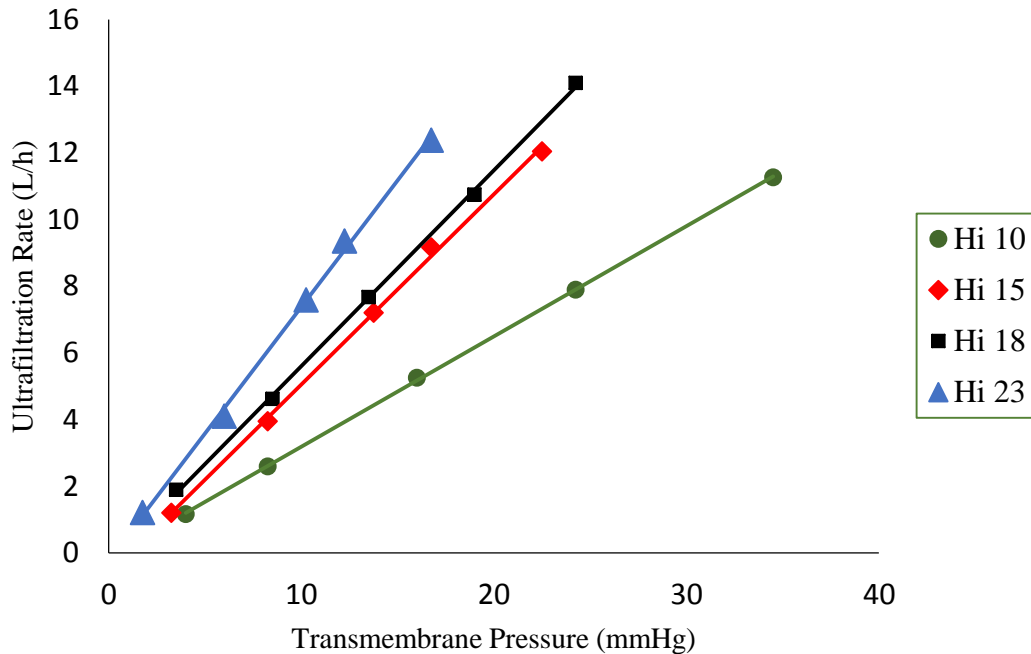
Figure 8.3: UFR as a function of transmembrane pressure. Solid lines represent the model predictions, whereas indicated signs are experimentally measured values obtained from dialyzers with different sizes (Hi 10, 15, 18 and 23).

As it is shown, the prediction by the mathematical model matches almost perfectly with the experimental results obtained from each dialyzer.

Simplified blood model validation

The comparison of measured hematocrit-values fluctuation (indicated signs) and the predicted course by simplified model for different inlet hematocrit-values is shown in Figure 8.4.
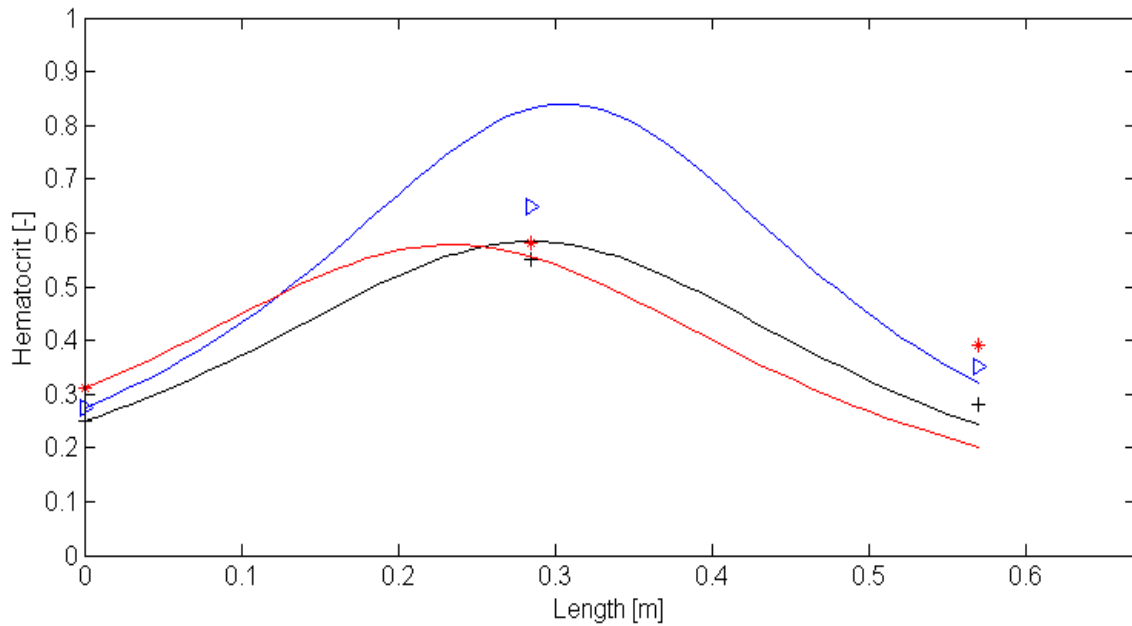
Figure 8.4: The course of hematocrit fluctuation along a fiber's length (realized by two serially connected modules (Hi 18)) as predicted by simplified blood model for three different Hct-values (%): 25(black), 27.5 (blue) and 31(red). The experimental data are measured at inlet, middle and outlet of the module arrangement.

Hematocrit value shows a peak-value around the middle of the module arrangement's length, which actually represent as already mentioned a unique elongated dialyzers, in all three experiments.

Advanced blood model validation

Figure 8.5 represent the course of hematocrit along the fibers of the used configuration for three different inlet hematocrit values. The experimentally obtained data are shown as indicated signs, whereas the corresponding curves, predicted by the advanced model for blood, as solid lines.

Figure 8.5: The course of hematocrit along the fiber's length (realized by two serial connected modules (Hi 18)) as predicted by advanced blood model for three different Hct-values: 25(black), 27.5 (blue) and 31(red). The experimental data are measured at inlet, middle and outlet parts.

Figure 8.6 and 8.7 demonstrate the experimental data (indicated signs) and the model prediction (solid curves) for the course of hematocrit along the length of serially connected dialyzers, at different transmembrane pressure levels, for two different inlet hematocrit values i.e. 25% and 27.5%.
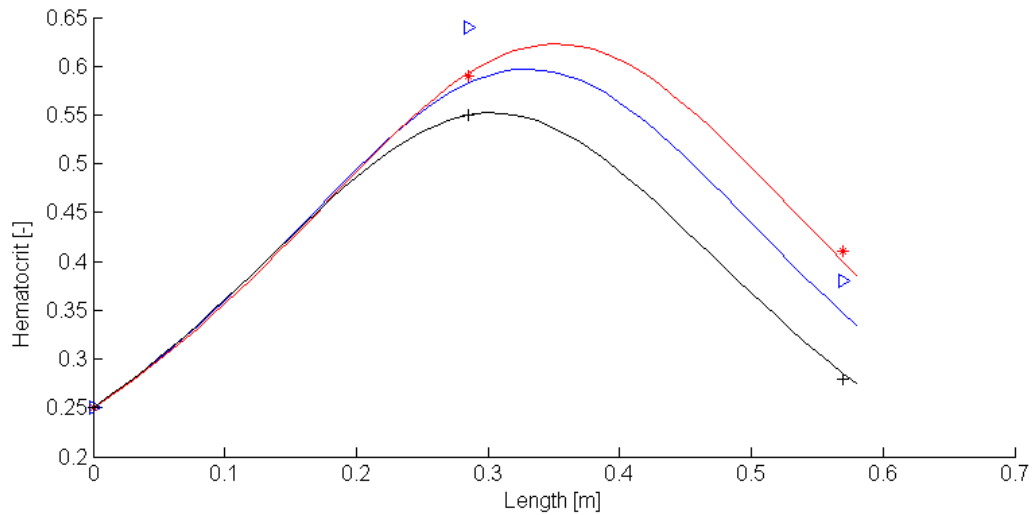
Figure 8.6: The course of hematocrit along a fiber's length (realized by two serial connected modules (Hi 18)) as predicted by advanced blood model for three different TMP levels (Hct$_i$ 25%). The experimental data are measured at inlet, middle and outlet parts.

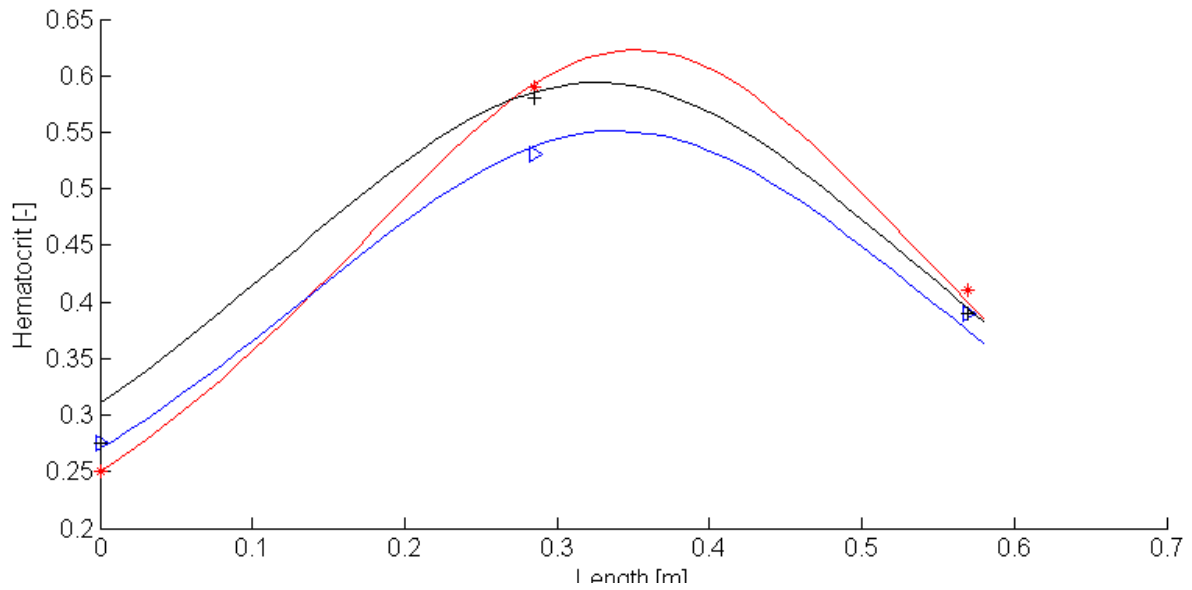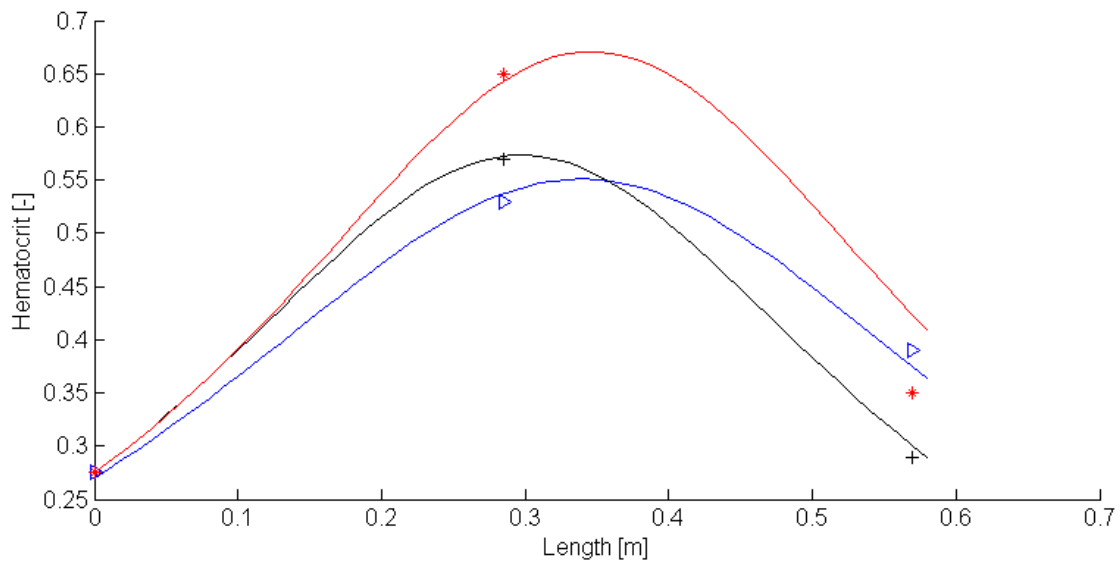*Figure 8.7: The course of hematocrit along a fiber's length (realized by two serial connected modules (Hi 18)) as predicted by advanced blood model for three different TMP levels (Hct$_i$ 27.5%). The experimental data are measured at inlet, middle and outlet parts.*

Figure 8.8 shows the predicted pressure drop along the length of already mentioned two serially connected dialyzers for blood and dialysate fluid.
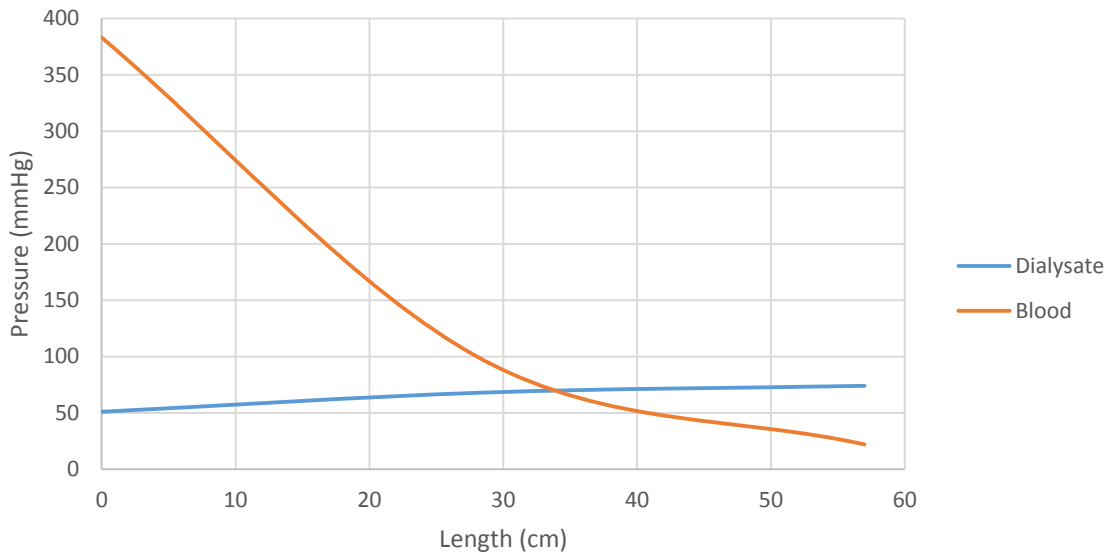
Figure 8.8: Pressure drop of blood and dialysate occurring along the length of two in serially connected arrangement (Hi 18) as predicted by advanced blood model.

Figure 8.9 demonstrates the blood flow rate along the length of the two-dialyzers arrangement at three inlet hematocrit values (%) (25, 27 & 31). Higher *Hct.* results in lower blood flow rate.
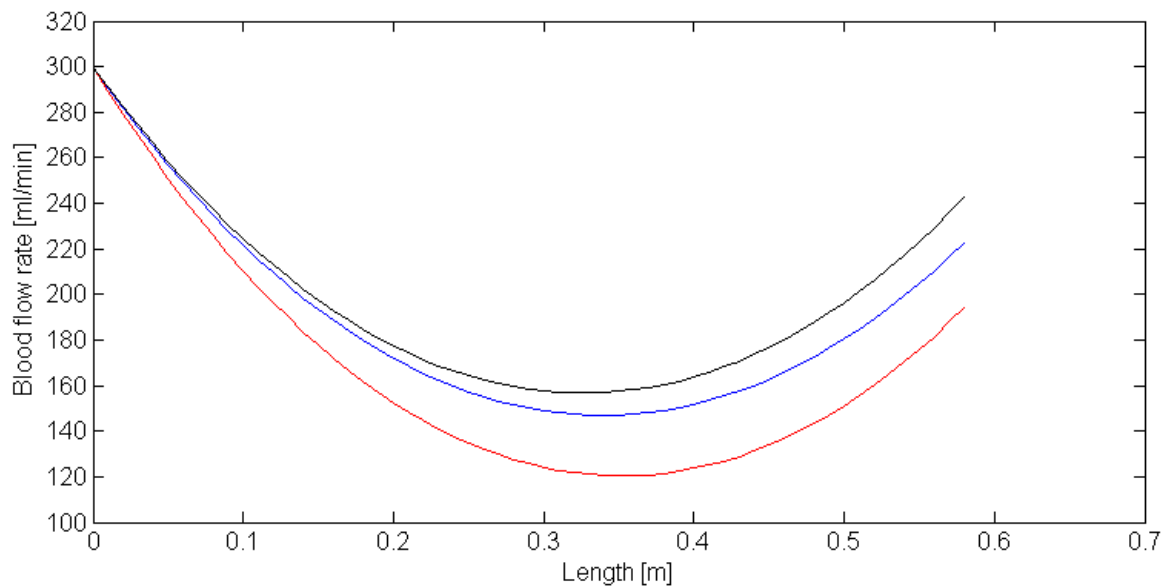
Figure 8.9: Representation of the blood flow rate along the length of two in serial connected arrangement, predicted by advanced blood model for three different inlet hematocrit levels (25(black), 27.5 (blue) and 31(red)).

The results which are in a very good agreement with the theoretical prediction which justify their application as it is demonstrated in figure 8.8 and 8.9.

8.2   Part 2: Direct hematocrit sampling out of capillaries

The second experimental system used as a supplementary validation method for the mathematical models introduced in Chapter 7. The main feature of present validation case is direct sampling the blood out of capillaries at different location and measuring the actual hematocrit-value.

8.2.1   Materials and methods

Most components named in this section, are identical to those implemented in section 8.1. Only those which are not yet introduced, will be described below.

8.2.1.1   Working fluids preparation

Fresh porcine blood (approx. 4-5 liters per experiment) is obtained from slaughterhouse and anticoagulated with heparin (10 units/ml blood), while isotonic solution is (NaCl 0.9%) used as dialysate liquid as well as for blood dilution for hematocrit adjustment.

8.2.1.2   Dialyzers

The hemodialysis circuit here designed utilizes one Kawasumi high flux dialyzer (RENAK PS-1800 H) with a surface area of (1.8 m^2), kindly provided by Meise GmbH, Schalksmühle, Germany. The module is mounted on the circuit and it is operated in the conventional way, until after a given period the circulation of the working media stops, and the dialyzer is dismounted. Its shell is then taken apart carefully in such way that not damaging the fiber bundle. Small bundles of capillaries are selected and cut out for determining their local hematocrit-value.

8.2.1.3   Circuit components and monitoring system

The same pumps and pressure monitoring device as described in section 8.1, were used. Four sensors were applied on a single module (one for each dialyzer port). Monitoring the pressure, controlling the resistance and UFR was performed as also described in section 8.1.

8.2.1.4   Experimental circuit

A typical in-vitro hemodialysis circuit is constructed for this investigations. The filtrate return arrangement has been used in according to section 8.1.1.6.2, in order to maintain a constant hematocrit value in the blood reservoir (Figure 8.10).
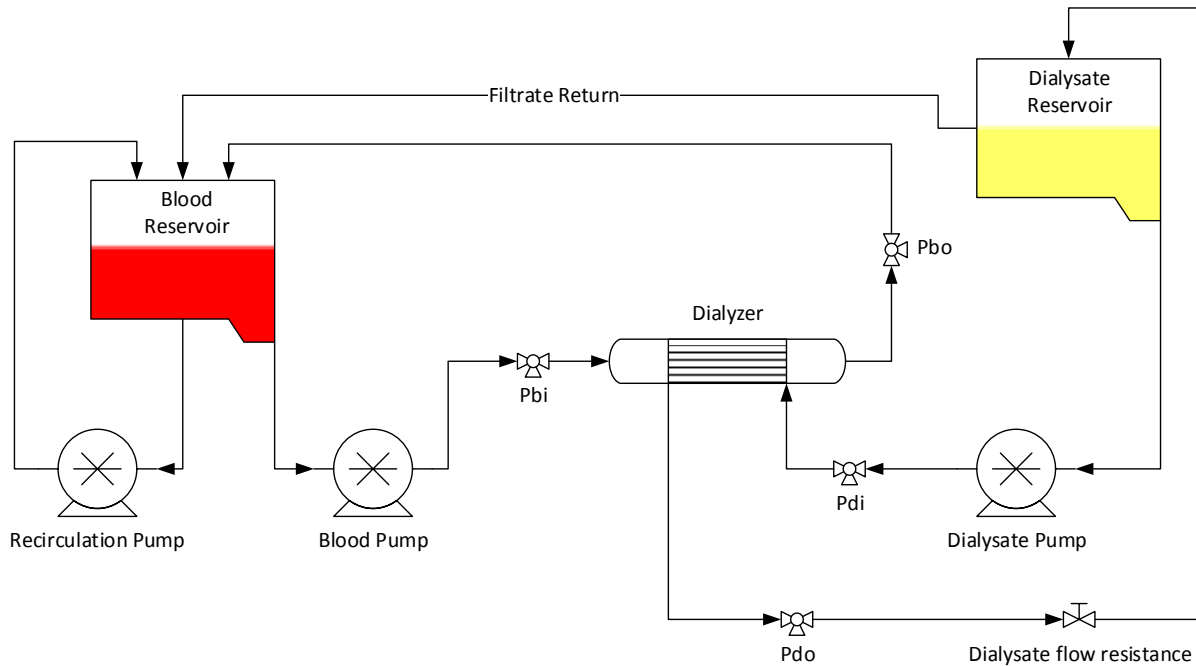
Figure 8.10: Illustration of a regular hemodialysis circuit with a single dialyzer module. Pressure sensors can be distinguished by the indications Pbi, Pbo, Pdi and Pdo.

8.2.1.5   Extraction of blood samples for hematocrit evaluation

Prior to the hemodialysis process, hematocrit is measured by the conventional method already described in the section 8.1.1.7. After the adjustment of the operational parameters (TMP, Hct_i), the pumps are stopped, the dialyzer is isolated from the rest of the circuit (clamping blood inlet and outlet tubes) and the dialysate liquid is drained.

Further, the dialyzer's shell is carefully cut and removed, in order to having access to the bundle of fibers. Subsequently, 20 fibers are selected from the periphery of the bundle and cut near the glued ends of the dialyzer i.e. potting regions. Two segments of 15 mm are cut from the ends of these fibers, one from the middle, and two in between ($x_1 = 25\%$ and $x_2 = 75\%$ of the length).

Each of these 5 segments consisting of 20 identical fiber slices, is then immersed in a vial containing 1000 μL of non-isotonic solution, where it is subjected to thorough stir, in order to lyse all the erythrocytes in the fiber segments and release their hemoglobin content in the surrounding liquid. After twenty minutes, hemoglobin concentration is measured by a spectrophotometer, following the procedure already described in Chapter 5.

In order to corroborate the uniformity of the hematocrit, this procedure is repeated for two more bundles of 20 hollow fibers each; one obtained from the central region of the dialyzer bundle, and another one from a region of intermediate radius (r ≈ 0.5 R).

The hematocrit evaluation was performed by means of a calibration curve, achieved by the correlation of the hemoglobin concentrations measured photometrically with the hematocrit values at the dialyzer's inlet and outlet. These samples were taken before the dialyzer was cut off the circuit. The calibration curve is used to convert the measured hemoglobin concentrations to the targeted hematocrit-values (Figure 8.11). The effect of dilution is considered in the numerical conversion.
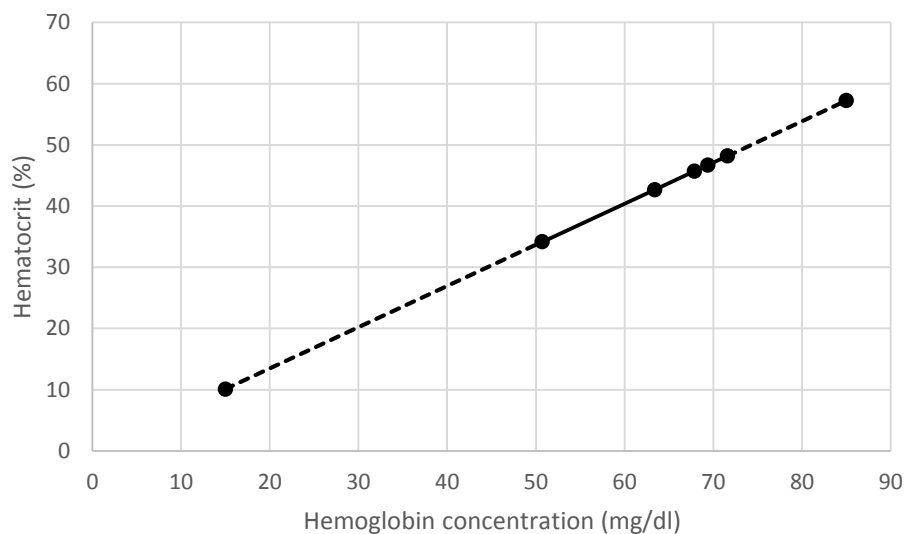
Figure 8.11: Calibrated relationship between hemoglobin concentration and hematocrit value of the blood samples.

8.2.2   Results

The new technique introduced in this section allows a measurable prove of the local hematocrit distribution along the fibers.

To apply the calibration curve, it is very important to make sure that all the cells using this non-isotonic solution have been destroyed and washed and whole of the contained hemoglobin of the cells is released into the surrounding solution. To prove that, several electron microscopy (SEM) pictures are taken from the inner side of the sampled hollow fibers before and after immersing into the non-isotonic solution. Figure 8.12 compares the inner side of hollow fibers before and after washing with non-isotonic solution.
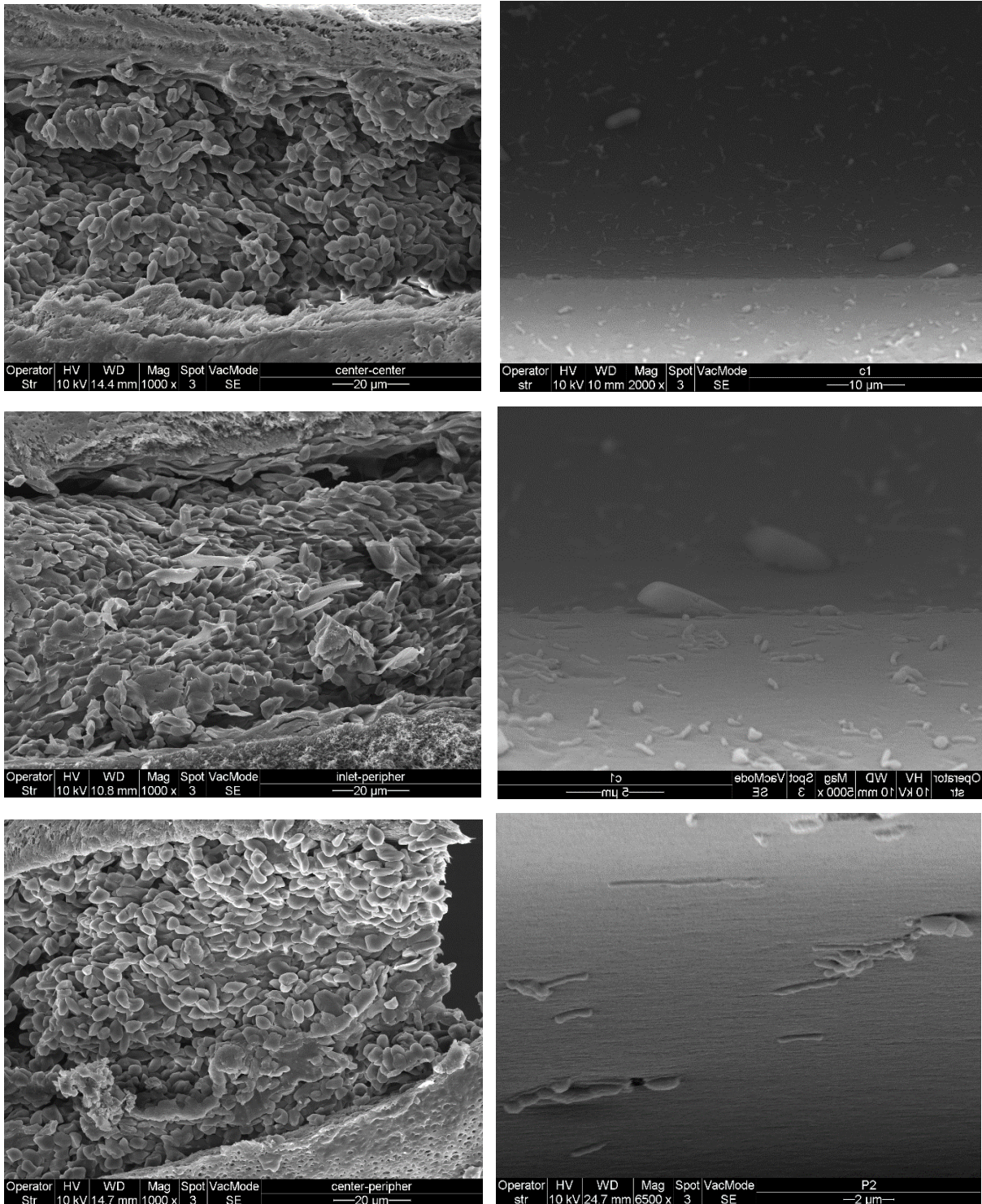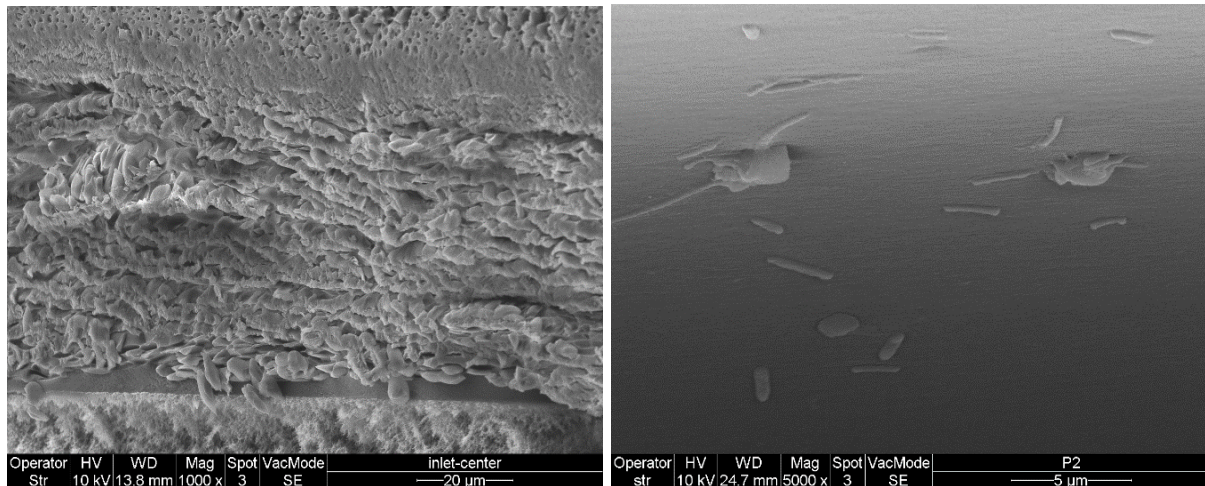
Figure 8.12: The inner surface of hollow fibers of the tested dialyzer before (left pictures) and after (right pictures) washing with non-isotonic solution. Electron microscopic photographs, department of pathology, University Hospital RWTH Aachen.

As it is obvious in this photographs, the red blood cell membranes are destroyed and therefore whole of their hemoglobin content must be released into the non-isotonic solution. Therefore, the measured hemoglobin concentration reliably can reflect the hematocrit-value.

In order to control and simulate clinical application, the filtration rate was controlled by increasing of resistance in dialysate and blood compartments inflow. This was achieved simply by using a clamp in the dialysate/blood outlet. The experimental results of these conditions are shown in Figure 8.14.

The diagram in Figure 8.13 depicts the course of in the mentioned way measured hematocrit-values along the dialyzer's length, experimental data are calculated as an average of the individual hematocrit measurements obtained from 60 fibers. From these, 20 are located centrally, another 20 from the periphery of the bundle, and the remaining from an intermediate radius. These values are compared with the calculated course predicted by advanced blood model equation for hematocrit values (see chapter 7).

Figure 8.14 shows the course of hematocrit-value along the fibers' length by sampling from different part of the module, i.e. central, peripheral and in-between. These measured values are compared with the predicted values by advanced blood model (solid lines). As boundary condition, the measured initial values are inserted in the model.
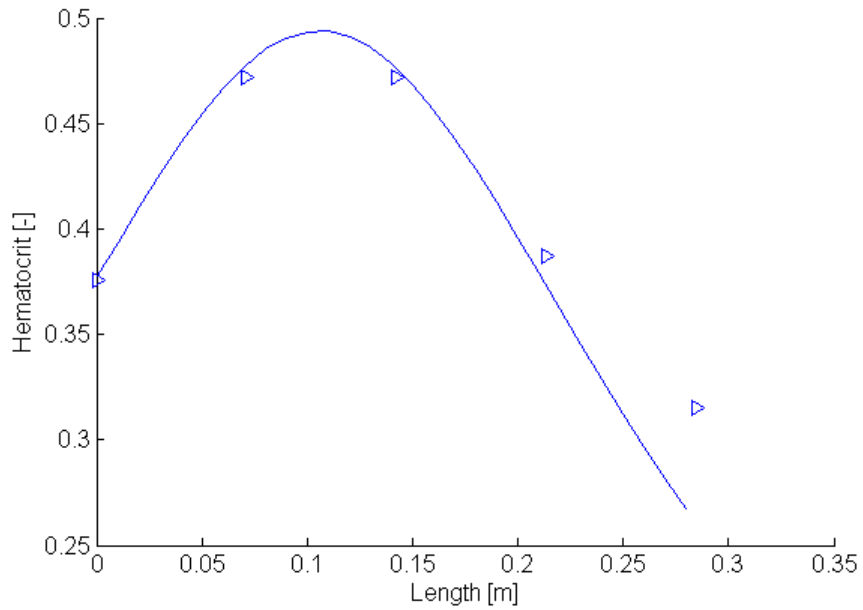
Figure 8.13: The course of average hematocrit-value as predicted by advanced model. The calculated data are inserted as (▷).
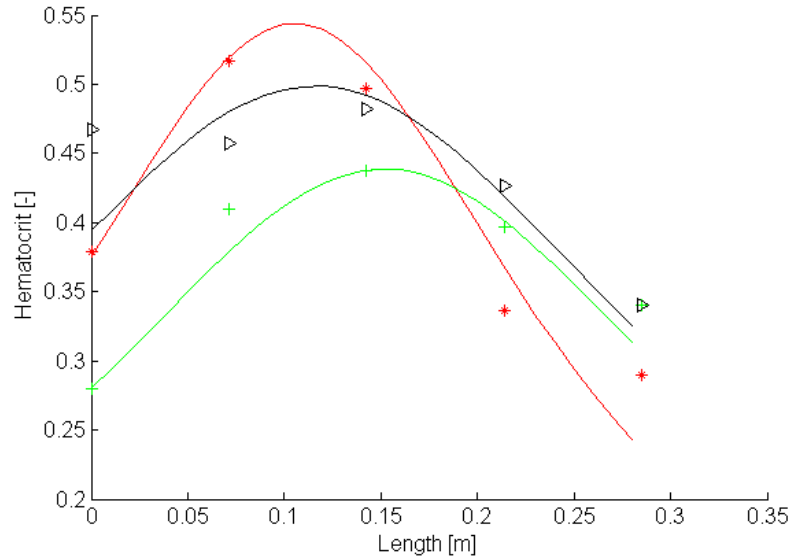
Figure 8.14: The course of hematocrit-value along the fibers' length sampled from different part of the module: central (black), peripheral (green) and intermediate (red). Indicated signs: Experimental data. Curves: Model predictions.

The produced hemolysis in a dialyzer due to cell distribution is given as an example in Figure 8.15. This figure clearly show a significant increase in hemolysis level by increasing the

hematocrit from 30 to 40 %. The produced hemolysis generated by the system itself (circuit without dialyzer) is deducted in order to demonstrate only the hemolysis part of the dialyzer itself.
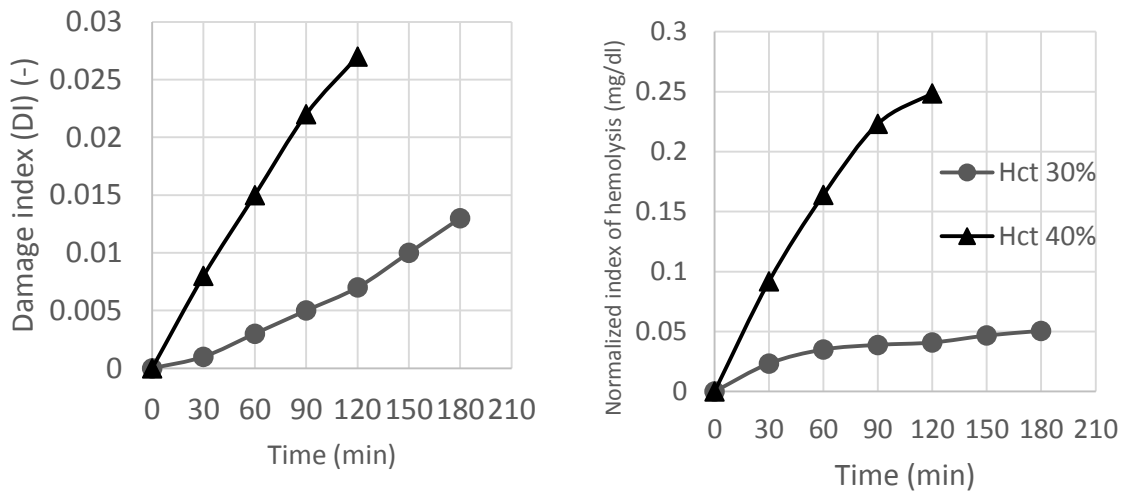
Figure 8.15: Effect of the initial inlet hematocrit-value upon the resulted hemolysis calculated as damage index(DI, left) and normalized index of hemolysis (NIH, right) in a dialyzer (RENAK PS-1800 H).

8.3   Discussion

In this chapter, the introduced models described in chapter 7 are experimentally proved and as it was described viable results could be obtained. The essential of these experimental circuits is shown in Figure 8.1 and 8.2 in combination with table 8.1.

As shown in Figure 8.3, the linearity of the data due to Newtonian behavior of water as working medium is confirmed. The nearly perfect agreement between model predictions and experimental results, proves that the model's parameters were well defined and all assumptions were close to the "reality".

The calculated courses of hematocrit according to the predictions made by the simplified model show rather poor agreement to the experimental results as Figure 8.4 indicates. This can be attributed to the assumptions made in the model particularly for oncotic pressure, which was considered to be a constant value. This was adopted to the literature reports with the frequently used assumption of a constant oncotic pressure, while in fact the results here demonstrate its

high dependency on hematocrit and therefore should not be regarded as a constant parameter and explains the high discrepancy between experimental data and model estimations.

The advanced model equation for blood based on Landis theoretical approach (chapter 7), which considers the effect on oncotic pressure, yields more consistent estimations which are much closer to the experimental data as shown in Figure 8.65, 8.6 and Figure 8.7. However, there are still some small deviations below 10% presumably originate from the modification of Landis equation in order to achieve the analytical solution.

Figure 8.8 and Figure 8.9 prove that this model can be implemented in the estimation of main parameters during a hemodialysis study, including local hematocrit-value, blood and filtrate flow rate, blood and dialysate pressure (Hct_i, P_b, P_d, Q_b, and Q_f). These approach provides a better understanding and simulation of true clinical features in case of filtration and backfiltration procedures, as well as their impact on Hematocrit and blood shearing. The substantial pressure drop is anticipated in Figure 8.8, demonstrates the impact of the length of a dialyzer leading to significant increase of flow resistance (according to the Hagen-Poiseuille equation). The non-linear character of the curve is due to interaction of involving parameters which are related in a rather complex manner such as TMP, Hct, UFR, blood viscosity and shear rate. Therefore, a linear approximation would be too far beyond the reality.

The presented validation procedure in part 2 of this chapter is based on measuring of the hemoglobin concentration of the erythrocytes which is correlating to hematocrit value. The probes are taken from different parts of blood compartment i.e. the blood containing inside the hollow fibers. In contrast to the presented approach here using directly red blood cells, the earlier proposals to apply Scintigraphic methods as reported by Ronco, Fiore et al. [135, 136] are indirect methods and therefore do not provide the required precise as result in order to consider the potential of convective solute transport in connection with ultrafiltration for blood purification.

As already mentioned the variation of hematocrit and its impact in physiological blood circulation and organ perfusion [17, 107] should be also considered in the case of artificial organs. Its important influence in connection with rotary blood pumps is already described in chapter 5. In the case of dialyzers, this phenomenon plays also an important role, however with lower shear and blood flow rates. The already shown fluctuation of hematocrit in different applications of dialyzers/hemofiltration affects the ultrafiltration rate and has an important

contribution to control the physiological hematocrit-value of the patients undergoing this kind of treatments. It is a phenomenon which was already reported in 1969 by Ivanovich et al [58]. For instance in Figure 8.13 one can observes a remarkable peak of hematocrit right after the inlet. This peak can be shifted by the increasing of flow resistance on the dialysate outlet conduit that leads to an artificial drop of TMP. The higher the induced resistance, the closer the peak of hematocrit value toward the inlet of hemofilter device. This shift is also responsible for the domination of backfiltration in the approx. 2/3 of the dialyzer's length, which has as a consequence of the drop of hematocrit at the outlet even below the inlet value. The agreement between the experimental data and the prediction of the advanced calculation model show the applicability of this method.

Figure 8.14 demonstrates if unequal values of hematocrit at the inlet of the fibers occur, the red blood cells distribution is non-uniform in the radial direction of the fiber bundle. As this figure shows, the fibers in the central region possess blood with higher hematocrit-value than those in peripheral ones. This fact leads also to a non-uniform filtration and also variation of the hematocrit during the blood passage along the length of fiber bundle as it is clearly shown in this figure. This result demonstrates for all regions, i.e. central, peripheral and intermediate a good agreement with the presented prediction model.

As Figure 8.15 shows in comparison to the rotary blood pumps, hemolysis values given as DI and NIH are lower. It is because of establishing much lower shear rates i.e. about 80 s^{-1} in the dialyzer corresponding to a value of 0.24 Pa which below 1 Pa. However, the significant rise of hemolysis for higher initial inlet hematocrit shows the importance of established local hematocrits on resulted hemolysis.

8.4   Conclusion

The water model validated in the serially connected dialyzers set, appears to be a well-defined model and its predictions match nearly perfectly to the obtained experimental results. Since in the case of water, no diffusion of solutes occurs, it is an ideal fluid for estimation of the filtration rate and the pressure drop establishing in hemodialyzer/filtration devices.

On the other hand, the simplified model for blood showed less accuracy because of the neglecting of the important influence of the oncotic pressure.

The advanced blood model however enable us to take the advantage of a much more accurate results by considering the oncotic pressure. Despite some approximation that has to be made in order to be able to have an analytically solution, its predictions for hematocrit course along the device has a very good agreement with the experimental data.

Furthermore the advanced blood model can successfully predict also other significant parameters of hemodialysis process such as P_b, P_d, Q_b, and Q_f, and thus provides a good overview of the hemodynamics in a dialyzer/filtration systems. As an important application, if hematocrit predictions are combined with the calculated local shear stress and viscosity, it can be used also for produced hemolysis rate and final hematocrit values estimation for clinical usage. As Figure 8.15 demonstrates the effect of produced hemolysis rate in the case of dialyzers is affected by its duration rather than the strength of the shear stress. It is in contrast to the results obtained for rotary blood pumps i.e. high shear stresses and low exposure time reported in chapter 5 and 6. However, the resulted hemolysis rate is strongly depended on the established local hematocrit.

Finally, it can be concluded that the prolongation of dialyzer length is a useful tool to achieve experiments with longer dialyzers by connecting smaller devices in serial mode.

The approach of extraction of blood samples for hematocrit evaluation, as a new method here, was shown to evidence the exact course of hematocrit fluctuation and serves as a further proof of the applicability of the advanced blood model for prediction of hematocrit in a dialyzer.

Chapter 9

Dialyzer circuit with inverse blood/dialysate compartments

9.1   Introduction

The aim of this approach is to try to prove another alternative for investigations on the influence of the red cells distribution in the case of artificial kidney. In this approach we changed the dialysate fluid compartments. I.e. the dialysate flows inside the fibers and the blood outside of the hollow fibers inside the shell housing. It should be noted that this approach is also used in the case of membrane capillary lung (membrane oxygenators). The adjustment of the flow directions requires certain modifications in the advanced model for blood described in the next section.

9.2   Materials and Methods

The majority of the materials used in this experimental variation are same to those used in the chapter 8. Therefore, only those which are not yet presented, will be described here. In this chapter, similar to the second validation method (8.2), the experiments are carried out with blood.

9.2.1   Modification of the advanced blood model for inverse flows

In the case of inverse flows in the dialysis circuit, a modified model for predicting the hemodynamic characteristics of blood would be required which has some differences from one introduced in chapter 7.

9.2.1.1   Theoretical backgrounds

9.2.1.1.1 Blood pressure

Pressure in dialysate compartment, in which for this case blood is flowing through, declines linearly:

$$P_b\left(l\right) = \frac{P_{bo} - P_{bi}}{L}\, l +\, P_{bi} \qquad \text{(Eq. 9.4.1)}$$

9.2.1.1.2 Shear rate

Shear rate inside the hollow fibers demonstrates a non-linear behavior, therefore the average shear rate in a pipe based on Severs and Austin [54] is considered as stated below:

$$\dot{\gamma} = \frac{8\,V}{D} = \frac{4\,Q}{\pi\,R^3}$$
(Eq. 9.4.2)

9.2.1.1.3 Viscosity

Viscosity of dialysate is given as constant approximately equal to the value of the water, because of its Newtonian behavior. The viscosity of blood is described as a power law equation according to Rosentrater et al. equation [131] for porcine blood.

$$\mu = k\,\dot{\gamma}^{n-1}$$
(Eq. 9.4.3)

As already introduced in the corresponding segment of Chapter 7 for the advanced blood model, viscosity is represented by equation 7.5.1, and can be correlated with hematocrit as following:

$$\mu(l) = 163\,\frac{c_6^2}{Q_b(l)^2} - 28.7\,\frac{c_6}{Q_b(l)} + 3.9$$
(Eq. 9.4.4)

$$\mu(l) = 163\,Hct^2 - 28.7\,Hct + 3.9$$
(Eq. 9.4.5)

9.2.1.1.4 Oncotic pressure

Oncotic pressure is considered to be a function of protein concentration in blood plasma. The relationship between pressure and protein concentration were approximated by the Landis and Pappenheimer equation [134] (see assumptions taken for advanced blood model in chapter 7). By applying the same approach, the relationship between oncotic pressure and hematocrit can be correlated as:

$$\pi\,(Hct(l)) = \frac{-984}{Hct(l)} + 5320$$
(Eq. 9.4.6)

9.2.1.1.5 Flow distribution

Flow distribution varies between peripheral and central fibers can be considered nearly uniform. A homogenous flow distribution (Q) for dialysate therefore becomes:

$$Q = N. \; Q_i^{fiber} \tag{Eq. 9.4.7}$$

And for mass transfer coefficient it is simplified here as:

$$K = N. \, K^{fiber} \tag{Eq. 9.4.8}$$

Where N is the number of fibers, and Q_i^{fiber} is inlet flow rate in each fiber.

9.2.1.2 Model formulation

Ultrafiltration rate of a single capillary can be estimated according to Fick's law:

$$dQ_f = K^{fiber} \; dA^{fiber} \; \Delta P_{tm} \tag{Eq. 9.4.9}$$

Which for the dialyzer module as a whole it will become:

$$dQ_f = K \; dA \; \Delta P_{tm}$$

$$dQ_f = K \; (2\pi R \; dl) \left(P_b(l) - P_d(l) - \pi(l) \right) \tag{Eq. 9.4.10}$$

Integration of Equation 9.4.10 over length and substitution of blood and oncotic pressure equations yields:

$$Q_f(l) = (2\pi R K) \left(\int_0^l P_b(l) \; dl - \int_0^l P_d(l) \; dl - \int_0^l \pi(l) \; dl \right) \tag{Eq. 9.4.11}$$

$$Q_f(l) = c_8 \left[\left[\int_0^l -P_d(l) \; dl - \int_0^l \left(\frac{-984}{c_6} \left((Q_{bi} + Q_{di}) - Q_d \right) + 5320 \right) dl + c_9 l^2 + P_{bi} \; l \right] \tag{Eq. 9.4.12}$$

Where $c_8 = 2\pi R K$, $c_9 = \frac{P_{bo} - P_{bi}}{2L}$. It is known:

$$Q_d(l) = Q_{di} + Q_f(l) \tag{Eq. 9.4.13}$$

$$Q_d(l) = Q_{di} + c_8 \left[\int_0^l -P_d(l) \; dl - \int_0^l \left(\frac{-984}{c_6} \left((Q_{bi} + Q_{di}) - Q_d \right) + 5320 \right) dl + c_9 l^2 + \right.$$
$$\left. P_{bi} \; l \right] \tag{Eq. 9.4.14}$$

On the other hand:

$$\Delta P_d = P_{di} - P_d(l) = \int_0^l dP_d \tag{Eq. 9.4.15}$$

Hollow fibers can be regarded as cylindrical pipes, and the flow in them is laminar, therefore Hagen–Poiseuille equation [6] can be employed for ΔP estimation:

$$\Delta P_d = {8\,\mu\,l\,Q^{fiber}}\Big/{\pi R^4}$$

(Eq. 9.4.16)

And here by substitution:

$$\Delta P_d = P_{di} - P_d(l) = \frac{8\,\mu\,(l)}{\pi NR^4} \int_0^l Q_d(l)dl$$

(Eq. 9.4.17)

Equation 9.4.14 can be rewritten using $P_d(l)$ from the derivative of Equation 9.4.17:

$$\acute{Q}_d(l) = c_8 \left[-P_d(l) + 2c_9 l + P_{bi} + \frac{984}{c_6}\left((Q_{bi} + Q_{di}) - Q_d\right) - 5320 \right]$$

(Eq. 9.4.18)

$$P_d(l) = \frac{-\acute{Q}_d(l)}{c_8} + 2c_9 l + P_{bi} + \frac{984}{c_6}\left((Q_{bi} + Q_{di}) - Q_d\right) - 5320$$

(Eq. 9.4.19)

Substitution of $P_d(l)$ from Equation 9.4.19 into Equation 9.4.17:

$$P_{bi} + \frac{\acute{Q}_d(l)}{c_8} - 2c_9 l - P_{bi} - \frac{984}{c_6}\left((Q_{bi} + Q_{di}) - Q_d\right) + 5320 = \frac{8\,\mu\,(l)}{\pi NR^4}\int_0^l Q_d(l)dl$$

(Eq. 9.4.20)

From the derivative of Equation 9.4.20 over length, it is obtained:

$$\frac{\acute{\acute{Q}}_d(l)}{c_8} - 2c_9 + \frac{984}{c_6} Q_d(l) = \frac{8\,\mu\,(l)Q_d(l)}{\pi NR^4}$$

(Eq. 9.4.21)

Which can be rewritten as:

$$\acute{\acute{Q}}_d(l) = c_{12}\, Q_d(l) + c_{13}$$

(Eq. 9.4.22)

Where
$$c_{12} = \frac{8\,\mu\,(l)}{\pi NR^4} - \frac{984}{c_6}\,, \qquad c_{13} = 2\,c_8\,c_9$$

Equation 9.4.22 is a second order non-linear ordinary differential equation. Solving this will yield $Q_d(l)$. A subsequent substitution of $Q_d(l)$ into Equation 9.4.19, will provide us with $P_d(l)$. Finally $Hct(l)$ can be obtained by substituting $Q_d(l)$ into Equation 7.5.6.

$$Q_d(l) = \frac{c_{13}}{c_{12}} + c_{14}e^{\sqrt{c_{12}}\,l} + c_{15}e^{-\sqrt{c_{12}}\,l} + c_{16}$$

(Eq. 9.4.23)

Where c_{14}, c_{15} and c_{16} are the integration constants.

Thusly, the derivative of $Q_d(l)$ will be:

$$\acute{Q}_d(l) = c_{14}\sqrt{c_{12}}\, e^{\sqrt{c_{12}}\, l} - c_{15}\sqrt{c_{12}}\, e^{-\sqrt{c_{12}}\, l} \tag{Eq. 9.4.24}$$

Substitution $\acute{Q}_b(l)$ into Equation 9.4.19 and the necessary simplifications lead to the following equation:

$$P_b(l) = -c_{14}\left(\frac{\sqrt{c_{12}}}{c_8} + \frac{984}{c_6}\right)e^{\sqrt{c_{12}}\, l} + c_{15}\left(\frac{\sqrt{c_{12}}}{c_8} - \frac{984}{c_6}\right)e^{-\sqrt{c_{12}}\, l}$$
$$+ 2c_9 l + P_{bi} + \frac{984}{c_6}\left((Q_{bi} + Q_{di}) - \frac{c_{13}}{c_{12}}\right) - 5320 \tag{Eq. 9.4.25}$$

Application of the boundary conditions for pressure: $P_d(0) = P_{di}$, $\quad P_d(L) = P_{do}$ grants us the values of the following constants:

$$c_{14} = 10^{-8} * (0.041 * TMP - 52.3)$$

$$c_{15} = 10^{-8} * (0.1356 * TMP - 37.1)$$

$$c_{16} = Q_{bi} - c_{14} - c_{15} - \frac{c_{13}}{c_{12}}$$

Application of the boundary condition for flow rate: $Q_d(0) = Q_{di}$:

$$Q_d(l) = c_{14}e^{\sqrt{c_{12}}\, l} + c_{15}e^{-\sqrt{c_{12}}\, l} + Q_{bi} - c_{14} - c_{15} \tag{Eq. 9.4.26}$$

Hence:

$$Q_f(l) = c_{14}e^{\sqrt{c_{12}}\, l} + c_{15}e^{-\sqrt{c_{12}}\, l} - c_{14} - c_{15} \tag{Eq. 9.4.27}$$

$$UFR = Q_f(L) = c_{14}e^{\sqrt{c_{12}}\, L} + c_{15}e^{-\sqrt{c_{12}}\, L} - c_{14} - c_{15} \tag{Eq. 9.4.28}$$

$$Hct\,(l) = \frac{Q_{di}\,Hct_i}{Q_d(l)} = \frac{c_6}{Q_d(l)} = \frac{c_6}{Q_{di} - c_{14}e^{\sqrt{c_{12}}\, l} - c_{15}e^{-\sqrt{c_{12}}\, l} + c_{14} + c_{15}}$$
$$\tag{Eq. 9.4.29}$$

9.2.2 Dialyzer

A Kawasumi high flux dialyzer (RENAK PS-1800 H) is modified for this investigation. The dialyzer's shell has been drilled at three evenly spaced positions, and three 3-ways cocks have been installed in the holes, thus providing five sampling sites (including the inlet and outlet ports).

9.2.3 Experimental circuit

In the here constructed hemodialysis circuit, a single dialyzer used in such a way that dialysate flows inside the hollow fibers and the blood in the compartment surrounding the capillary bundle.

Blood sampling is achieved from the inlet and outlet as well as the cocks located on the shell, where the three holes have been drilled (*BS1*, *BS2* and *BS3*) as shown in Figure 9.1. Hence, 5 blood samples can be obtained for each experimental set. Having more sampling sites offers a more accurate insight into the varying hematocrit level along the fibers' length. This system is also featuring a closed loop configuration, in order to provide constant conditions throughout the investigation's period.
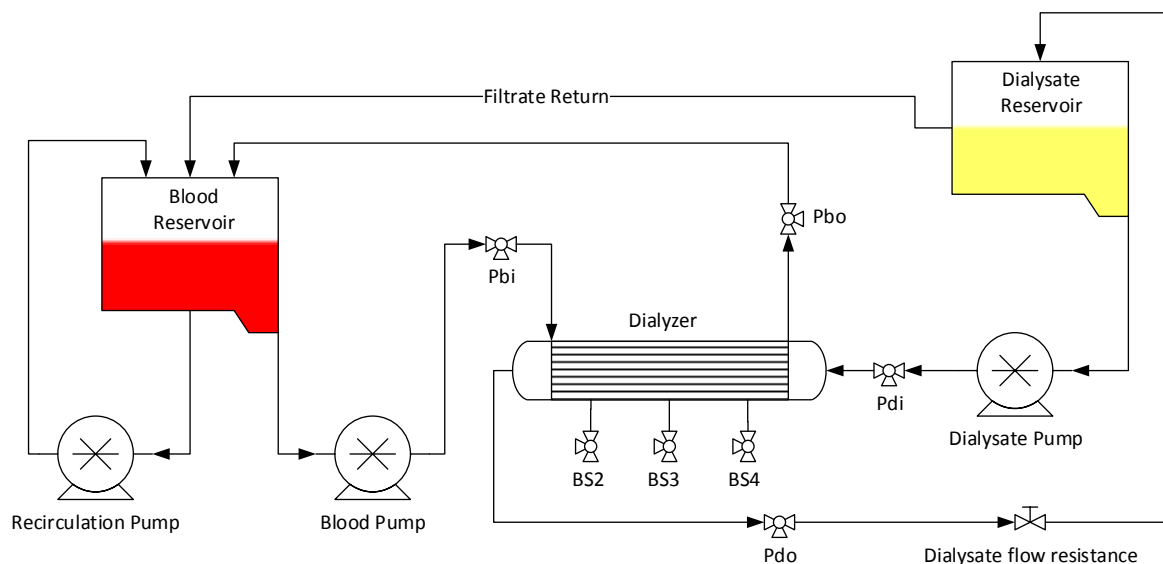
Figure 9.1: Schematic representation of the extracorporeal circuit for a single dialyzer with inverse blood/dialysate flow. Pressure sensors are distinguished by the indications for inlet and outlet as: Pbi, Pbo, Pdi and Pdo. Blood sampling sites: Pbi, BS2, BS3, BS4 and Pbo.

9.2.4   Experimental procedure

Hematocrit measurement and adjustment as well as pump and sensor calibration and UFR measurement methods were achieved similar to those introduced in the Chapter 8 (8.1). For in vitro investigations also here heparinized porcine blood was used.

9.3   Results

Figure 9.2 shows the course of hematocrit-value along the length of a dialyzer in this case outside of the capillaries because of the inversed blood/dialysate flow compartments. Different inlet hematocrit-values (*Hct_i* 36.5, 39, 43 and 55%) are applied. In this figure, the course of curves show the model prediction and the indicated signs the measured values.
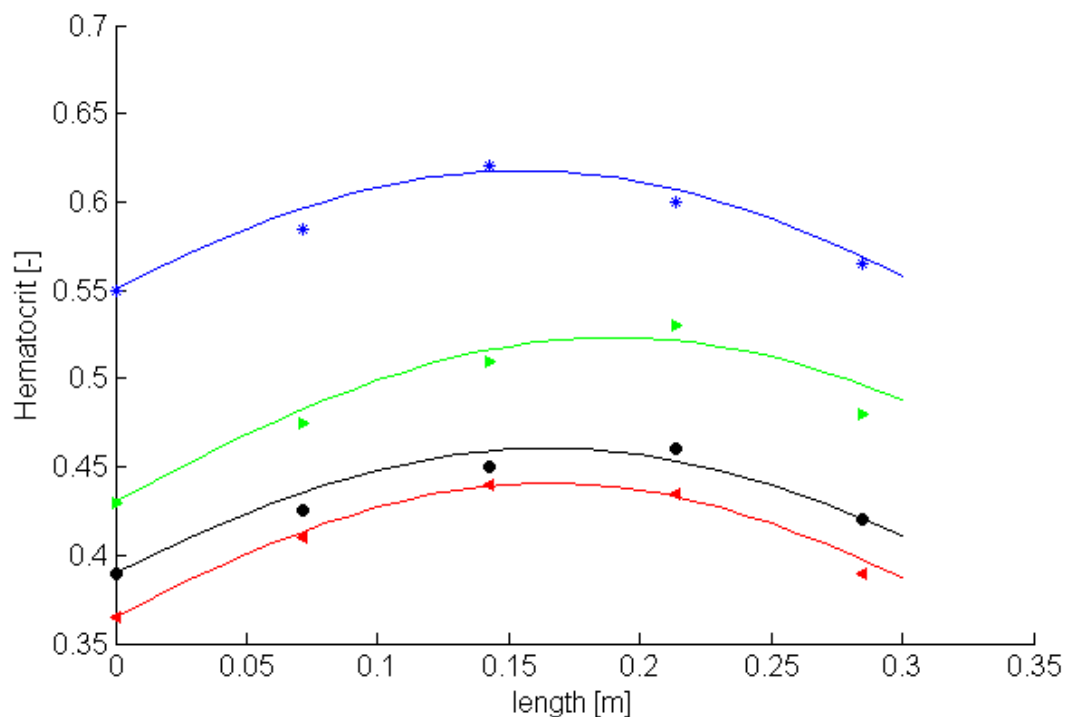
Figure 9.2: The course of hematocrit-value along the length of a dialyzer in the inverse blood/dialysate flow condition with different inlet hematocrit value (Hct_i) (corresponding to the length=0)

The next two figures demonstrate the course of the blood (Figure 9.3) and dialysate (Figure 9.4) flow rates along the dialyzer's length. Due to filtration and backfiltration resulting by pressure differences direction, there are after a minimum value a further increase of flow in the case of blood (Figure 9.3) and decrease of flow after a maximum for the dialysate (Figure 9.4). Therefore, the dialysate flow rate is enhanced by the added filtrate, whereas blood flow experiences the opposing effect. Because of this inversion, filtrate migrates from the "dialysate" compartment to the "blood" compartment, i.e. into the fibers.
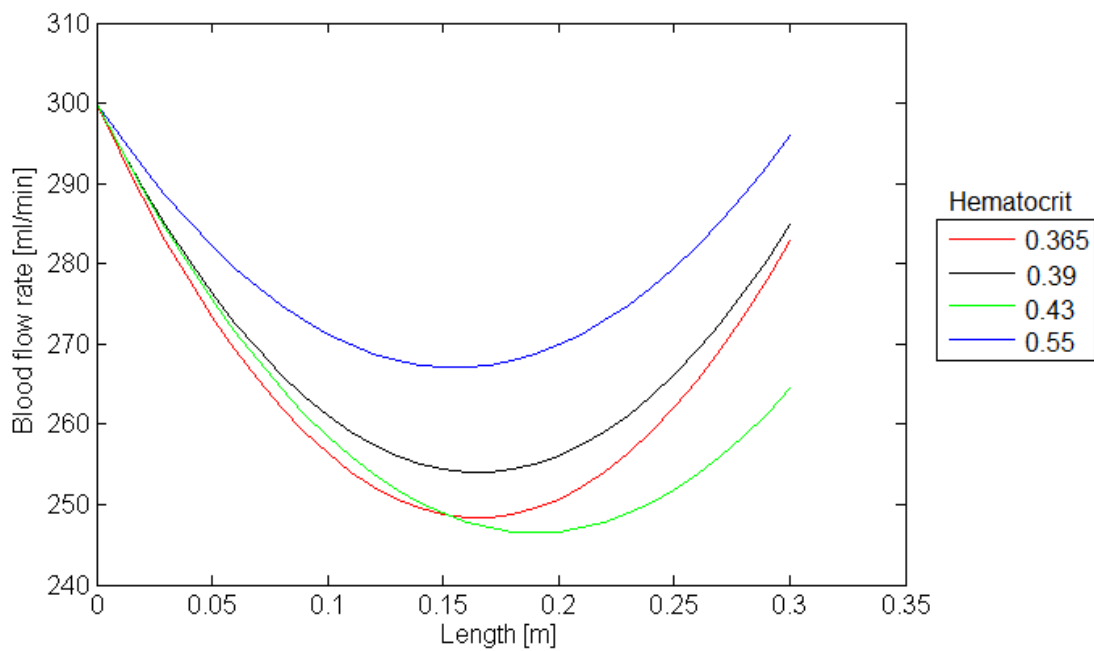
Figure 9.3: The course of the blood flow rate along the fiber length, caused by filtration and backfiltration as predicted by equations 9.4.26 and 9.4.27 in a dialyzer with blood flow outside and dialysate inside of the fibers (for inverse usual flow condition).
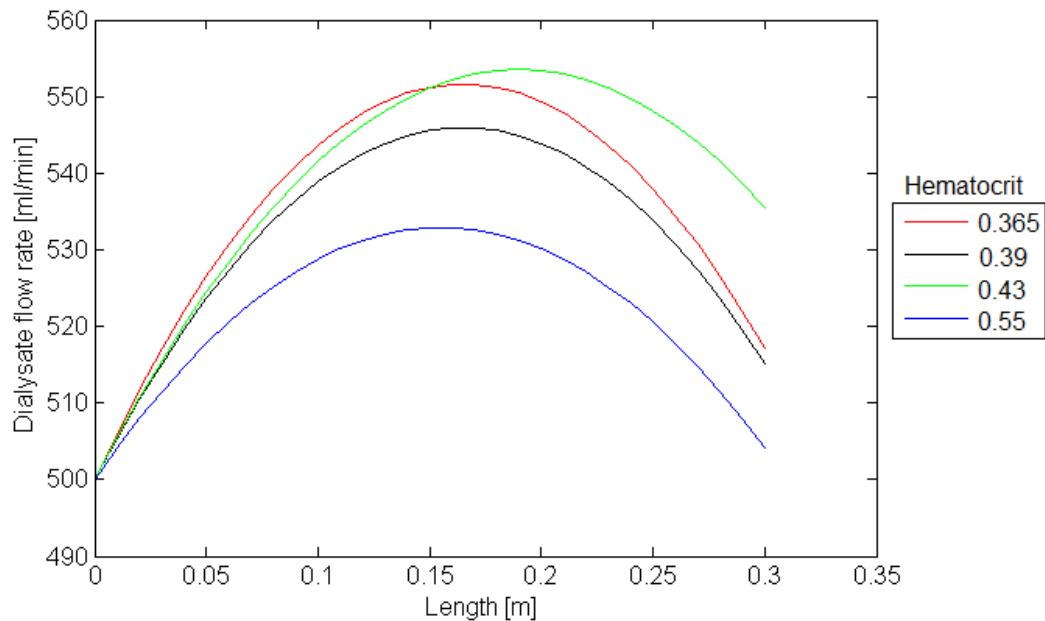
Figure 9.4: The course of the dialysate flow rate along the fiber length, as predicted by equation 9.4.26 (for inversed usual flow condition).

9.4   Discussion

The introduced alternative method in this chapter has the advantage of blood sampling and hematocrit monitoring in different part of the dialyzer along its length. Thus, this method provides more quantity of samples and therefore a better comparison is possible.

The curves in Figure 9.2, shows the course of hematocrit for different inlet hematocrit Values. They show a more flat character in comparison to regular flow systems (see section 8.1). In other words, the   peak at backfiltration point, compared to obtained values from the circuit introduced in section 8.1 is not emphasized i.e. is not much higher than other values. This is the case due to the fact that blood flows outside of the capillaries and therefore produces less transmembrane pressure. However, the existence of the peak shows that hematocrit change does not behave linearly. It is notable to mention that the adequate amount of experimental data obtained from this circuit provide enough data for a better verification of the model. As the plot in Figure 9.3 indicates, the blood flow rate along the length of the dialyzer module decreases significantly (almost up to 20%) under the influence of filtration. Dialysate flow rate exhibits an opposite behavior to the blood, since the discharge from blood plasma liquid accumulates inside the fibers.

9.5   Conclusion

This validation case was specifically carried out in pursuance of achieving an improved hematocrit monitoring regarding the fluctuation of hematocrit during a hemodialysis procedure. Although, the dialyzer's use was entirely reversed, the goal was to obtain blood samples from as many locations along the dialyzer's shell as possible. The advanced mathematical model demonstrates a very good agreement with the experimental data.

In general thought, higher hematocrit at the dialyzer's inlet, triggers an increase in all the hemodynamic characteristics of the flow (TMP, viscosity, shear stress, UFR, hematocrit). In conclusion, after three validation cases, the reliability of the advanced model for blood was further confirmed. It can be also concluded that this inversed flow study might provide for the future new ideas to redesign the classical hemodialysis flow principle, in order to achieve also more efficacy for diffusion of electrolytes and the removal of the toxins.

Chapter 10

Overview and outcomes

10.1 Concluding remarks

The primary objective of the presented study is to determine the significance of shear induced cell distribution and its consequences on hemodynamic, rheological performance and red cell damage resulting to hemolysis. The general goal is the application of the results for clinical use and commercially available artificial organs, especially in rotary blood pumps and dialyzers. For this purpose, appropriate models predicting cell distribution and hemolysis rate in shear fields are developed and validated by several for this purposed developed in-vitro devices.

The here presented hypothesis on shear induced migration of blood cells towards low shear regions was evaluated in several different test cases, and the results of these in-vitro experiments corroborate not only the existence of this phenomenon, but also its significant role in hemolysis generation. This study emphasizes on the redistribution of blood cells in artificial organs due to shear fields, and on the existence of local hematocrit values. This approach can be expanded for all blood contacting artificial organs, and contribute to the reevaluation and design optimization of these devices, for a wide range of shear rates and exposure times. Comparing the results obtained from experimental studies with the Couette system and the literature data with the semi-empirical hemolysis model demonstrate that a good correspondence between them can be observed. Therefore, it can be concluded that the provided hemolysis estimation method is reliable and valid for both human and porcine blood. The proposed model considers the main hemolysis mechanisms and delivers two phenomenological outcomes; proportional quantification of each hemolysis mechanism, which is a function of shear stress, and determination of the average red blood cell membrane breakdown time, which shortens by increasing of shear stress.

The formulated model was applied to several test cases, each of which was chosen to validate different aspects of the model. Noticeable agreement between the model's predictions and the experimental data, demonstrated its reliability, reproducibility and applicability. These models can contribute to a more accurate understanding of the roll od red blood cells on hemodynamics inside the hollow fibers due to its effect on hemolysis as well as filtration process. These results can be used for "engineering" of this kind of artificial organs to achieve not only more efficacy but also improved hemocompatibility.

10.2 Future aspects

Although this study attempted to discover solutions and to highlight important design criteria for some of the current challenges in artificial organs for minimizing the blood trauma, particularly in rotary blood pumps and dialyzers, all relevant aspects are not fully investigated. Considering these facts the following suggestions may be regarded as improvements of this study, and ground for further investigations in future:

The point proven by this study is that hematocrit decrease drastically in very high shear regions, and the occurrence of hemolysis in this regions is consequently much lower than originally may assumed. Therefore, further investigation could be conducted on new rotary pumps, recognizing that the concentration of red blood cells should be appreciated in high shear regions in order to design low hemolysis pump systems. One possibility is to develop Couette devices with different gap sizes and use that for blood investigations with systematically reduced and varied hematocrit values. In this case in analogy to computer simulation the degree of shear induced hemolysis can be studied in vitro experimentally but not with constant hematocrit value. At a same time computational simulation of blood flow in the Couette device could support more realistic simulation of the final design of a rotary pump. In other words, these new experimental studies will show not only the effect of shear rate but also its dependency to hematocrit value. This could lead to optimal design which demonstrate also a high hemocompatibility. Therefore as suggested here, in order to reduce hemolysis, the significant role of local hematocrit values should be taken into consideration in the future design improvement of blood contacting devices to provide optimal hemocompatibility.

Also it might help in the future as it was discussed in chapter 6 to develop more evidence based semi-empirical models for both human and porcine blood in order to get more efficient predictions for rotary blood pumps.

According to the investigations as presented in chapter 7-9, especially the relationship between hematocrit and filtration should be still investigated for further developed experimental circuits and compare low and high flux dialyzers in order to improve the clinical application for a better water balance between extracorporeal fluid in the circuit and the patient. Also the presented idea to change the compartments seems to be worth for future investigation in order to improve the performance and hemocompatibility of the system.

Chapter 11

List of Symbols

Symbol	Description	Unit
a	Constant Value	$(-)$
A	Area	(m^2)
b	Constant Value	$(-)$
c	Constant Value	$(-)$
d	Diameter	(m)
D	Diffusion Coefficient	$(m^2.s^{-1})$
h	Height	(m)
Hct	Hematocrit	$(-)$
J	Linear Flux	$(kg\ s^{-1}\ m^{-2})$
k	(Specific) Factor / Parameter	$(-)$
K	Mass Transfer Coefficient	$(m.s^{-1})$
l	Length	(m)
N	Number of Fibers	$(-)$
p	(Partial) Pressure	(Pa)
P	Permeability Coefficient	$(m^2.s.Pa)$
pH	Expression of acidity or alkalinity of a solution	$(-)$
Q	Flow Rate	$(m^3.s^{-1})$
r	Radial coordinate, radius	(m)
Re	Reynolds Number	$(-)$
RPM	Revolutions per minute	(s^{-1})
T	Temperature	(K)
Ta	Taylor number	$(-)$
t	Time	(s)
t_{th}	Threshold rupturing time of RBCs	(s)
$\bar{t}$	Average rupturing time of RBCs	(s)
u	Velocity component in x-direction	(m/s)
V	Volume	(m^3)
x	Space coordinate	(m)
y	Space coordinate	(m)
z	Space coordinate	(m)
Greek Letters:		

Δ	Gradient (Drop)	*(-)*
$\dot{\gamma}$, G	Shear Rate	*(s⁻¹)*
Γ	*Gamma distribution function*	*(-)*
δ²	*Variance of Gamma distribution function*	*(-)*
θ	Angle of Rotation	*(degree)*
μ	Dynamic viscosity	*(Pa.s)*
ρ	Density	*(kg.m⁻³)*
τ	Shear Stress	*(Pa)*
υ	Kinematic Viscosity	*(m².s⁻¹)*
ω	Angular velocity	*(Rad/s)*

Subscription/Superscription:

b	Blood
d	Dialysate
i	Inside
o	Outside
pl	Plasma
tot	Total

Abbreviations

AWAK	*Automated Wearable Artificial Kidney*
CFD	*Computational Fluid Dynamics*
ECC	*Extra-corporeal Circulation*
NS	*Combined Model (Non-uniform Threshold Model and Sub-lethal Model)*
NUT	*Non-uniform Threshold Model*
PA	*Polyamide*
PES	*Polyethersulfone*
PMMA	*Polymethyl methacrylate*
PS	*Polysulfone*
PVC	*Polymethyl methacrylate*
RBC	*Red Blood Cell*
SUB	*Permeation Model (Sub-lethal Model)*
VAD	*Ventricle Assist Device*
WBC	*White blood cell*

Appendix I: Gamma Distribution Functions

Probability density functions in one, discrete or continuous, variable are denoted p(r) and f(x), respectively. They are assumed to be properly normalized such that:

$$\sum_r p(r) = 1 \ and \ \int_{-\infty}^{\infty} f(x)\, dx = 1$$

where the sum or the integral are taken over all relevant values for which the probability density function is defined. Statisticians often use the distribution function or as physicists more often call it the cumulative function which is defined as:

$$P(r) = \sum_{i=-\infty}^{r} p(i) \ and \ F(x) = \int_{-\infty}^{x} f(t)\, dt$$

The gamma distribution is a two-parameter family of continuous probability distributions. The general formula for the probability density function of the gamma distribution is:

$$f(x; a, b) = \frac{a\,(ax)^{b-1}e^{-ax}}{\Gamma(b)}$$

where the parameters a and b are positive real quantities as is the variable x. Note that the parameter a is simply a scale factor ;and

$$\Gamma(b) = \int_0^{\infty} t^{b-1}e^{-t}\, dt$$

For $b \leq 1$ the distribution is J-shaped and for $b > 1$ it is unimodal with its maximum at $x = \frac{b-1}{a}$.

For b = 1, the exponential distribution is obtained and with a = 1/2 and b = n/2 with n an integer the chi-squared distribution is obtained with n degrees of freedom.

Where mean value, $\mu = \frac{b}{a}$ and variance, $\delta^2 = \frac{b}{a^2}$.
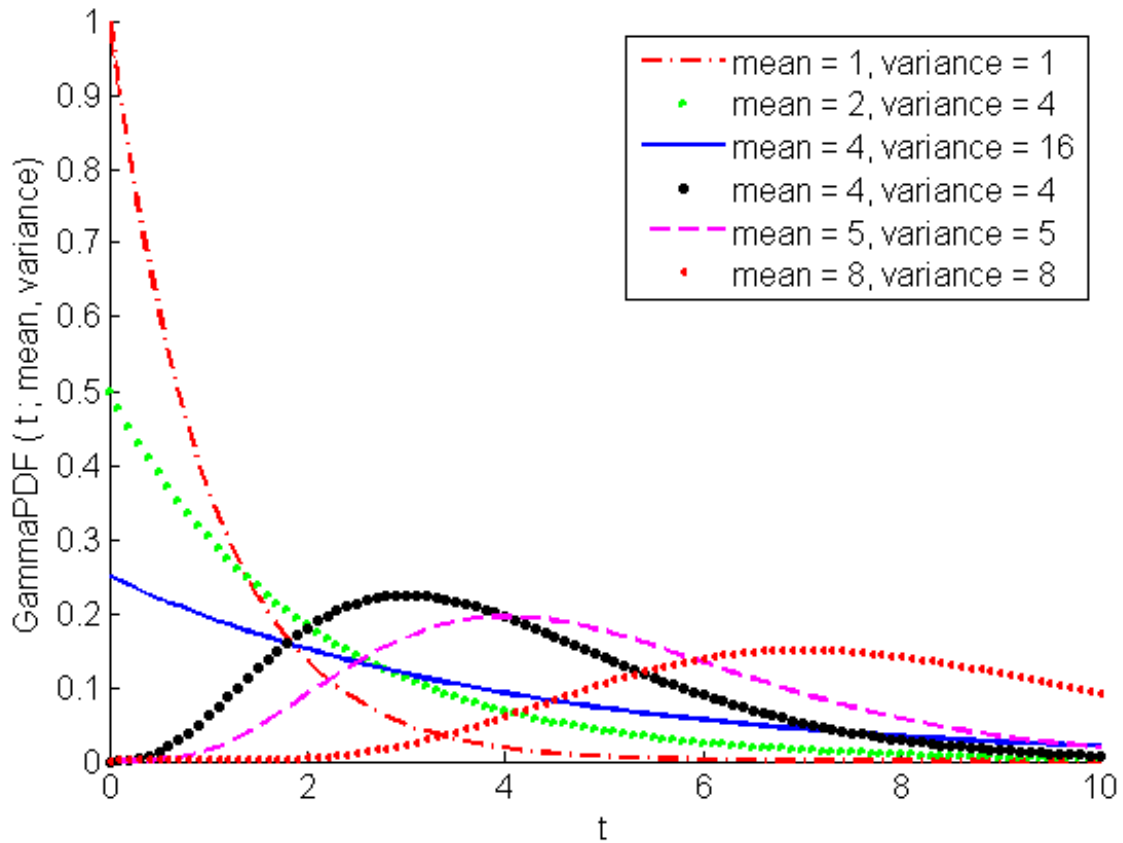
Figure A.1. Examples of Gamma distributions with different mean and variance values.

The formula for the cumulative distribution function of the gamma distribution is

$$F\ (x) = \frac{\Gamma_x(b)}{\Gamma(b)} \quad x \geq 0 \; ; b \ > 0$$

where $\Gamma(b)$ is the gamma function defined above and $\Gamma_x(b)$ is the incomplete gamma function. The incomplete gamma function has the formula

$$\Gamma_x(b) \ = \ \int_0^x t^{b-1} e^{-t} \, dt$$

The following is the plot of the gamma cumulative distribution function with the same values of γ as the pdf plots above.
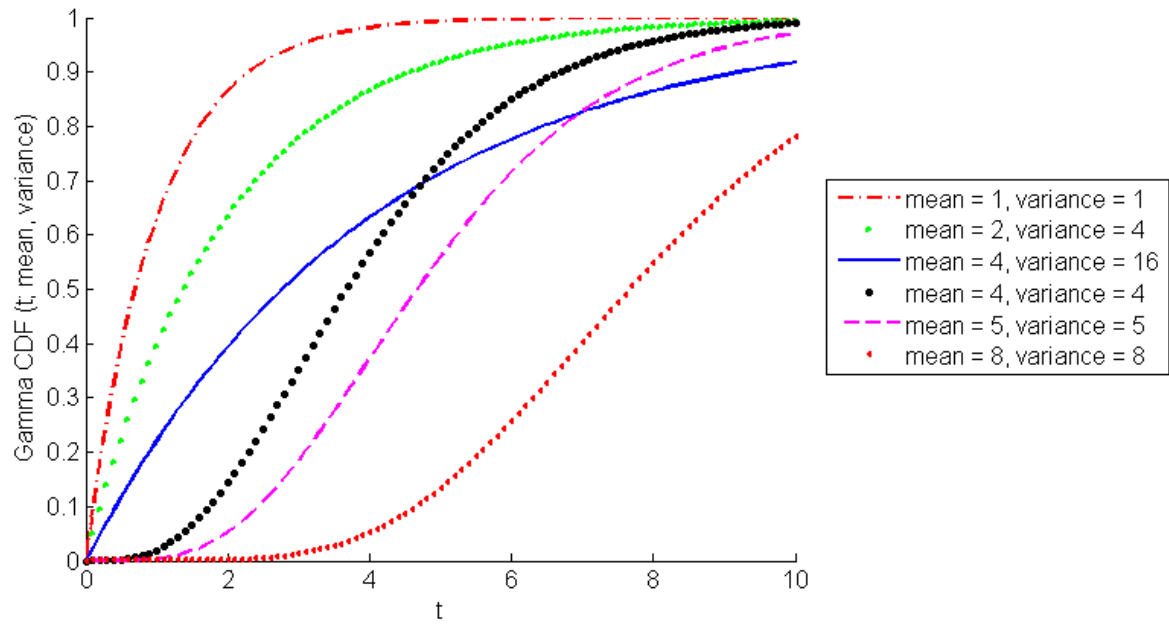
Figure A.2. Example plots of the gamma cumulative distribution function with different mean and variance values.

Appendix II: Analytical Solution of Couette Flow

For theoretical analysis it is convenient to express the governing equations in cylindrical coordinates (r, θ, z). Neglecting external forces, the Navier-Stokes equations for incompressible flow of a Newtonian fluid read as:

$$\rho \left(\frac{\partial u}{\partial t} + (u.\nabla)u \right) + \nabla p - \mu \nabla^2 u = 0 \qquad A.II.1$$

$$\nabla.u = 0 \qquad A.II.2$$

with the dynamic viscosity μ and the pressure p. The vector u = (u_r, u_θ, u_z) is composed of the velocity components in radial, azimuthal and axial direction. The Taylor-Couette system is schematically shown in Fig. A. II.1. The sense of rotation of the two cylinders shall be assumed in opposite directions.
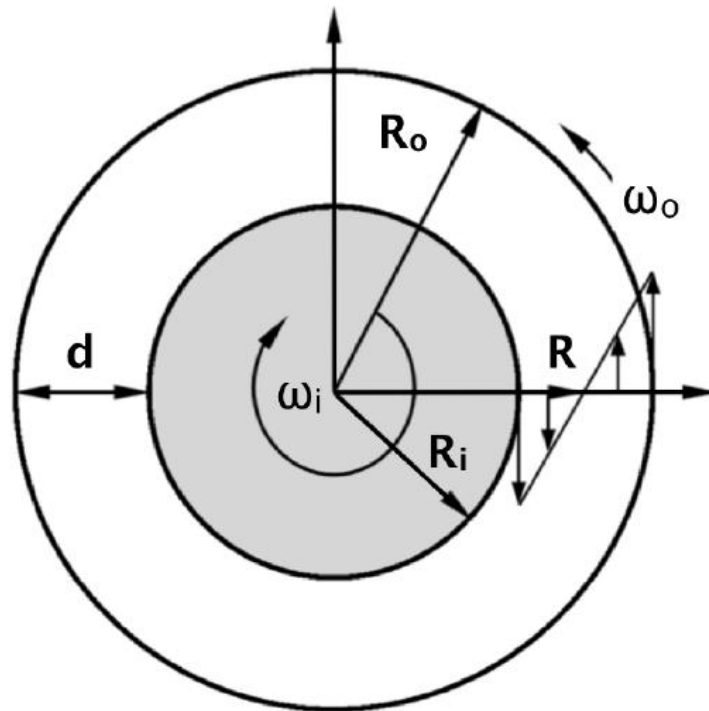
Figure A. II.1. Schematic representation of Couette flow cylinders rotating in opposite directions. R is the radial position where the angular velocity is zero.

Boundary conditions are given by the no-slip conditions at the inner and outer cylinder walls:

$$u \ (r = R_i) = (0, -\omega_i R_i \quad 0) \qquad A.II.3$$

$$u\ (r = R_O) = (0, -\omega_O R_O, 0) \qquad\qquad \text{A. II. 4}$$

The circular Couette flow in the cylindrical gap describes the laminar steady state (u_0, p_0) of a viscous fluid between two infinitely long concentric cylinders. Assuming that $u_{r0} = u_{z0} = 0$, $u_{\theta 0} = u_{\theta 0}(r)$ and $p_0 = p_0(r)$, the Navier-Stokes equations (A. II.1) simplify to

$$\frac{\partial p_0}{\partial r} - \rho\ \frac{u_{\theta 0}}{r^2} = 0 \qquad\qquad \text{A. II. 5}$$

$$\frac{1}{r}\frac{\partial}{\partial r}\left(r\frac{\partial u_{\theta 0}}{\partial r}\right) - \frac{u_{\theta 0}}{r^2} = \frac{\partial}{\partial r}\left(\frac{1}{r}\frac{\partial (r u_{\theta 0})}{\partial r}\right) = 0 \qquad\qquad \text{A. II. 6}$$

$$\frac{1}{r}\frac{\partial u_\theta}{\partial \theta} = 0 \qquad\qquad \text{A. II. 7}$$

The azimuthal component (A. II.6) is then integrated twice with respect to r to find a general solution for the Couette velocity profile:

$$u_{\theta 0}\ (r) = C_1\ \frac{r}{2} + C_2\frac{1}{r} \qquad\qquad \text{A. II. 8}$$

Matching the integration constants C1 and C2 to the boundary conditions (A. II.3) and (A. II.4) yields:

$$C_1 = \frac{2\ (\omega_i + \omega_O)R_O^2}{R_O^2 - R_i^2} - 2\ \omega_i \qquad\qquad \text{A. II. 9}$$

$$C_2 = \frac{(\omega_i + \omega_O)R_i^2 R_O^2}{R_i^2 - R_O^2} \qquad\qquad \text{A. II. 10}$$

Inserting equations A. II.9 and A. II.10 into equation A. II.8 yields the radius-dependent angular velocity ω:

$$\omega = \frac{(\omega_i + \omega_O)R_O^2\ (R_i^2 - r^2)}{(R_i^2 - R_O^2)r^2} - \omega_i \qquad\qquad \text{A. II. 11}$$

The azimuthal velocity component u_θ can be written as:

$$u_\theta(r) = r.\omega(r) \qquad\qquad \text{A. II. 12}$$

from where it follows

$$\frac{du_\theta(r)}{dr} = \frac{2(\omega_i + \omega_o)R_i^2 R_O^2}{(R_i^2 - R_O^2)r^2} \qquad \text{A. II. 13}$$

The radial position R where the angular velocity ω is zero can be derived from equation A. II.11 as:

$$R^2 = \frac{(\omega_i + \omega_o)R_i^2 R_O^2}{(\omega_i R_i^2 - \omega_o R_O^2)} \qquad \text{A. II. 14}$$

For the special case of a non-rotating inner cylinder ωi zero and r = R = Ro.

Appendix III: Step by Step model formulation mentioned in chapter 7

Model formulation for water as fluid medium

Based on presented assumptions in chapter 7, the composition of the model will commence. The amount of the filtrate flow for a single fiber in a microscopic volume element with the length of dl according to Fick's law can be assessed (57):

$$dQ_f = N.K^{fiber} A \Delta P_{tm} \tag{A. III. 1}$$

$$dQ_f = K A \Delta P_{tm}$$

$$dQ_f = K (2\pi R \, dl) [P_w(l) - P_d(l)] \tag{A. III. 2}$$

By integrating both sides of the last equation over length:

$$Q_f(l) = \int_0^l K (2\pi R) [P_w(l) - P_d(l)] dl \tag{A. III. 3}$$

$$Q_f(l) = (2\pi RK) \int_0^l [P_w(l) - P_d(l)] dl \tag{A. III. 4}$$

$$Q_f(l) = (2\pi RK) \left[\int_0^l P_w(l) \, dl - \int_0^l P_d(l) \, dl \right] \tag{A. III. 5}$$

$$Q_f(l) = (2\pi RK) \left[\int_0^l P_w(l) \, dl - \int_0^l \left(\frac{P_{di} - P_{do}}{L} l + P_{do} \right) dl \right] \tag{A. III. 7}$$

$$Q_f(l) = c_1 \left(\int_0^l P_w(l) \, dl - c_2 l^2 - c_3 l + c_4 \right) \tag{A. III. 6}$$

Where $c_1 = 2\pi RK$, $c_2 = \frac{P_{di} - P_{do}}{2L}$ and $c_3 = P_{do}$.

It is also known:

$$Q_w(l) = Q_{wi} - Q_f(l) \tag{A. III. 7}$$

$$Q_w(l) = Q_{wi} - c_1 \left(\int_0^l P_w(l) \, dl - c_2 l^2 - c_3 l + c_4 \right) \tag{A. III. 8}$$

On other hand:

$$\Delta P_w = P_{wi} - P_w(l) = \int_0^l dP_w \qquad \text{(A. III. 9)}$$

Since hollow fibers resemble cylindrical pipes and the flow is laminar, Hagen–Poiseuille equation for ΔP can be used:

$$\Delta P_w = \frac{8\,\mu\,l\,Q_w}{\pi R^4} \qquad \text{(A. III. 10)}$$

Similarly:

$$dP_w = \frac{8\,\mu}{\pi R^4} Q_w(l)dl \qquad \text{(A. III. 11)}$$

By substitution:

$$\Delta P = P_{wi} - P_w(l) = \frac{8\,\mu}{\pi R^4}\int_0^l Q_w(l)dl = \frac{8\,\mu}{\pi R^4}\int_0^l \left[Q_{wi} - c_1\left(\int_0^l P_w(l)\,dl - c_2 l^2 - c_3\,l + c_4\right)\right]dl \text{ (A. III. 12)}$$

From the derivative of Equation A. III. 12 the following equation is obtained:

$$-\acute{P}_w(l) = \frac{8\,\mu}{\pi R^4}\left[Q_{wi} - c_1\left(\int_0^l P_w(l)\,dl - c_2 l^2 - c_3\,l + c_4\right)\right] \qquad \text{(A. III. 13)}$$

Whereas the second derivative yields:

$$\acute{P}_w(l) = \frac{8\,\mu}{\pi R^4}\left[c_1(P_w(l) - 2c_2 l - c_3)\right] \qquad \text{(A. III. 14)}$$

Equation A. III. 14 is a second order linear ordinary differential equation. By solving this inhomogeneous second-order linear ordinary differential equation, the general solution of $P_b(l)$ will be obtained from:

$$P_w(l) = al + b$$

Where a and b are constants. Assuming the boundary conditions of:

$$P_w(0) = P_{wi}$$

$$P_w(L) = P_{wo}$$

Then the particular solution will have the following form.

$$\boldsymbol{P_w(l)} = \frac{P_{wo} - P_{wi}}{L}\,\boldsymbol{l} + \boldsymbol{P_{wi}} \qquad \text{(A. III. 15)}$$

By substituting $P_b(l)$ into equation A. III. 15, $Q_b(l)$ is obtained.

$$Q_w(l) = Q_{wi} - c_1 \left(\int_0^l \left(\frac{P_{wo} - P_{wi}}{L} l + P_{wi} \right) dl - c_2 l^2 - c_3 l + c_4 \right) \tag{A. III. 16}$$

$$= Q_{wi} - c_1 \left(\frac{P_{wo} - P_{wi}}{2L} l^2 + P_{wi} l - c_2 l^2 - c_3 l + c_4 + c_5 \right)$$

$$= c_1 \left(c_2 - \frac{P_{wo} - P_{wi}}{2L} \right) l^2 + (c_1 c_3 - c_1 P_{wi}) l + Q_{wi} - c_1 c_4 - c_1 c_5$$

After substitution of c_1, c_2 and c_3 and simplification:

$$Q_w(l) = Q_{wi} - \pi RK \left(\frac{P_{do} - P_{di} + P_{wo} - P_{wi}}{L} \right) l^2 - 2\pi RK (P_{wi} - P_{wo}) l - 2\pi RK \, (c_4$$

$$+ c_5) \tag{A. III. 17}$$

Since $Q_w(0) = Q_{wi}$, the term $c_4 + c_5 = 0$, so:

$$\boldsymbol{Q_w(l) = Q_{wi} - \pi RK \left(\frac{P_{do} - P_{di} + P_{wo} - P_{wi}}{L} \right) l^2 - 2\pi RK (P_{wi} - P_{do}) l} \tag{A. III. 18}$$

Hence, for $Q_f(l)$ by consideration of equation A. III. 7:

$$\boldsymbol{Q_f(l) = Q_{wi} - Q_w(l) = \pi RK \left(\frac{P_{do} - P_{di} + P_{wo} - P_{wi}}{L} \right) l^2 + 2\pi RK (P_{wi} - P_{do}) l} \tag{A. III. 19}$$

Net ultrafiltration rate can be defined as:

$$\boldsymbol{UFR = Q_f(L) = \pi RK \, (P_{wi} + P_{wo} - P_{di} - P_{do}) L} \tag{A. III. 20}$$

For clinical applications, it is reasonable to define and use an average transmembrane pressure ($\overline{TMP}$), as reported by Ronco et al.(57):

$$\overline{TMP}(l) = \frac{1}{l} \int_0^l dP_{tm}(l). \, dl \tag{A. III. 21}$$

$$\overline{TMP}(l) = \frac{1}{l} \int_0^l \left[\frac{P_{wo} - P_{wi}}{L} l + P_{wi} - \frac{P_{di} - P_{do}}{L} l - P_{do} \right] dl$$

The general solution will appear as:

$$\overline{TMP}(l) = \frac{1}{l} \left[\frac{P_{wo} - P_{wi} - P_{di} + P_{do}}{2L} l^2 + (P_{wi} - P_{do}) l \right] \tag{A. III. 22}$$

Eventually, the average $\overline{TMP}$ and the overall UFR in a dialyzer with length L can be obtained from the following equations:

$$\overline{TMP}(L) = \frac{P_{wo}+P_{wi}}{2} - \frac{P_{di}+P_{do}}{2} \tag{A. III. 23}$$

$$UFR = Q_f(L) = 2\pi RKL\,\overline{TMP}(L) \tag{A. III. 24}$$

Model formulation in Simplified model for blood as fluid medium

Based on the mentioned assumptions in chapter 7, the ultrafiltration rate taking place in a single fiber for a tiny voxel with length of *dl*, according to Fick's law can be replicated:

$$dQ_f = K^{fiber}\,dA^{fiber}\,\Delta P_{tm} \tag{A. III. 25}$$

Whereas for the complete fiber bundle in a dialyzer module, the net filtration rate is:

$$dQ_f = K\,dA\,\Delta P_{tm}$$

$$dQ_f = K\,(2\pi R\,dl)\,(P_b(l) - P_d(l) - \pi(l)\,) \tag{A. III. 26}$$

By integration of both sides over length:

$$Q_f(l) = \int_0^l K\,(2\pi R)\,(P_b(l) - P_d(l) - \pi(l)\,)dl \tag{A. III. 27}$$

$$Q_f(l) = (2\pi RK)\int_0^l (P_b(l) - P_d(l) - \pi(l)\,)dl \tag{A. III. 28}$$

$$Q_f(l) = (2\pi RK)(\int_0^l P_b(l)\,dl - \int_0^l P_d(l)\,dl - \int_0^l \pi(l)\,dl) \tag{A. III. 29}$$

$$Q_f(l) = (2\pi RK)(\int_0^l P_b(l)\,dl - \int_0^l \left(\frac{P_{di}-P_{do}}{L}\,l + P_{do}\right)dl - \int_0^l(24\,mmHg)\,dl) \tag{A. III. 30}$$

$$Q_f(l) = c_8\,(\int_0^l P_b(l)\,dl - c_9 l^2 - c_{10}\,l + c_{11}) \tag{A. III. 31}$$

Where $c_8 = 2\pi RK$, $c_9 = \frac{P_{di}-P_{do}}{2L}$ and $c_{10} = P_{do} + 24\,mmHg$.

It is also known:

$$Q_b(l) = Q_{bi} - Q_f(l) \tag{A. III. 32}$$

$$Q_b(l) = Q_{bi} - c_8 \left(\int_0^l P_b(l) \, dl - c_9 l^2 - c_{10} \, l + c_{11} \right) \tag{A. III. 33}$$

On the other hand:

$$\Delta P_b = P_{bi} - P_b(l) = \int_0^l dP_b \tag{A. III. 34}$$

The fact that hollow fibers can be approximated as cylindrical pipes and the flow in them is laminar, permits the application of Hagen–Poiseuille equation for ΔP:

$$\Delta P_b = \frac{8 \, \mu \, l \, Q_b^{fiber}}{\pi R^4} \tag{A. III. 35}$$

And here:

$$dP_b = \frac{8}{\pi N R^4} \mu(l) Q_b(l) dl \tag{A. III. 36}$$

By substitution:

$$\tag{A. III. 37}$$

$$\Delta P = P_{bi} - P_b(l) = \frac{8}{\pi N R^4} \int_0^l \mu(l) \, Q_b(l) dl$$

$$= \frac{8}{\pi N R^4} \int_0^l c_7 \left(Q_b(l)^{n-1} + 2.5 \, c_6 Q_b(l)^{n-2} + 14.1 c_6^2 \, Q_b(l)^{n-3} \right) Q_b(l) dl$$

$$= \frac{8 \, c_7}{\pi N R^4} \int_0^l \left(Q_b(l)^n + 2.5 \, c_6 Q_b(l)^{n-1} + 14.1 c_6^2 \, Q_b(l)^{n-2} \right) dl$$

This equation using $P_b(l)$ from the derivative of Equation A. III. 33 can be rewritten:

$$\acute{Q}_b(l) = - c_8 \left(P_b(l) - 2 c_9 l - c_{10} \right) \tag{A. III. 38}$$

$$P_b(l) = \frac{- \acute{Q}_b(l)}{c_8} + 2 c_9 l + c_{10} \tag{A. III. 39}$$

From equation A. III.39, $P_b(l)$ is substituted into equation A. III. 37:

$$P_{bi} + \frac{\acute{Q}_b(l)}{c_8} - 2 c_9 l - c_{10} = \frac{8 c_7}{\pi N R^4} \int_0^l \left(Q_b(l)^n + 2.5 \, c_6 Q_b(l)^{n-1} + 14.1 c_6^2 \, Q_b(l)^{n-2} \right) dl$$

$$\tag{A. III. 40}$$

The derivative of Equation A. III. 40 over length yields:

$$\frac{\acute{Q}_b(l)}{c_8} - 2 c_9 = \frac{8 c_7}{\pi N R^4} \left(Q_b(l)^n + 2.5 \, c_6 Q_b(l)^{n-1} + 14.1 c_6^2 \, Q_b(l)^{n-2} \right) \tag{A. III. 41}$$

Which can simplified in the following form:

$$\acute{Q}_b(l) = c_{12} \, Q_b(l)^n + c_{13} \, Q_b(l)^{n-1} + c_{14} \, Q_b(l)^{n-2} + c_{15} \qquad \text{(A. III. 42)}$$

Where $\qquad c_{12} = {8 \, c_7 \, c_8}/{\pi N R^4}$, $c_{13} = 20 \, {c_7 \, c_8 c_6 \, c_{12}}/{\pi N R^4}$, $\qquad c_{14} =$

$112.8 \, {c_7 \, c_8 c_6{}^2 \, c_{12}}/{\pi N R^4}$

and $c_{15} = 2 \, c_8 \, c_9$.

Equation A. III. 42 is a second order non-linear ordinary differential equation. Its solution will yield $Q_b(l)$. Subsequently, substitution of $Q_b(l)$ into equation A. III. 39 will grant $P_b(l)$. Likewise, substitution of $Q_b(l)$ into equation 7.4.4, will result in $Hct(l)$.

$$Q_b(l) = \frac{c_{12} \, l^{n+2}}{n^2 + 3n + 2} + \frac{c_{13} l^{n+1}}{n^2 + n} + \frac{c_{14} \, l^n}{n^2 - n} + \frac{c_{15} l^2}{2} + c_{16} l + c_{17} \qquad \text{(A. III. 43)}$$

where $c_{17} = Q_{bi}$, Derivative of Q_b will be:

$$\acute{Q}_b(l) = \frac{c_{12} \, l^{n+1}}{n+1} + \frac{c_{13} l^n}{n} + \frac{c_{14} \, l^{n-1}}{n-1} + c_{15} l + c_{16} \qquad \text{(A. III. 44)}$$

After substitution $\acute{Q}_b(l)$ into equation A. III. 39:

$$P_b(l) = -\frac{1}{c_8} \left(\frac{c_{12} \, l^{n+1}}{n+1} + \frac{c_{13} l^n}{n} + \frac{c_{14} \, l^{n-1}}{n-1} + c_{15} l + c_{16} \right) + 2 c_9 l + c_{10}$$

$$P_b(l) = -\frac{1}{c_8} \left(\frac{c_{12} \, l^{n+1}}{n+1} + \frac{c_{13} l^n}{n} + \frac{c_{14} \, l^{n-1}}{n-1} \right) + \left(2 c_9 - \frac{c_{15}}{c_8} \right) l - \frac{c_{16}}{c_8} + c_{10}$$

$$P_b(l) = -\frac{1}{c_8} \left(\frac{c_{12} \, l^{n+1}}{n+1} + \frac{c_{13} l^n}{n} + \frac{c_{14} \, l^{n-1}}{n-1} \right) - \frac{c_{16}}{c_8} + c_{10} \qquad \text{(A. III. 45)}$$

Application of boundary condition $P_b(0) = P_{bi}$: $c_{10} - {c_{16}}/{c_8} = P_{bi}$ and

$c_8 * (P_{do} + 3189 - P_{bi}) = c_{16}$, so $\quad P_b(L) = P_{bo}$

Then

$$P_b(L) = -\frac{c_{18}}{c_8}\left(\frac{c_{12}\,L^{n+1}}{n+1} + \frac{c_{13}L^n}{n} + \frac{c_{14}\,L^{n-1}}{n-1}\right) + P_{bi} \qquad \text{(A. III. 46)}$$

Where:

$$c_{18} = \frac{c_8\,(P_{bi} - P_{bo})}{\left(\dfrac{c_{12}\,L^{n+1}}{n+1} + \dfrac{c_{13}L^n}{n} + \dfrac{c_{14}\,L^{n-1}}{n-1}\right)}$$

Hence, the model can be rewritten as:

$$P_b(l) = -\frac{c_{18}}{c_8}\left(\frac{c_{12}\,l^{n+1}}{n+1} + \frac{c_{13}l^n}{n} + \frac{c_{14}\,l^{n-1}}{n-1}\right) + P_{bi} \qquad \text{(A. III. 47)}$$

Substitution into A. III. 43 gives us blood flow rate:

$$\boldsymbol{Q_b(l)} = \frac{\boldsymbol{c_{12}\,l^{n+2}}}{\boldsymbol{n^2 + 3n + 2}} + \frac{\boldsymbol{c_{13}l^{n+1}}}{\boldsymbol{n^2 + n}} + \frac{\boldsymbol{c_{14}\,l^n}}{\boldsymbol{n^2 - n}} + \frac{\boldsymbol{c_{15}l^2}}{\boldsymbol{2}} + \boldsymbol{c_{16}l + Q_{bi}} \quad \text{(A. III. 48)}$$

Hence filtration rate can be calculated according to the formula below:

$$\boldsymbol{Q_f(l)} = -\boldsymbol{c_{16}l} - \frac{\boldsymbol{c_{15}l^2}}{\boldsymbol{2}} - \frac{\boldsymbol{c_{12}\,l^{n+2}}}{\boldsymbol{n^2 + 3n + 2}} - \frac{\boldsymbol{c_{13}l^{n+1}}}{\boldsymbol{n^2 + n}} - \frac{\boldsymbol{c_{14}\,l^n}}{\boldsymbol{n^2 - n}} \qquad \text{(A. III. 49)}$$

$$\boldsymbol{UFR = Q_f(L)} = -\boldsymbol{c_{16}L} - \frac{\boldsymbol{c_{15}L^2}}{\boldsymbol{2}} - \frac{\boldsymbol{c_{12}\,L^{n+2}}}{\boldsymbol{n^2 + 3n + 2}} - \frac{\boldsymbol{c_{13}L^{n+1}}}{\boldsymbol{n^2 + n}} - \frac{\boldsymbol{c_{14}\,L^n}}{\boldsymbol{n^2 - n}}$$

$$\text{(A. III. 50)}$$

From the definition of $\overline{TMP}$ (average transmembrane pressure):

$$\overline{TMP}(l) = \frac{1}{l}\int_0^l dP_{tm}(l).\,dl \qquad \text{(A. III. 51)}$$

$$= \frac{1}{l}\int_0^l [P_b(l) - P_d(l) - \pi(l)]dl$$

$$\overline{TMP}(l) = \frac{1}{l}\int_0^l \left(\left(-\frac{\left(8\,^{c_7}/_{\pi NR^4}\right)l^{n+1}}{n+1} - \frac{\left(20\,^{c_7\,c_6\,c_{12}}/_{\pi NR^4}\right)l^n}{n} - \frac{\left(112.8\,^{c_7\,c_6{}^2\,c_{12}}/_{\pi NR^4}\right)l^{n-1}}{n-1}\right.\right.$$
$$\left.\left.+\;P_{bi}\right) - \left(\frac{P_{di}-P_{do}}{L}\,l + P_{do}\right) - 24\right)dl$$

The general solution will appear as:

$$\overline{TMP}(l) = \frac{1}{l}\left(-\frac{P_{di}-P_{do}}{2L}\,l^2 + (P_{bi}-P_{do})l - \frac{\left(8\,^{c_7}/_{\pi NR^4}\right)l^{n+2}}{n^2+2n+3} - \frac{\left(20\,^{c_7\,c_6\,c_{12}}/_{\pi NR^4}\right)l^{n+1}}{n^2+n}\right.$$
$$\left.-\frac{\left(112.8\,^{c_7\,c_6{}^2\,c_{12}}/_{\pi NR^4}\right)l^n}{n^2-n}\right) \tag{A. III. 52}$$

Finally, the average transmembrane pressure in a dialyzer with length L can be calculated:

$$\boldsymbol{\overline{TMP}(L)} = \frac{1}{L}\left(-\frac{P_{di}-P_{do}}{2L}L^2 + (P_{bi}-P_{do})L - \frac{\left(8\,^{c_7}/_{\pi NR^4}\right)L^{n+2}}{n^2+2n+3}\right.$$
$$\left.-\frac{\left(20\,^{c_7\,c_6\,c_{12}}/_{\pi NR^4}\right)L^{n+1}}{n^2+n} - \frac{\left(112.8\,^{c_7\,c_6{}^2\,c_{12}}/_{\pi NR^4}\right)L^n}{n^2-n}\right) \tag{A. III. 53}$$

Accordingly, the hematocrit value at any given point along the fiber is predicted by the following equation:

$$\boldsymbol{Hct\,(l)} = \frac{Q_{bi}\,Hct_i}{Q_b(l)} = \frac{c_6}{Q_b(l)} = \frac{c_6}{\dfrac{c_{12}\,l^{n+2}}{n^2+3n+2} + \dfrac{c_{13}l^{n+1}}{n^2+n} + \dfrac{c_{14}\,l^n}{n^2-n} + \dfrac{c_{15}l^2}{2} + c_{16}l + Q_{bi}}$$

$$\tag{A. III. 54}$$

Model Formulation in Advanced blood model for blood as fluid medium

Based on the mentioned assumptions on chapter 7, ultrafiltration rate of a single capillary can be approximated by a microscopic volume with surface equal to the cross-section of the hollow fiber and length of *dl*, according to Fick's law:

$$dQ_f = K^{fiber}\,dA^{fiber}\,\Delta P_{tm} \tag{A. III. 55}$$

Which for the dialyzer module as a whole it will become:

$$dQ_f = K \, dA \, \Delta P_{tm} \tag{A. III. 56}$$

$$dQ_f = K \, (2\pi R \, dl) \left(P_b(l) - P_d(l) - \pi(l) \right)$$

Integration of Equation A. III. 56 over length yields:

$$Q_f(l) = \int_0^l K \, (2\pi R) \left(P_b(l) - P_d(l) - \pi(l) \right) dl \tag{A. III. 57}$$

$$Q_f(l) = (2\pi RK) \left(\int_0^l P_b(l) \, dl - \int_0^l P_d(l) \, dl - \int_0^l \pi(l) \, dl \right) \tag{A. III. 58}$$

$$Q_f(l) = (2\pi RK) \left[\int_0^l P_b(l) \, dl - \int_0^l \left(\frac{P_{di} - P_{do}}{L} \, l + P_{do} \right) dl \right.$$
$$\left. - \int_0^l \left({}^{-984}/_{Hct(l)} + 5320 \right) dl \right] \tag{A. III. 59}$$

$$Q_f(l) = c_8 \left[\int_0^l P_b(l) \, dl - \int_0^l \left({}^{-984}/_{Hct(l)} + 5320 \right) dl - c_9 l^2 - P_{do} \, l \right] \tag{A. III. 60}$$

Where $c_8 = 2\pi RK$, $c_9 = \frac{P_{di} - P_{do}}{2L}$. It is known that:

$$Q_b(l) = Q_{bi} - Q_f(l) \tag{A. III. 61}$$

$$Q_b(l) = Q_{bi} - c_8 \left[\int_0^l P_b(l) \, dl - \int_0^l \left({}^{-984}/_{Hct(l)} + 5320 \right) dl - c_9 l^2 - P_{do} \, l \right] \tag{A. III. 62}$$

On the other hand:

$$\Delta P_b = P_{bi} - P_b(l) = \int_0^l dP_b \tag{A. III. 63}$$

Hollow fibers can be regarded as cylindrical pipes, and the flow in them is laminar, therefore Hagen–Poiseuille equation (6) can be employed for ΔP estimation:

$$\Delta P_b = {}^{8 \mu l \, Q^{fiber}}/_{\pi R^4} \tag{A. III. 64}$$

And here:

$$dP_b = \frac{8}{\pi N R^4} \mu\,(l) Q(l) dl \qquad \text{(A. III. 65)}$$

By substitution:

$$\Delta P = P_{bi} - P_b(l) = \frac{8}{\pi N R^4} \int_0^l \mu\,(l)\,Q_b(l) dl \qquad \text{(A. III. 66)}$$

$$= \frac{8}{\pi N R^4} \int_0^l (163\, c_6^2\, Q_b(l)^{-2} - 28.7\, c_6\, Q_b(l)^{-1} + 3.9)\, Q_b(l) dl$$

$$= \frac{8\, c_7}{\pi N R^4} \int_0^l \left(163\, c_6^2\, Q_b(l)^{-1} - 28.7\, c_6 + 3.9\, Q_b(l)\right) dl$$

Equation A.III. 66 can be rewritten using $P_b(l)$ from the derivative of Equation A. III. 62:

$$\acute{Q}_b(l) = -\,c_8\,(P_b(l) - 2c_9 l - P_{do} + {984}/{Hct(l)} - 5320) \qquad \text{(A. III. 67)}$$

$$P_b(l) = \frac{-\acute{Q}_b(l)}{c_8} + 2c_9 l + P_{do} - {984}/{Hct(l)} + 5320 \qquad \text{(A. III. 68)}$$

Substitution of $P_b(l)$ from Equation A. III. 68 into Equation A. III. 66:

$$P_{bi} + \frac{\acute{Q}_b(l)}{c_8} - 2c_9 l - P_{do} + \frac{984}{Hct(l)} - 5320 \qquad \text{(A. III. 69)}$$

$$= \frac{8c_7}{\pi N R^4} \int_0^l (163 c_6^2\, Q_b(l)^{-1} - 28.7 c_6 + 3.9 Q_b(l))\, dl$$

From the derivative of Equation A. III. 69 over length, it is obtained:

$$\frac{\acute{Q}_b(l)}{c_8} - 2c_9 - \frac{984}{c_6}\, Q_b(l) = \frac{8c_7}{\pi N R^4} \left(163\, c_6^2\, Q_b(l)^{-1} - 28.7\, c_6 + 3.9\, Q_b(l)\right)$$
$$\text{(A. III. 70)}$$

Which can be rewritten as:

$$\acute{Q}_b(l) = \left(c_{12}\, Q_b(l)^{-1} + c_{13} + c_{14}\, Q_b(l)\right) \qquad \text{(A. III. 71)}$$

Where $\qquad c_{12} = {1300\; c_6^2 c_7\, c_8}/{\pi N R^4}\;, \qquad c_{13} = 2\, c_8\, c_9 - 230\; {c_6\, c_7\, c_8}/{\pi N R^4}$

and $\quad c_{14} = \dfrac{31\, c_7\, c_8}{\pi N R^4} + \dfrac{984\, c_8}{c_6}$

Since c_{12} is several orders of magnitude smaller than c_{13} and c_{14}, it can be neglected, hence Equation A.III. 71 becomes:

$$\acute{Q}_b(l) = c_{13} + c_{14}\, Q_b(l) \qquad\qquad \text{(A. III. 72)}$$

Equation A. III. 72 is a second order non-linear ordinary differential equation. Solving this will yield $Q_b(l)$. A subsequent substitution of $Q_b(l)$ into Equation A. III. 68, will provide us with $P_b(l)$. Finally $Hct(l)$ can be obtained by substituting $Q_b(l)$ into Equation 7.4.4.

$$Q_b(l) = \frac{c_{13}}{c_{14}} + c_{15}e^{\sqrt{c_{14}}\, l} + c_{16}e^{-\sqrt{c_{14}}\, l} + c_{17} \qquad\qquad \text{(A. III. 73)}$$

Where c_{15}, c_{16} and c_{17} are the integration constants. Thusly, the derivative of $Q_b(l)$ will be:

$$\acute{Q}_b(l) = c_{15}\sqrt{c_{14}}\, e^{\sqrt{c_{14}}\, l} - c_{16}\sqrt{c_{14}}\, e^{-\sqrt{c_{14}}\, l} \qquad\qquad \text{(A. III. 74)}$$

Substitution $\acute{Q}_b(l)$ into Equation A. III. 68:

$$P_b(l) = -\frac{1}{c_8}\left(c_{15}\sqrt{c_{14}}\, e^{\sqrt{c_{14}}\, l} - c_{16}\sqrt{c_{14}}\, e^{-\sqrt{c_{14}}\, l}\right) + 2c_9 l + P_{do} - \frac{984}{Hct(l)} + 5320$$

$$\text{(A. III. 75)}$$

After the necessary simplifications:

$$\boldsymbol{P_b(l)} = -c_{15}\left(\frac{\sqrt{c_{14}}}{c_8} + \frac{984}{c_6}\right)e^{\sqrt{c_{14}}\, l} + c_{16}\left(\frac{\sqrt{c_{14}}}{c_8} - \frac{984}{c_6}\right)e^{-\sqrt{c_{14}}\, l} \quad \text{(A. III. 76)}$$
$$+\, 2c_9 l + P_{do} + 5320 - \frac{c_{13}}{c_{14}}$$

Application of the boundary conditions for pressure: $P_b(0) = P_{bi}$ and $P_b(L) = P_{bo}$ grants us the values of the following constants:

$$c_{15} = 10^{-8} * (0.041 * TMP - 52.3)$$

$$c_{16} = 10^{-8} * (0.1356 * TMP - 37.1)$$

$$c_{17} = Q_{bi} - c_{15} - c_{16} - \frac{c_{13}}{c_{14}}$$

Application of the boundary condition for flow rate: $Q_b(0) = Q_{bi}$:

$$Q_b(l) = c_{15}e^{\sqrt{c_{14}}\, l} + c_{16}e^{-\sqrt{c_{14}}\, l} + Q_{bi} - c_{15} - c_{16} \qquad \text{(A. III. 77)}$$

Hence:

$$Q_f(l) = c_{15} + c_{16} - c_{15}e^{\sqrt{c_{14}}\, l} - c_{16}e^{-\sqrt{c_{14}}\, l} \qquad \text{(A. III. 78)}$$

$$UFR = Q_f(L) = c_{15} + c_{16} - c_{15}e^{\sqrt{c_{14}}\, L} - c_{16}e^{-\sqrt{c_{14}}\, L} \qquad \text{(A. III. 79)}$$

$$Hct\,(l) = \frac{Q_i\, Hct_i}{Q(l)} = \frac{c_6}{Q(l)} = \frac{c_6}{c_{15}e^{\sqrt{c_{14}}\, l} + c_{16}e^{-\sqrt{c_{14}}\, l} + Q_{bi} - c_{15} - c_{16}}$$

$$\text{(A. III. 80)}$$

Bibliography

1. Abouna, G.M. *Organ shortage crisis: problems and possible solutions*. in *Transplantation proceedings*. 2008. Elsevier.
2. Nosé, Y., et al., *Development of rotary blood pump technology: past, present, and future.* Artificial organs, 2000. 24(6): p. 412-420.
3. Tchantchaleishvili, V., et al., *Evaluation and treatment of pump thrombosis and hemolysis.* Annals of cardiothoracic surgery, 2014. 3(5): p. 490.
4. Vitale, F., L. Turchetti, and M.C. Annesini, *Modeling of Mechanical Blood Damage: a Discussion of Current Approaches and Alternative Proposals.* Icheap-10: 10th International Conference on Chemical and Process Engineering, Pts 1-3, 2011. 24: p. 961-966.
5. Wells, R.M., *Blood-Gas Transport and Hemoglobin Function: Adaptations for Functional and Environmental Hypoxia.* Fish physiology, 2009. 27: p. 255-299.
6. Silbernagl, S. and A. Despopoulos, *Color atlas of physiology*. 2009: Thieme.
7. White, J.G., *Platelet Structure.* Platelets, 2013: p. 117.
8. Fox, S.I., *Fundamentals of human physiology*. 2009: McGraw-Hill.
9. Widmaier, E., H. Raff, and T. Kevin, *Strang In Vander's Human Physiology*. 2008, Mc Graw-Hill International edition, pp-241-42.
10. Trsukey, G., F. Yuan, and D. Katz, *Transport phenomena in biological systems*. second ed. 2009, New Jersey: Prentice Hall.
11. Waugh, R.E. and R.M. Hochmuth, *Mechanics and deformability of hematocytes.* The biomedical engineering handbook, 1995. 35: p. 474-486.
12. Behbahani, M.J., *Modeling and Simulation of Shear-Dependent Platelet Reactions in Blood Vessels and Blood-Contacting Medical Devices*. 2011: Verlag Dr. Hut.
13. Litin, S.C., *Mayo Clinic Family Health Book*. 2008: Recording for the Blind & Dyslexic.
14. Shinton, N.K., *Desk Reference for Hematology, Second Edition*. 2007: CRC Press.
15. Bain, B.J., *Blood cells: a practical guide*. 2015: John Wiley & Sons.
16. Robertson, A.M., A. Sequeira, and M.V. Kameneva, *Hemorheology*, in *Hemodynamical flows*. 2008, Springer. p. 63-120.
17. Yen, R. and Y. Fung, *Effect of velocity distribution on red cell distribution in capillary blood vessels.* American Journal of Physiology-Heart and Circulatory Physiology, 1978. 235(2): p. H251-H257.
18. Baskurt, O.K., *Handbook of hemorheology and hemodynamics*. Vol. 69. 2007: IOS press.
19. Fåhræus, R. and T. Lindqvist, *The viscosity of the blood in narrow capillary tubes.* American Journal of Physiology--Legacy Content, 1931. 96(3): p. 562-568.
20. Pries, A., D. Neuhaus, and P. Gaehtgens, *Blood viscosity in tube flow: dependence on diameter and hematocrit.* American Journal of Physiology-Heart and Circulatory Physiology, 1992. 263(6): p. H1770-H1778.
21. Segre, G., *Radial particle displacements in Poiseuille flow of suspensions.* Nature, 1961. 189: p. 209-210.
22. Jay, A.W., *Viscoelastic properties of the human red blood cell membrane: I. Deformation, volume loss, and rupture of red cells in micropipettes.* Biophysical journal, 1973. 13(11): p. 1166.
23. Katanov, D., G. Gompper, and D.A. Fedosov, *Microvascular blood flow resistance: Role of red blood cell migration and dispersion.* Microvascular research, 2015. 99: p. 57-66.
24. Serge, G. and A. Silberberg, *Behavior of macroscopic rigid spheres in Poiseuille flow.* J. Fluid Mech, 1962. 14(1): p. 115-157.
25. Di Carlo, D., et al., *Continuous inertial focusing, ordering, and separation of particles in microchannels.* Proceedings of the National Academy of Sciences, 2007. 104(48): p. 18892-18897.
26. Mchedlishvili, G. and N. Maeda, *Blood Flow Structure Related to Red Cell Flow: A Determinant of Blood Fluidity in Narrow Microvessels.* The Japanese journal of physiology, 2001. 51(1): p. 19-30.

27. Schobeiri, M.T., *Fluid mechanics for engineers: a graduate textbook*. 2010: Springer Science & Business Media.

28. Hunt, B.W., *Fluid mechanics for civil engineers*. 1995: Department of Civil Engineering, University of Canterbury.

29. Motthaghy, K., et al., *Oxygen uptake into the sheared flowing blood: Effects of red cell membranes and haematocrit*, in *Oxygen Transport to Tissue-V*. 1984, Springer. p. 175-185.

30. Fung, Y.-C., *Biomechanics: mechanical properties of living tissues*. 2013: Springer Science & Business Media.

31. Mottaghy, K., *Rheological effects of blood-material interactions in extracorporeal circulation.* Current Perspectives of the Extracorporeal Circulation, 2000: p. 1-12.

32. Schmid-S.H, R. Wells, and Goldston.J, *Increased Viscous Resistance of Blood Due to Hypertonicity a Possible Mechanism for Intrarenal Distribution of Blood Flow.* Federation Proceedings, 1969. 28(2): p. 716-&.

33. Barnes, H.A., J.F. Hutton, and K. Walters, *An introduction to rheology*. Vol. 3. 1989: Elsevier.

34. Taskin, M.E., et al., *Micro-scale modeling of flow and oxygen transfer in hollow-fiber membrane bundle.* Journal of membrane science, 2010. 362(1): p. 172-183.

35. Zhang, J., et al., *Characterization of membrane blood oxygenation devices using computational fluid dynamics.* Journal of membrane science, 2007. 288(1): p. 268-279.

36. Jones, S.A., *A relationship between Reynolds stresses and viscous dissipation: implications to red cell damage.* Annals of biomedical engineering, 1995. 23(1): p. 21-28.

37. Kameneva, M.V., et al., *In vitro evaluation of hemolysis and sublethal blood trauma in a novel subcutaneous vascular access system for hemodialysis.* ASAIO journal, 2002. 48(1): p. 34-38.

38. Leverett, L., et al., *Red blood cell damage by shear stress.* Biophysical journal, 1972. 12(3): p. 257.

39. Blackshear, P. and G. Blackshear, *Mechanical hemolysis, Skalak R., Chen S., Handbook of bioengineering VOL. 15, 1987, 15.1-15.19*. McGraw Hill, New York.

40. Schmid-Schönbein, H. and R. Wells, *Fluid drop-like transition of erythrocytes under shear.* Science, 1969. 165(3890): p. 288-291.

41. Mottaghy, K., et al., *THE FLOATING-DROPLETS OXYGENATOR: DEVELOPMENTS USING FLUOROCAREONS WITH COAXIAL ROTATING CYLINDERS.* ASAIO Journal, 1977. 23(1): p. 464-468.

42. Boettcher, W., F. Merkle, and H.-H. Weitkemper, *History of extracorporeal circulation: the invention and modification of blood pumps.* The Journal of extra-corporeal technology, 2003. 35(3): p. 184-191.

43. Reul, H., *Technical requirements and limitations of miniaturized axial flow pumps for circulatory support.* Cardiology, 1994. 84(3): p. 187-193.

44. Akdis, M. and H. Reul, *Mechanical blood pumps for cardiac assistance.* Applied Bionics and Biomechanics, 2005. 2(2): p. 73-80.

45. Reul, H.M. and M. Akdis, *Blood pumps for circulatory support.* PERFUSION-SEVENOAKS-, 2000. 15(4): p. 295-312.

46. 2015; Available from: http://heartmateii.com/heartmate-ii-system.aspx.

47. Luciani, G.B. and G.M. Boffa, *Donor shortage in heart transplantation.* Cardiovascular Surgery, 1994. 107(5).

48. Goldstein, D.J., *Worldwide experience with the MicroMed DeBakey Ventricular Assist Device® as a bridge to transplantation.* Circulation, 2003. 108(10 suppl 1): p. II-272-II-277.

49. Young, J.B., *Healing the heart with ventricular assist device therapy: mechanisms of cardiac recovery.* The Annals of thoracic surgery, 2001. 71(3): p. S210-S219.

50. Behbahani, M., et al. *Towards shape optimization for ventricular assist devices using parallel stabilized FEM*. in *Proceedings of the NIC Symposium*. 2008.

51. Chobanian, A.V., *Joint National Committee on Prevention, Detection, Evaluation, and Treatment of High Blood Pressure. National Heart, Lung, and Blood Institute; National High*

Blood Pressure Education Program Coordinating Committee: Seventh report of the Joint National Committee on Prevention, Detection, Evaluation, and Treatment of High Blood Pressure. Hypertension, 2003. 42: p. 1206-1252.

52. Rothenburger, M., et al., *Treatment of thrombus formation associated with the MicroMed DeBakey VAD using recombinant tissue plasminogen activator.* Circulation, 2002. 106(12 suppl 1): p. I-189-I-192.

53. Couser, W.G., et al., *The contribution of chronic kidney disease to the global burden of major noncommunicable diseases.* Kidney international, 2011. 80(12): p. 1258-1270.

54. Stevens, L.A., et al., *Assessing kidney function—measured and estimated glomerular filtration rate.* New England Journal of Medicine, 2006. 354(23): p. 2473-2483.

55. Vanholder, R.C., R.V. De Smet, and S. Ringoir, *Assessment of urea and other uremic markers for quantification of dialysis efficacy.* Clinical chemistry, 1992. 38(8): p. 1429-1436.

56. Roy, T., J. Vienken, and P. Wabel, *Stand der Technik bei der Nieren-und Leberersatztherapie/Kidney and liver support therapies: state-of-the-art methods.* Biomedizinische Technik/Biomedical Engineering, 2009. 54(5): p. 245-254.

57. Ronco, C., *Problems related to backfiltration in hemodialysis.* Nefrologia, 1990. 10(Supl 3): p. 33-43.

58. Ivanovich, P., A. Manzler, and R. Drake, *Acute hemolysis following hemodialysis.* ASAIO Journal, 1969. 15(1): p. 316-318.

59. Bronzino, J.D., *Biomedical engineering handbook*. Vol. 2. 1999: CRC press.

60. Schmidt, R.F. and G. Thews, *Physiologie des Menschen*. 2013: Springer-Verlag.

61. Babb, A.L., et al., *Hemodialyzer evaluation by examination of solute molecular spectra.* ASAIO Journal, 1972. 18(1): p. 98-105.

62. Vanholder, R., et al., *Review on uremic toxins: classification, concentration, and interindividual variability.* Kidney international, 2003. 63(5): p. 1934-1943.

63. James, W.D., T. Berger, and D. Elston, *Andrews' diseases of the skin: clinical dermatology*. 2015: Elsevier Health Sciences.

64. Moake, J.L., *Thrombotic microangiopathies.* New England Journal of Medicine, 2002. 347(8): p. 589-600.

65. George, J.N., *Thrombotic thrombocytopenic purpura.* New England Journal of Medicine, 2006. 354(18): p. 1927-1935.

66. Moake, J.L. *von Willebrand factor, ADAMTS-13, and thrombotic thrombocytopenic purpura*. in *Seminars in hematology*. 2004. Elsevier.

67. Abel, J.J., L. Rowntree, and B. Turner, *On the removal of diffusible substances from the circulating blood by means of dialysis.* Transactions of the Association of American Physicians, 1913. 28: p. 51.

68. ABEL, J.J., L.G. ROWNTREE, and B. Turner, *On the removal of diffusible substances from the circulating blood of living animals by dialysis II. Some constituents of the blood.* Journal of Pharmacology and Experimental Therapeutics, 1914. 5(6): p. 611-623.

69. Quinton, W., D. Dillard, and B.H. Scribner, *Cannulation of blood vessels for prolonged hemodialysis.* ASAIO Journal, 1960. 6(1): p. 104-113.

70. Kiil, F., *Development of a parallel-flow artificial kidney in plastics.* Acta chirurgica Scandinavica. Supplementum, 1960: p. 142.

71. Leonard, E.F. and L.W. Bluemle Jr, *The permeability concept as applied to dialysis.* ASAIO Journal, 1960. 6(1): p. 33-37.

72. Lipps, B.J., et al., *THE HOLLOW FIBR ARTIFICIAL KIDNEY.* ASAIO Journal, 1967. 13(1): p. 200-207.

73. Henderson, L., et al., *BLOOD PURIFICATION BY ULTRAFILTRATION AND FLUID REPACEMENT (DIAFILTRATION).* ASAIO Journal, 1967. 13(1): p. 216-222.

74. Popovich, R., et al., *The definition of a novel portable/wearable equilibrium peritoneal dialysis technique.* Trans Am Soc Artif Intern Organs, 1976. 5(64): p. 484-489.

75.   Ronco, C., et al., *Blood and dialysate flow distributions in hollow-fiber hemodialyzers analyzed by computerized helical scanning technique.* Journal of the American Society of Nephrology, 2002. 13(suppl 1): p. S53-S61.

76.   Ronco, C., R. Bellomo, and J.A. Kellum, *Critical care nephrology*. 2008: Elsevier Health Sciences.

77.   Sperelakis, N., *Cell physiology source book: Essentials of membrane biophysics*. 2012: Elsevier.

78.   Wehner, F., et al., *Cell volume regulation: osmolytes, osmolyte transport, and signal transduction*. 2004: Springer.

79.   Forni, L. and P. Hilton, *Continuous hemofiltration in the treatment of acute renal failure.* New England Journal of Medicine, 1997. 336(18): p. 1303-1309.

80.   Kramer, P., et al., *Intensive care potential of continuous arteriovenous hemofiltration.* ASAIO Journal, 1982. 28(1): p. 28-32.

81.   Wizemann, V., *Hemodiafiltration—An Avenue to Shorter Dialysis?* 1985.

82.   Lipnizki, F. and R.W. Field, *Mass transfer performance for hollow fibre modules with shell-side axial feed flow: using an engineering approach to develop a framework.* Journal of Membrane Science, 2001. 193(2): p. 195-208.

83.   Petitclerc, T., *Estimation of mass transfer through a hemodialyzer: theoretical approach and clinical applications.* Artificial organs, 1998. 22(7): p. 601-607.

84.   Krick, G. and C. Ronco, *On-line Hemodiafiltration: The Journey and the Vision*. 2011: Karger Medical and Scientific Publishers.

85.   Ledebo, I., et al., *Progress in dialysis technology—clinical benefit vs increased complexity and risk. Report on the Dialysis Opinion Symposium at the ERA–EDTA Congress, 7 June 1998, Rimini.* Nephrology Dialysis Transplantation, 1999. 14(9): p. 2101-2105.

86.   Ronco, C., *Backfiltration in clinical dialysis: nature of the phenomenon, mechanisms and possible solutions.* The International journal of artificial organs, 1990. 13(1): p. 11.

87.   Rangel, A.V., et al., *Backfiltration: past, present and future.* 2011.

88.   Uhlenbusch-Körwer, I., et al., *Understanding membranes and dialysers*. 2004: Pabst Lengerich.

89.   Göhl, H., R. Buck, and H. Strathmann, *Basic features of the polyamide membranes.* 1992.

90.   Ronco, C., et al., *Effects of a reduced inner diameter of hollow fibers in hemodialyzers.* Kidney international, 2000. 58(2): p. 809-817.

91.   Sugaya, H. and Y. Sakai, *Polymethylmethacrylate: from polymer to dialyzer.* 1999.

92.   Randoux, C., et al., *Filtration of native and glycated β 2-microglobulin by charged and neutral dialysis membranes.* Kidney international, 2001. 60(4): p. 1571-1577.

93.   Gurland, H., et al., *Definitions and terminology in biocompatibility.* Nephrology, dialysis, transplantation, 1994. 9: p. 4-10.

94.   Indeglia, R., et al., *Influence of mechanical factors on erythrocyte sublethal damage.* ASAIO Journal, 1968. 14(1): p. 264-272.

95.   Peirce, E.C., *Draft proposal: standard for blood gas exchangers. .* Transaction of American Society of Artificial Internal Organs, 1976. 22: p. 734.

96.   Naito, K., K. Mizuguchi, and Y. Nosé, *The need for standardizing the index of hemolysis.* Artificial organs, 1994. 18(1): p. 7-10.

97.   Wurzinger, L., R. Opitz, and H. Eckstein, *Mechanical bloodtrauma. An overview.* Angeiologie, 1986. 38(3): p. 81-97.

98.   Gartner, M.J., et al., *Modeling flow effects on thrombotic deposition in a membrane oxygenator.* Artificial organs, 2000. 24(1): p. 29-36.

99.   Kirschfink, M., B. Kovacs, and K. Mottaghy, *Extracorporeal circulation: in vivo and in vitro analysis of complement activation by heparin-bonded surfaces.* Circulatory shock, 1993. 40(3): p. 221-226.

100.   Kopp, R., et al., *Hemocompatibility of a miniaturized extracorporeal membrane oxygenation and a pumpless interventional lung assist in experimental lung injury.* Artificial organs, 2010. 34(1): p. 13-21.

101. Kopp, R., et al., *Effect of hirudin versus heparin on hemocompatibility of blood contacting biomaterials: an in vitro study.* The International journal of artificial organs, 2005. 28(12): p. 1272-1277.

102. Kopp, R., K. Mottaghy, and M. Kirschfink, *Mechanism of complement activation during extracorporeal blood-biomaterial interaction: effects of heparin coated and uncoated surfaces.* Asaio Journal, 2002. 48(6): p. 598-605.

103. Goubergrits, L., *Numerical modeling of blood damage: current status, challenges and future prospects.* Expert Review of Medical Devices, 2006. 3(5): p. 527-531.

104. Goubergrits, L. and K. Affeld, *Numerical estimation of blood damage in artificial organs.* Artificial Organs, 2004. 28(5): p. 499-507.

105. Taskin, M.E., et al., *Evaluation of Eulerian and Lagrangian models for hemolysis estimation.* ASAIO journal, 2012. 58(4): p. 363-372.

106. Pauli, L., et al., *Transient stress-based and strain-based hemolysis estimation in a simplified blood pump.* International journal for numerical methods in biomedical engineering, 2013. 29(10): p. 1148-1160.

107. Fung, Y.-c., *Biomechanics: circulation*. 2013: Springer Science & Business Media.

108. Eastlake, C.N., *An aerodynamicist's view of lift, Bernoulli, and Newton.* The Physics Teacher, 2002. 40(3): p. 166-173.

109. Leighton, D. and A. Acrivos, *The shear-induced migration of particles in concentrated suspensions.* Journal of Fluid Mechanics, 1987. 181: p. 415-439.

110. Zhao, H., E.S. Shaqfeh, and V. Narsimhan, *Shear-induced particle migration and margination in a cellular suspension.* Physics of Fluids (1994-present), 2012. 24(1): p. 011902.

111. Leighton, D. and A. Acrivos, *The lift on a small sphere touching a plane in the presence of a simple shear flow.* Zeitschrift für angewandte Mathematik und Physik ZAMP, 1985. 36(1): p. 174-178.

112. Evans, D.G. and X. Duan, *Preparation of layered double hydroxides and their applications as additives in polymers, as precursors to magnetic materials and in biology and medicine.* Chemical Communications, 2006(5): p. 485-496.

113. Taylor, G.I., *Stability of a viscous liquid contained between two rotating cylinders.* Philosophical Transactions of the Royal Society of London. Series A, Containing Papers of a Mathematical or Physical Character, 1923: p. 289-343.

114. Bergmann, B. and D.-I.M. Behbahani, *Numerische Simulation thrombozytaerer Reaktionen in einem Taylor-Couette System.* 2008.

115. Mottaghy, K. and H. Hanse, *Effect of combined shear, secondary and axial flow of blood on oxygen uptake.* Chemical engineering communications, 1985. 36(1-6): p. 269-279.

116. Rumscheidt, F.-D. and S. Mason, *Particle motions in sheared suspensions XII. Deformation and burst of fluid drops in shear and hyperbolic flow.* Journal of Colloid Science, 1961. 16(3): p. 238-261.

117. Torza, S., R. Cox, and S. Mason, *Particle motions in sheared suspensions XXVII. Transient and steady deformation and burst of liquid drops.* Journal of Colloid and Interface science, 1972. 38(2): p. 395-411.

118. Ding, J., et al., *Shear-Induced Hemolysis: Species Differences.* Artificial organs, 2015.

119. Giersiepen, M., et al., *Estimation of Shear Stress-Related Blood Damage in Heart-Valve Prostheses - Invitro Comparison of 25 Aortic Valves.* International Journal of Artificial Organs, 1990. 13(5): p. 300-306.

120. Yeleswarapu, K.K., et al., *A mathematical model for shear-induced hemolysis.* Artif Organs, 1995. 19(7): p. 576-82.

121. Sowemimo-Coker, S.O., *Red blood cell hemolysis during processing.* Transfusion medicine reviews, 2002. 16(1): p. 46-60.

122. Paul, R., et al., *Recent findings on flow induced blood damage: critical shear stresses and exposure times obtained with a high shear Couette-system.* INTERNATIONAL JOURNAL OF ARTIFICIAL ORGANS, 1999. 22: p. 256-256.

123. Schwartz, C.J., N.T. Werthessen, and S.G. Wolf, *Structure and function of the circulation*. 1981, Plenum Press: New York; London.

124. Heuser, G. and R. Opitz, *A Couette Viscometer for Short-Time Shearing of Blood.* Biorheology, 1980. 17(1-2): p. 17-24.

125. Liu, T.-Y., et al., *Hemocompatibility and anaphylatoxin formation of protein-immobilizing polyacrylonitrile hemodialysis membrane.* Biomaterials, 2005. 26(12): p. 1437-1444.

126. Abayli, E. and M. Çamlibel, *The effect of high-flux hemodialysis on renal anemia.* 2004.

127. Phrommintikul, A., et al., *Mortality and target haemoglobin concentrations in anaemic patients with chronic kidney disease treated with erythropoietin: a meta-analysis.* The lancet, 2007. 369(9559): p. 381-388.

128. Ronco, C., et al., *Effects of hematocrit and blood flow distribution on solute clearance in hollow-fiber hemodialyzers.* Nephron, 2001. 89(3): p. 243-250.

129. Severs, E. and J. Austin, *Flow properties of vinyl chloride resin plastisols.* Industrial & Engineering Chemistry, 1954. 46(11): p. 2369-2375.

130. Podolsky, R.D., *Temperature and water viscosity: physiological versus mechanical effects on suspension feeding.* SCIENCE-NEW YORK THEN WASHINGTON-, 1994: p. 100-100.

131. Rosentrater, K.A. and R.A. Flores, *Physical and rheological properties of slaughterhouse swine blood and blood components.* Transactions of the ASAE, 1997. 40(3): p. 683-689.

132. Guth, E. and R. Simha, *Untersuchungen über die Viskosität von Suspensionen und Lösungen. 3. Über die Viskosität von Kugelsuspensionen.* Kolloid-Zeitschrift, 1936. 74(3): p. 266-275.

133. Black, L.L. and C.A. Wiederhielm, *Plasma oncotic pressures and hematocrit in the intact, unanesthetized bat.* Microvascular research, 1976. 12(1): p. 55-58.

134. Landis, E. and J. Pappenheimer, *Exchange of substances through capillary walls*, in *Handbook of Physiology*, W. Hamilton and P. Dow, Editors. 1963: Washington, DC. p. 961-1034

135. Fiore, G.B., et al., *A new semiempirical mathematical model for prediction of internal filtration in hollow fiber hemodialyzers.* Blood purification, 2006. 24(5-6): p. 555-568.

136. Ronco, C., et al., *A new scintigraphic method to characterize ultrafiltration in hollow fiber dialyzers.* Kidney international, 1992. 41(5): p. 1383-1393.

Curriculum Vitae

Personal Information:

First Name: Ali

Surname: Poorkhalil

Date of Birth: 17.05.1985

Place of Birth: Dezfool, Iran

Education Background:

2011 – 2016	**Ph.D in Chemical Engineering** Institute of Biochemical Engineering and Institute of Physiology RWTH Aachen University, Germany **Thesis title**: Impact of Red Cell Distribution in Sheared Blood Flow upon Quantification of Hemolysis Rate in Artificial Organs
2007 – 2009	**M.Sc. in Polymer Engineering** Department of Chemical Eng., Polymer group University of Tarbiat Modares, Iran **Thesis title**: "Preparation of Polyurethane and Polyvinyl Alcohol Membranes with Cyclodextrins and their Inclusion Complexes and Studying Gas Permeation Properties"
2003 – 2007	**B.Sc. in Polymer Engineering** Department of Polymer Engineering, Amirkabir University of Technology, Iran **Thesis title**: "Evaluation of Effect of Coupling Agent Epoxy/Glass Fibre Composites on Physical and Mechanical Properties"

1999 – 2003   Diploma in Mathematics and Physics, Shikh Ansari High School, Dezfool (National Organization for Development of Exceptional Talents), Iran